Titre: Title:	Source of Bright Few-Cycle Twin Beams Near the Single-Mode Limit Toward Extreme Nonlinear Optics
Auteur: Author:	Patrick Cusson
Date:	2026
Type:	Mémoire ou thèse / Dissertation or Thesis
Référence: Citation:	Cusson, P. (2026). Source of Bright Few-Cycle Twin Beams Near the Single-Mode Limit Toward Extreme Nonlinear Optics [Thèse de doctorat, Polytechnique Montréal]. PolyPublie. https://publications.polymtl.ca/74058/

POLYTECHNIQUE MONTRÉAL
affiliée à l'Université de Montréal

Source of Bright Few-Cycle Twin Beams Near the Single-Mode Limit Toward Extreme Nonlinear Optics

PATRICK CUSSON
Département de génie physique

Thèse présentée en vue de l'obtention du diplôme de *Philosophiæ Doctor*
Génie physique

Mars 2026

POLYTECHNIQUE MONTRÉAL
affiliée à l'Université de Montréal

Cette thèse intitulée :

Source of Bright Few-Cycle Twin Beams Near the Single-Mode Limit Toward Extreme Nonlinear Optics

présentée par **Patrick CUSSON**
en vue de l'obtention du diplôme de *Philosophiæ Doctor*
a été dûment acceptée par le jury d'examen constitué de :

Sean MOLESKY, président
Denis SELETSKIY, membre et directeur de recherche
Stéphane VIRALLY, membre et codirecteur de recherche
Nicolás QUESADA, membre
Benjamin BRECHT, membre externe

DEDICATION

To Sandra, Fred, and RouKi,
who give meaning to all my work

ACKNOWLEDGEMENTS

I would first like to thank Denis Seletskiy for the numerous amazing opportunities he offered me over the years, starting with welcoming me into the femtoQ team right as it was founded. I learned so much about science and pedagogy from our interactions, and I hope to achieve a similar impact on my students someday. I also thank Stéphane Virally for all the time he spent helping me solve technical issues and develop the confidence needed to push this project to the finish line.

I am grateful to all my current and former colleagues in femtoQ. Their daily support and warm presence were invaluable in making this project not only successful, but also fun. Among them, I want to give special thanks to Benjamin, Étienne, and Gabriel, whose presence was essential in keeping me sane through the hardest parts of this project. I also want to acknowledge Nicolas for his work in designing and implementing the Python GUI for the lab experiments, which proved to be immensely useful.

I thank the technical staff of Polytechnique, in particular Émile and Mikaël, who helped in setting up the lab and my experiments. I am thankful to Andrei, Maria, and Francesco at the Max Planck Institute for the Science of Light, who gave me a warm welcome in their labs and helped accelerate my work by sharing their expertise with me. I give my thanks to Alexander Franzen, creator of the ComponentLibrary, a vector graphics library I used for drawing optical experimental setups in this thesis. I also want to thank Alain Rochefort, Stéphane Payeur, François Thompson, and Martine Richer, whose formative presence at various points of my life all had a major impact on the completion of this thesis.

I am eternally grateful to my friends and my family for their love and unwavering support. We often hear that "it takes a village to raise a child", but as I complete this journey and look back on all the amazing people who cheered me on, I can confidently say that it also takes a village to raise a PhD, and that I managed to surround myself with a great one.

Lastly, my deepest thanks go to my partner Sandra. Thank you for always believing in me, for making every day a little brighter with your smile, and for always making sure that I take care of myself. Nearly 12 years later, I still can't believe how lucky I am to have found someone as kind, funny, smart, and loving as you to share my brief passage through this frenetic world. I would not have had the courage to take on this challenge without having you by my side.

This work was supported by the Fonds de recherche du Québec – Nature et technologies

(FRQNT) under grant numbers 320144 (https://doi.org/10.69777/320144) and 258978 (https://doi.org/10.69777/258978). I acknowledge the support of the Natural Sciences and Engineering Research Council of Canada (NSERC). This project has received funding from the European Union's Horizon Europe research and innovation programme under grant agreement No 101070700.

RÉSUMÉ

La production de paires de photons intriquées dans la conversion paramétrique descendante (*parametric down-conversion*, PDC) est un élément fondamental de nombreuses technologies quantiques, incluant notamment l'informatique, la communication et la métrologie quantique. Grâce aux progrès de la technologie laser ultrarapide, la PDC peut désormais être poussée dans le régime de haut gain, où les paires de photons se transforment en faisceaux jumeaux brillants (*bright twin beams*, BTBs) avec une intensité optique comparable à celle des systèmes laser commerciaux. L'accès à cet état quantique macroscopique de la lumière permet d'étudier expérimentalement les interactions lumière-matière extrêmes induites par de la lumière non classique.

Les phénomènes d'optique non linéaires dans le régime non-perturbatif, tels que la génération d'harmoniques élevées et l'effet tunnel électronique, sont connus pour être fortement influencés non seulement par la luminosité du champ d'excitation, mais aussi par son évolution temporelle décrite par la durée de l'impulsion et la phase porteuse-enveloppe (*carrier-envelope phase*, CEP). Ces deux aspects ont cependant reçu très peu d'attention dans les réalisations contemporaines de PDC, en partie parce que le régime de haut gain de la PDC est difficile à atteindre expérimentalement pour des impulsions de quelques cycles. Cette thèse se concentre donc sur la conception, la caractérisation et la modélisation d'une source de BTBs conçue dès le départ pour exciter des phénomènes d'optique non linéaire extrême avec des états de lumière non classiques.

En l'absence d'un champ initial fini, les caractéristiques de la lumière produite par PDC sont entièrement déterminées par la pompe optique qui excite l'effet et par le milieu non linéaire qui lui sert de médiateur. La conception des sources de PDC se résume donc à une sélection et à une optimisation rigoureuses de ces deux composants. Dans ce travail, une forte amplification paramétrique de BTBs ayant une durée d'impulsion de quelques cycles est obtenue en combinant un train précompressé d'impulsions de pompe d'une durée de moins de 10 fs avec un milieu non linéaire possédant une dispersion chromatique quasi-nulle à la longueur d'onde centrale du processus de parametric down-conversion (PDC).

Après sa conception et sa mise en œuvre, les BTBs sont caractérisés à l'aide de méthodes standards pour quantifier ses propriétés spatiales, spectrales et statistiques. Afin de révéler ses caractéristiques temporelles innovatrices, deux mesures inédites dans le contexte des sources lumineuses générées par PDC sont ici démontrées. Premièrement, la forme de l'impulsion est mesurée à l'aide de la technique classique de l'autocorrelation résolue en fréquence (*frequency-*

resolved optical gating, FROG), démontrant une durée de 3,4 cycles d'oscillation à pleine largeur à mi-hauteur. Deuxièmement, les fluctuations et les corrélations de la CEP des BTBs sont mesurées à l'aide d'une nouvelle technique qui est inspirée par l'interférométrie « f-to-$2f$ » et qui est un analogue temporel de la détection hétérodyne des champs quantiques à bande étroite. Cette technique est ensuite utilisée dans une preuve de concept démontrant la capacité de remodeler l'état quantique des BTBs en utilisant l'amplitude et la CEP comme critères de post-sélection.

Enfin, un logiciel de simulation numérique semi-classique modélisant les nombreux phénomènes optiques linéaires et non linéaires pertinents dans ce régime extrême de la PDC est implémenté, puis utilisé pour analyser les aspects dynamiques et les limites de la source de BTBs ici mise en œuvre. L'analyse numérique révèle le rôle crucial joué par le phénomène de lentille de Kerr et par la réponse spectrale des détecteurs dans l'observation du caractère non classique de la source. Des stratégies réalistes sont élaborées pour surmonter les limites de ces deux aspects dans les travaux futurs.

ABSTRACT

The production of entangled photon pairs in PDC is a fundamental bulding blocks behind a wide range of quantum technologies, including quantum computing, communication, and metrology.. Thanks to advances in ultrafast laser technology, PDC can now be driven into the so-called high-gain regime, where photon pairs turn into bright twin beams (BTBs) with an optical intensity that is comparable to that of off-the-shelf laser systems. Access to this macroscopic quantum state of light enables experimental investigations of extreme light-matter interactions driven by nonclassical light.

Nonpertubative nonlinear phenomena such as high-harmonic generation and electron tunneling are known to be significantly influenced not only by the brightness of the driving field, but also by its temporal evolution described by the pulse duration and the carrier-envelope phase (CEP). These two aspects however have received very little attention in contemporary PDC implementations, in part because the high-gain regime of PDC is difficult to reach experimentally for few-cycle pulses. This thesis therefore focuses on the design, characterization, and modeling of a source of BTBs which is tailored from the outset for the task of driving extreme nonlinear optics with nonclassical states of light.

In the absence of a finite seed, the characteristics of the light produced in PDC is entirely determined by the nonlinear medium mediating the effect, and by the optical pump that drives it. The design of PDC sources therefore amounts to the careful selection and optimization of these two components. In this work, a high parametric amplification of BTBs with a few-cycle pulse duration is achieved by combining a pre-compressed sub-10-fs pump pulse train with a nonlinear medium that exhibits near-zero chromatic dispersion at the wavelength of the central of PDC process.

Following its design and implementation, the BTBs are characterized using standard methods to unveil its spatial, spectral and statistical properties. To further uncover its novel temporal characterizations, two measurements that are new in the context of PDC-driven light sources are implemented. First, the pulse shape is measured using the classical technique of frequency-resolved optical gating (FROG), demonstrating a 3.4-cycle full-width at half maximum duration. Second, the fluctuations and correlations of the CEP of the BTBs are measured using a new scheme inspired by f-to-$2f$ interferometry, which achieves a temporal analogue to heterodyne detection of narrowband quantum fields. This technique is further used in a proof-of-principle demonstration of the ability to reshaping the quantum state of BTBs with both the amplitude and the CEP as post-selection criteria.

Finally, a semi-classical numerical simulation software which models the many linear and nonlinear optical phenomena that are relevant in this extreme regime of PDC is implemented, and subsequently used to analyze the dynamics and limitations of the BTBs source here demonstrated. The numerical analysis reveals the critical role played by Kerr lensing and by the spectral response of detectors in the observation of the nonclassical character of the source. Realistic strategies are devised to overcome the limitations of these two aspects in future works.

TABLE OF CONTENTS

LIST OF TABLES

LIST OF FIGURES

LIST OF SYMBOLS AND ACRONYMS

BBO	Beta barium borate
BSV	Bright squeezed vacuum
BTBs	Bright twin beams
CEP	Carrier-envelope phase
COPRA	Common pulse retrieval algorithm
FROG	Frequency-resolved optical gating
FWHM	Full-width at half maximum
GD	Group delay
GDD	Group delay dispersion
GV	Group velocity
GVD	Group velocity dispersion
GVM	Group velocity mismatch
JSA	Joint spectral amplitude
JSI	Joint spectral intensity
MIR	Mid infrared
NIR	Near infrared
NOPA	Noncollinear optical parametric amplifier
NRF	Noise reduction factor
OPA	Optical parametric amplifier
PDC	Parametric down-conversion
SF	Sum frequency
SFG	Sum frequency generation
SC	Supercontinuum
SCG	Supercontinuum generation
SH	Second harmonic
SH-FROG	Second-harmonic frequency-resolved optical gating
SHG	Second-harmonic generation
SPM	Self-phase modulation
2DSI	Two-dimensional spectral shearing interferometry
VIS	Visible
UV	Ultraviolet
YAG	Yttrium aluminium garnet

LIST OF APPENDICES

CHAPTER 1 INTRODUCTION

1.1 Context

Ever since its first demonstration in 1960 [1], the laser has been a cornerstone of scientific and technological progress, driving fiber-based telecommunications [2], barcode readers [3], optical disk players [4], Lidar [5], laser cutting [6], laser surgery [7], gravitational wave detectors [8], and much more. Even today, most laser-based technologies rely on the minute control over the *classical* degrees of freedom of light [9], e.g. its frequency, its polarization, and its intensity.

Yet, for over a century light has been known to be composed of discrete particles now called photons [10–12]. This quantization is described by the so-called quantum state of light, another degree of freedom which determines the statistical and correlation properties of light in ways that can't be explained classically [13, 14]. This new "control knob" for optical science is the basis behind the emerging industries of quantum technology, with quantum cryptography [15] and computing [16] being arguably the most prominent examples.

Quantum and classical optics have long been seen respectively as the physics of faint and bright light. Yet, as theoretical understanding and experimental capabilities progressed over time, brighter regimes of quantum optics appeared : starting from the microscopic regime with the first implementations of "true" single-photon sources in the 1980s [17,18], then evolving toward mesoscopic multi-photon nonclassical states of light [19–21], and finally leading to the demonstration of sources of macroscopic squeezed states of light [22–24] that are intense enough to be visible to the naked eye and even to drive nonlinear optical phenomena [25–27].

The development of macroscopic quantum optics opens up new opportunities in applying nonclassical light to areas previously exclusive to classical light. One such example is quantum-enhanced sensing [28–33], where these novel states combine the classical signal-to-noise advantage of intense light with the nonclassical advantages provided by squeezing and entanglement.

More recently, a surging interest appeared in the literature toward the exploration of extreme light-matter interactions driven by bright squeezed light [34–40], promising to unlock new capabilities in the control over the quantum state of light and matter [41, 42], and to help bridge the gap between attosecond and quantum science [43, 44]. These studies focused on the impact of the enhanced photon number fluctuations that these sources exhibit, yet past works of classical attosecond physics teach us that the temporal characteristics of the driving field have just as much if not more importance for extreme nonlinear phenomena [45–50].

1.1.1 Parametric down-conversion

Figure 1.1 illustrates the optical process known as parametric down-conversion (PDC), a nonlinear interaction where photons from a intense optical pump split into pairs of entangled "twin" photons at a lower frequency. This pairwise generation process is a metaphorical key to the realm of experimental quantum optics, as depending on the degeneracy (or non-degeneracy) of the generated photons, this effect directly leads to either or both of the two main nonclassical properties of light : squeezing and entanglement. Thanks to its relatively good accessibility compared to other sources of nonclassical light, and the high versatility of photon pairs as a starting point to generate new quantum states of light, PDC has been the de-facto gateway to experimental quantum optics ever since its experimental demonstration in 1970 [51].

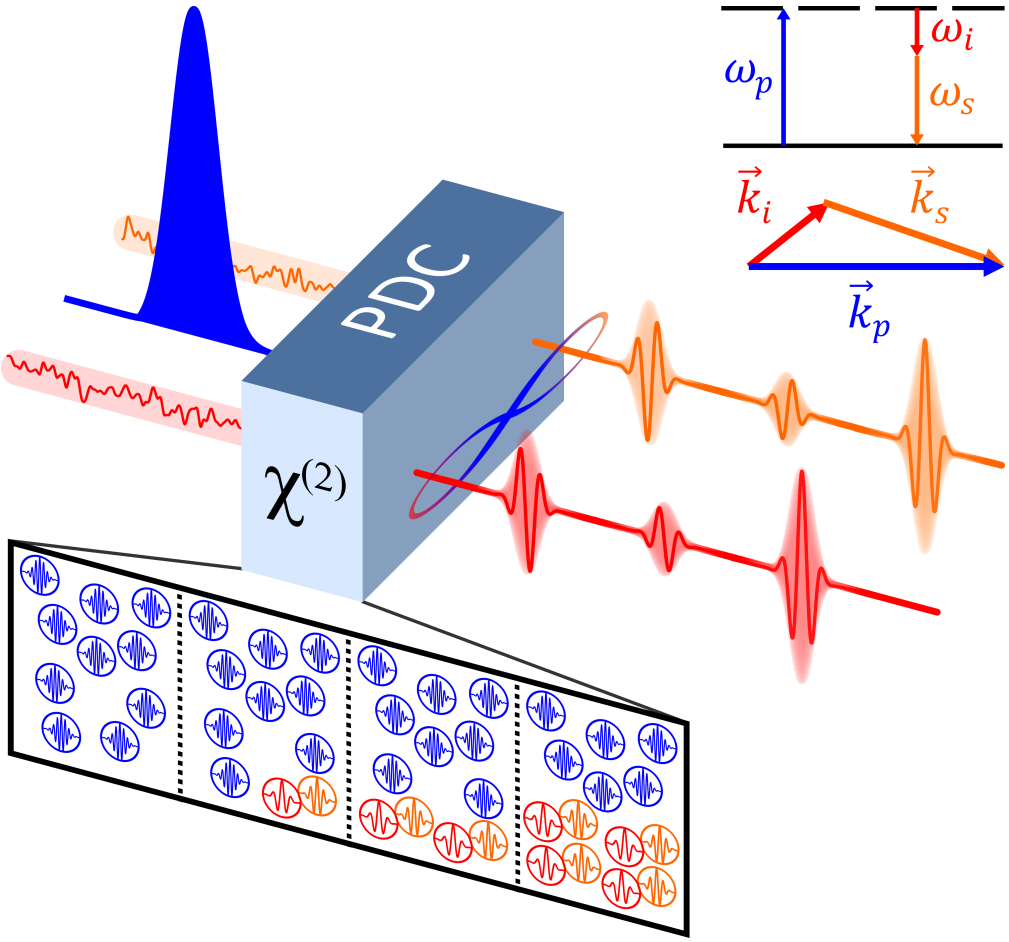

Figure 1.1 Schematic of PDC. A strong optical pump (p) propagates through a nonlinear medium ($\chi^{(2)}$) and generates pairs of photons, traditionally labeled as signal (s) and idler (i) in the non-degenerate case. Energy and momentum conservation laws link respectively the carrier frequency ($\omega_\mathrm{p} = \omega_\mathrm{s} + \omega_\mathrm{i}$) and the wave vector ($\vec{k}_\mathrm{p} = \vec{k}_\mathrm{s} + \vec{k}_\mathrm{i}$) of all three fields.

This process is initially spontaneous, driven from the interaction of the pump with the omnipresent fluctuations of the electromagnetic quantum vacuum [52–55]. As the intensity of the pump or the interaction length are increased, the strength of this interaction also increases, and photon pairs generated spontaneously at the start of the interaction can stimulate the generation of more photon pairs at a latter point. This causes a snowballing exponential growth that can reach a macroscopic brightness (to date, up to 10^{13} photon pairs [22]) that is typically associated with classical light sources. The down-converted light can be emitted in either of two states depending on whether the two photons of each pair are distinguishable or not : bright twin beams (BTBs) or bright squeezed vacuum (BSV) respectively [23].

1.1.2 Problem and State of the Art

Based on lessons learned from seminal works in classical attosecond physics [45–50], and the recent works on nonperturbative nonlinear optical optics with bright squeezed vacuum [34–40], 5 ingredients can be identified for an ideal source of BTBs or BSV to drive extreme nonlinear optical phenomena :

1. **A macroscopic brightness**
   By definition, optical nonlinear interactions become more and more efficient as the intensity of the driving field increases [56, 57]. While advances in optical confinement methods brought down the energy scale necessary to access nonlinear optics by several orders of magnitude [50, 58], with few exceptions the current experimental threshold is an average number of photons per pulse $\langle n \rangle \sim 10^6$ [39] which is still a ways away from the mesoscopic ($\langle n \rangle \sim 10^2$) and microscopic ($\langle n \rangle \sim 1$) scales.

2. **A few-cycle pulse duration**
   The duration of a light pulse not only impacts its peak optical intensity, but also defines a temporal window that gates the nonlinear interaction. As it approaches the period of the carrier field, a new regime of extreme nonlinear optics appears where the interaction is confined to a single half-cycle of the driving field, enabling e.g. the generation of *isolated* attosecond pulses [59] or the observation of nonlinear signals that otherwise interfere destructively with themselves over multiple half-cycles [50].

3. **Control over the carrier-envelope phase (CEP)**
   The CEP is a parameter known to be crucial when extreme nonlinear phenomena are driven by few-cycle pulses [46, 47, 49, 50], as it significantly affects the peak amplitude of the electric field one can achieve. As PDC is kickstarted from quantum noise, the CEP of the generated pulses is either fully random [48, 60], or locked to the (usually

pseudo-random) CEP of the pump laser. One therefore needs to either measure at least its shot-to-shot variations [45], or use a so-called CEP-stable pump.

4. **Emission of down-converted light in a single spatiotemporal mode**
   The light emitted in PDC can be viewed as amplified vacuum fluctuations. In this context, the number of spatiotemporal modes can be qualitatively understood as the number of independent fluctuations (i.e. degrees of freedom) that are being amplified. For multimode PDC, all these fluctuations add up incoherently with each other, and produce entirely different results at each laser shot. For single-mode PDC, the beam shape, the spectrum, and most crucially the pulse envelope (necessary to define the CEP) all remain the same at each laser shot; only the phase and number of photons fluctuate. Single-mode BTBs and BSV further exhibit increased fluctuations of their intensity compared to their multimode counterparts, which further provides a so-called statistical enhancement of nonlinear processes [25, 35, 40].

5. **Exploitable nonclassical features**
   The main interest of these investigations is to transfer nonclassical features from the driving field (e.g. squeezing) to new regions of the electromagnetic spectrum [38, 41] and matter [37], or to unlock some advantage in the driven process such as an enlarged emission bandwidth [35, 40] or non-Poissonian statistics [37, 42]. This, of course relies on the pump field being nonclassical in itself.

However, the generation of a state of light which combines all these characteristics at once is experimentally challenging. On the one hand, parametric amplification of a single mode with a few-cycle temporal extent requires the use of femtosecond pump pulses to match the bandwidth of the down-converted field [61–64]. On the other hand, pushing the parametric gain toward a macroscopic number of photons requires long interaction lengths, and the ensuing chromatic dispersion accumulated throughout the interaction severely limits the achievable bandwidth. Furthermore, the observation of nonclassicality is harder at higher brightness, both for technical and fundamental reasons [65]. Therefore, most PDC implementations found in the literature sacrifice at least one of these features in favor of the others.

To provide a rapid overview of the current state of the art, table 1.1 lists 16 recent reports on the implementation of a squeezed vacuum or twin beams source which achieve at least one of the listed criteria. So far, few works have demonstrated a macroscopic ($\gtrsim 10^6$) average number of photons $\langle n \rangle$ [22, 24, 25, 40, 63, 66–70] or a near-unity ($\lesssim 1.1$) number of spatiotemporal modes K [20, 25, 40, 62]. Only two works demonstrated both of those characteristics in a single source [25, 40], but they did not demonstrate the nonclassicality of the resulting

BSV.

What's more, for nearly all implementations of BTBs and BSV found in the literature, the only information provided on the duration of the generated pulse train is the duration of the pump pulse, which can reasonably be used as an upper bound. Outside of the present thesis, there has been only one report of a pulse duration measurement being performed on a PDC-driven light source [40]. It has been done in collaboration with the author [71] subsequently to this work [72], and revealed a 4.7-cycle pulse duration for a BSV at 1600 nm. Finally, while the CEP properties of the light generated from few-cycle PDC has been investigated numerically [60] , no experimental measurement has been reported until now.

Table 1.1 Experimental progress over the last 21 years on the implementation of light sources driven by PDC.

[Ref.] Year	$\langle n \rangle$	K	Duration	Nonclassicality
[66] 2004	$\sim 10^7$	16	4.45 ps (pump)	—
[67] 2005	$\sim 10^7$	14	4.5 ps (pump)	—
[68] 2010	$\sim 10^6$	3750	17 ps (pump)	NRF = 0.5
[62] 2011	2.5	1.05	444 fs (pump)	—
[22] 2012	$\sim 10^{13}$	1.25[1]	18 ps (pump)	—
[73] 2014	2.5×10^5	1.41	18 ps (pump)	NRF = 0.5 (for $K > 400$)
[24] 2015	$\sim 10^{12}$	1.75[1]	18 ps (pump)	—
[74] 2015	$\sim 10^4$	4.31	300 fs (pump)	NRF = 0.7
[20] 2016	20	1.15	1 ps (pump)	NRF = 0.4
[75] 2016	$\sim 10^5$	$100 - 1000$	18 ps (pump)	NRF = 0.5 (for $K > 500$)
[21] 2016	6.3×10^5	4.5×10^5	18 ps (pump)	NRF = 0.3
[63] 2017	$\sim 10^8$	$1.3 - 4$	140 fs (pump)	—
[25] 2017	$\sim 10^{11}$	1.03	1.6 ps (pump)	—
[69] 2018	$\sim 10^9$	> 40	16 ps (cross-corr.)	—
[70] 2020	$\sim 10^{10}$	18	22 ps (pump)	—
[40] 2024	2×10^{12}	~ 1	25 fs (measured)	—

[1] Values measured after significant mode filtering, and therefore incompatible with the reported $\langle n \rangle$.

1.2 Research Objectives

This work aims to accomplish four specific objectives. The first and main objective targets the experimental development of a novel source of quantum light :

1. **Design and implement a source of quantum light optimized toward the driving of extreme nonlinear optical phenomena**
   The implemented source should demonstrate the five characteristics of an ideal nonclassical pump for extreme nonlinear optics identified above, namely 1) high brightness, 2) a single spatiotemporal mode composition, 3) a few-cycle pulse duration, 4) control over its CEP, and 5) a nonclassicallity that can be turned into a quantum advantage.

Achieving this objective however requires the demonstration of two novel measurements in the context of PDC-driven light sources. These demonstration are therefore the two next objectives of this thesis :

2. **Demonstrate a pulse duration measurement on PDC-driven light**
   While the measurement of pulse durations is a routine exercise in classical ultrafast optics, it is completely novel for BSV and BTBs. A particular challenge in this new context is to analyze how the measurement react to the potential presence of multiple modes.

3. **Demonstrate a CEP measurement on PDC-driven light**
   Similarly, there are well-established methods for the measurement, control, and stabilization of the CEP of pulsed light in classical ultrafast optics, but their extension to BSV or BTBs has not been demonstrated. Here, a particular attention must be paid to the phase relation between the down-converted light and its pump, and to the definition of phase in quantum optics.

Finally, the fourth objective aims to improve theoretical prediction capabilities to support the design of the source and the analysis of its characterization results :

4. **Develop a numerical model of ultrafast PDC in the high-gain regime**
   Driving PDC in the extreme limits of high parametric gain, few-cycle pulse duration, and strong spatiotemporal localization implies that the output states will be influenced by the interplay of chromatic dispersion, diffraction, and high-order nonlinearities. No readily-available model of PDC addresses all of these effects simultaneously, and the implementation of one will help not only this work, but also future implementations of few-mode ultrafast BSV and BTBs.

1.3 Thesis Outline

First, Chapter 2 presents a detailed literature review of the concepts treated throughout the rest of this thesis, starting with a textbook-like introduction to the theoretical concepts of ultrafast, nonlinear, and quantum optics that are applied in subsequent chapters. It is followed by a practical description of nondegenerate spontaneous parametric down-conversion (SPDC), and the quantum states of light resulting from that process : photon pairs in the low-gain regime, and BTBs in the high-gain regime. Various methods to characterize the quantum state of light are then introduced, and their particular application to BTBs is discussed. The review finally concludes with a brief with the longstanding problem of defining the concept of optical phase in the context of quantum optics.

Next, Chapter 3 compiles the technical details on the implementation of pre-established methods in this thesis toward the experimental generation and theoretical modeling of few-cycle, single-mode BTBs. It includes a derivation of the numerical model used with details of its software implementation, a presentation of how standard characterization methods are realized in this work, and the design guidelines of the BTBs source with a particular focus on the characterization of its classical pump source.

Then, Chapter 4 presents all experimental results on the generation and characterization of few-cycle, single-mode BTBs, including many characterization results that appear in the literature, e.g. photon statistics, the noise reduction factor (NRF), and the Schmidt decomposition of spectral modes, as well as a new measurement in the context of PDC-driven light : pulse duration via frequency-resolved optical gating (FROG). The chapter concludes with the presentation of a novel scheme to measure the CEP of BTBs, and results from its application to the present source.

Afterwards, Chapter 5 is a numerical analysis of the source implemented in Chapter 4. It first investigates the pulse propagation dynamics of the pump and the BTBs during the PDC process, and the role played by the higher-order nonlinear effects. Alternative designs of the BTBs source are then explored toward the future experimental demonstration of a nonclassical relation uniting the twin beams. The chapter conclude with an analysis of the role played by the detection bandwidth on the measured value of the NRF for few-cycle BTBs.

Finally, the thesis concludes with a global discussion of the results presented here, the limitations of this work alongside potential solutions, and potential future research avenues.

CHAPTER 2 LITERATURE REVIEW

2.1 Ultrafast Linear and Nonlinear Optics

Pulses of light are electromagnetic waves with a well-defined finite support in time [56], more often referred to as its duration. In the scalar approximation, i.e. when considering a single polarization of the field, they can be represented in spacetime by a complex wave function

$$u(\mathbf{r},t) = A(\mathbf{r},t)e^{i(\omega_0 t+\phi_0)} \tag{2.1}$$

where $A(\mathbf{r},t)$ is the complex envelope of the pulse at position $\mathbf{r}$ and time t normalized such that the optical intensity $I(\mathbf{r},t) = |A(\mathbf{r},t)|^2$, and ω_0 and ϕ_0 are the angular frequency and the phase of the carrier wave. In a medium with a (frequency-independent) refractive index n, the real part of u is directly related to the electric field by

$$E(\mathbf{r},t) = \sqrt{\frac{2}{nc\epsilon_0}}\mathrm{Re}\left\{u(\mathbf{r},t)\right\} \tag{2.2}$$

where ϵ_0 is the permittivity of free space, and c is the speed of light in vacuum. Equivalently, the pulse can be represented in frequency domain by the Fourier transform of u

$$\tilde{u}(\mathbf{k},\omega) = \mathcal{F}_{\mathbf{r},t}\left\{u(\mathbf{r},t)\right\} = \tilde{A}(\mathbf{k},\omega-\omega_0) = \left|\tilde{A}(\mathbf{k},\omega-\omega_0)\right| e^{-i\phi(\mathbf{k},\omega)} \tag{2.3}$$

where $\tilde{A}(\mathbf{k},\omega)$ is the Fourier transform of the spatio-temporal envelope $A(\mathbf{r},t)$, $\mathbf{k}$ is the wavevector, ω is the angular frequency, $\left|\tilde{A}(\mathbf{k},\omega-\omega_0)\right|$ is the amplitude spectrum of the pulse, and $\phi(\mathbf{k},\omega)$ is its spectral phase. The pulse envelope and the complex spectrum forming a Fourier pair is a mathematical expression of the fact that optical pulses result from the superposition of multiple monochromatic waves. An important consequence of this relationship is that the product of the pulse duration Δt and the bandwidth $\Delta\nu = \Delta\omega/2\pi$ is lower bounded as

$$\Delta t\Delta\nu \geq \mathrm{TBP}_0 \tag{2.4}$$

where the minimal time-bandwidth product TBP_0 is a dimensionless constant which depends on the shape of the optical spectrum and on the definition used for Δt and $\Delta\nu$, e.g. the full-width at half maximum (FWHM) or the square-root of the second moment of the pulse

shape. A pulse which satisfies the equality $\Delta t \Delta \nu = \mathrm{TBP}_0$ is often said to be compressed, transform-limited, or Fourier-limited. This condition is achieved when and only when all frequency components are in phase at a specific point in time.

As illustrated in Figure 2.1, in order to produce pulses with an ever shorter duration, one therefore not only needs to increase their bandwidth, but also to ensure that all frequency components are in phase. Experimentally, the former is achieved either by the use of lasers based on gain media with a large amplification bandwidth such as titanium-doped sapphire [76], or by extending the spectrum of a narrowband source via nonlinear processes [57, 77, 78]. The latter is then attained by careful characterization of the spectral phase via pulse measurement techniques (see section 2.1.3), and then compression of the pulse by cancellation of its chromatic dispersion (see section 2.1.4).

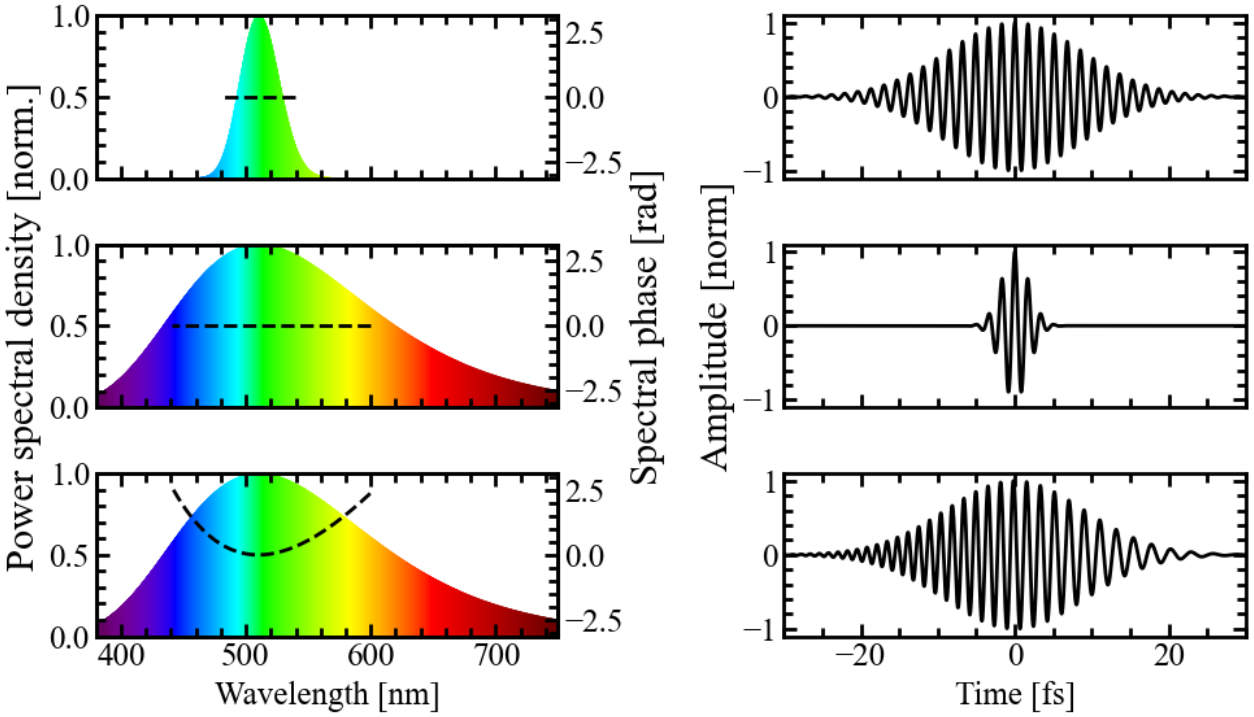

Figure 2.1 Spectral (left column) and temporal (right column) representation of 3 distinct light pulses : a compressed multi-cycle pulse (top row), a compressed few-cycle pulse (middle row), and a dispersed pulse with a bandwidth supporting a few-cycle duration (bottom row). Due to chromatic dispersion, the last pulse has the same duration as the first one, and it has a time-dependent instantaneous frequency that is reminiscent of the chirp of a bird.

2.1.1 Linear Pulse Propagation in Transparent Media

When considering directional propagation [79] of e.g. laser light, linear propagation of light pulses is best expressed in the frequency domain, where the envelope evolves according to the Helmholtz equation

$$\frac{\partial^2 \tilde{A}}{\partial z^2} = -k^2 \tilde{A} - (k_x^2 - k_y^2)\tilde{A} \tag{2.5}$$

where $k = 2\pi\omega n(k_x, k_y, \omega)/c$ is the wavenumber of the pulse, and k_x and k_y are its transverse components along the x- and y-axes. The first term describes chromatic dispersion stemming from the (potentially anisotropic) refractive index n, and the second describes diffraction. This equation is solved exactly by the solution $\tilde{E}(z) = \tilde{E}_{\rightarrow}(0)e^{-ik_z z} + \tilde{E}_{\leftarrow}(0)e^{ik_z z}$, which describes independent propagation of forward ($\tilde{E}_{\rightarrow}$) and backward ($\tilde{E}_{\leftarrow}$) propagating waves along the z-axis with a longitudinal wavenumber $k_z = \sqrt{k^2 - k_x^2 - k_y^2}$. For the case of an unidirectional pulse propagating forward through a dispersive medium of length L, the output pulse is therefore given by

$$\tilde{u}(k_x, k_y, \omega, z + L) = \tilde{u}(k_x, k_y, \omega, z)e^{-ik_z L} \ . \tag{2.6}$$

In simple experimental scenarios where space-time coupling [80] is negligible, equation (2.5) can be further simplified by assuming that the spatio-temporal envelope $A(\mathbf{r}, t)$ is separable into a product of a spatial (transverse) and a temporal (longitudinal) envelopes

$$A(\mathbf{r}, t) \approx A_{\mathrm{T}}(x, y)A_t(t) \tag{2.7}$$

which allows for independent treatment of diffraction and chromatic dispersion. The transverse envelope is typically treated within the paraxial approximation [56], where it is simply modeled as a Gaussian beam with an appropriate beam waist w_0

$$A_{\mathrm{T}}(x, y, z) \propto \frac{1}{q(z)} e^{-ik\frac{x^2+y^2}{2q(z)}} \tag{2.8}$$

where $q(z) = (z - z_0) + iz_{\mathrm{R}}$ is the complex beam parameter, z_0 is the location of the focal plane, and $z_{\mathrm{R}} = \pi n \mathrm{w}_0^2/\lambda_0$ is the Rayleigh range for a beam with a carrier wavelength in vacuum λ_0. As for the temporal envelope, its evolution is again calculated in frequency

domain

$$\mathcal{F}_t \left\{ A_t(t, z+L) \right\} = \tilde{A}_\omega(\omega, z+L) = \tilde{A}_\omega(\omega, z) e^{-ikL} \tag{2.9}$$

where k is here evaluated along the z-axis, i.e. for $k_x = k_y = 0$.

Spectral Phase and Carrier-Envelope Phase

For a transparent medium where $\mathrm{Im}\{n\} = 0$, the amplitude spectrum $\left|\tilde{A}(\mathbf{k}, \omega - \omega_0)\right|$ of the pulse remains constant. In this case, the only variable parameter under propagation is its spectral phase $\phi(\omega)$, which evolves as

$$\phi(\omega, z+L) = \phi(\omega, z) - k(\omega) L \ . \tag{2.10}$$

When $\phi(\omega)$ evolves slowly within the pulse bandwidth, an intuitive understanding of the effects of chromatic dispersion on light pulses can be obtained from a Taylor expansion of the phase and of the propagation constant k around the carrier ω_0

$$\phi(\omega) = \phi(\omega_0) + \frac{\partial \phi}{\partial \omega}(\omega - \omega_0) + \frac{1}{2}\frac{\partial^2 \phi}{\partial \omega^2}(\omega - \omega_0)^2 + \frac{1}{6}\frac{\partial^3 \phi}{\partial \omega^3}(\omega - \omega_0)^3 + (...) \tag{2.11}$$

$$k(\omega) = k(\omega_0) + \frac{\partial k}{\partial \omega}(\omega - \omega_0) + \frac{1}{2}\frac{\partial^2 k}{\partial \omega^2}(\omega - \omega_0)^2 + \frac{1}{6}\frac{\partial^3 k}{\partial \omega^3}(\omega - \omega_0)^3 + (...) \ . \tag{2.12}$$

The zeroth- and first-order terms do not affect the compression of the pulse, as the zeroth-order terms only describe its carrier phase $\phi(\omega_0)$ and its phase velocity $v_\mathrm{p} = \omega/k$, while the first-order terms describe its group delay (GD) (i.e. its time of arrival) and group velocity $v_\mathrm{g} = (\partial k/\partial \omega)^{-1}$. These two terms are however significant for extreme nonlinear optics with few-cycle pulses as they determine the carrier-envelope phase [45, 48]

$$\phi_\mathrm{CEP} = (\phi(\omega_0) - \mathrm{GD}\omega_0) \mod 2\pi \tag{2.13}$$

which describes the relative timing between the carrier wave and the envelope of the pulse. As illustrated in Figure 2.2, when $\phi_\mathrm{CEP} = 0$ ($\phi_\mathrm{CEP} = \pi/2$) one obtains a cosine-like (sine-like) pulse where the electric-field is maximal (null) at the peak of the envelope. For extremely nonlinear phenomena such as high-harmonic generation (HHG) [49], or electron tunneling [50], this change in symmetry can make the difference between maximization and total cancellation of nonlinear signals.

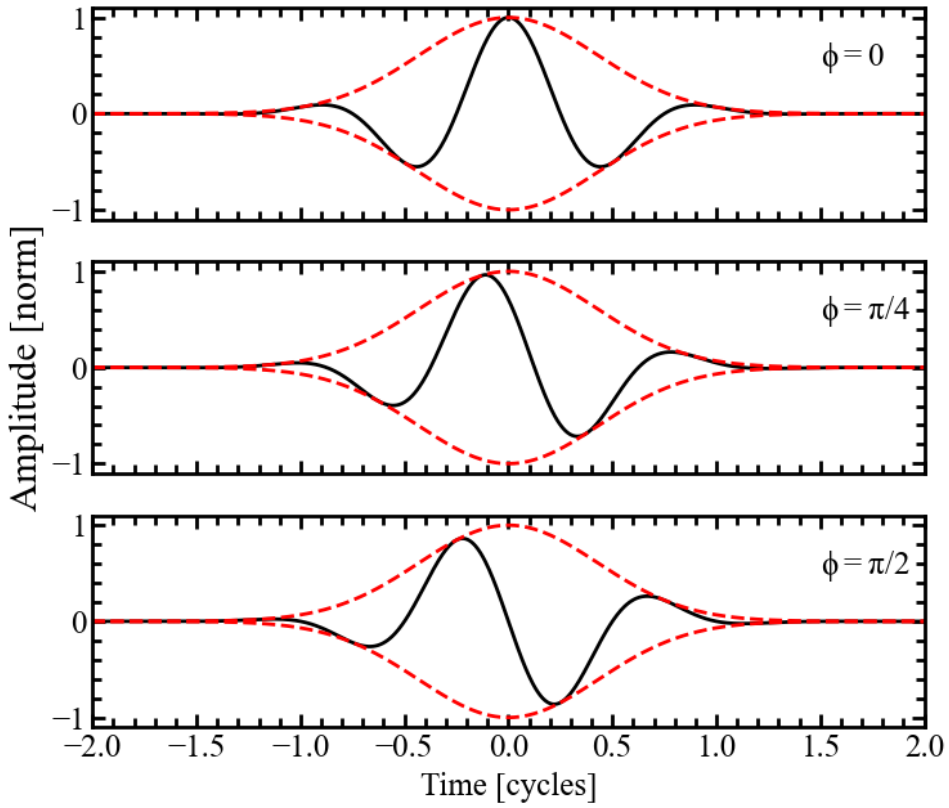

Figure 2.2 Impact of the CEP ϕ on the electric field of few-cycle pulses. The solid black line is the carrier wave, and the dashed red line is the envelope.

The second and higher order terms in the expansion of ϕ (k) then describe how the GD of the pulse (group velocity of the medium) varies as a function of frequency within the pulse bandwidth. The second-order term, designated as group delay dispersion (group velocity dispersion), describes a linear dependence; the third-order term describes a quadratic dependence, and so forth. All terms tend to stretch the pulse in time, with even-order terms stretching it symmetrically in time, and odd-order terms stretching it asymmetrically. Most pulse compression techniques specifically target cancellation of the group delay dispersion of the pulse [81, 82], since it is the dominating effect for all but few-cycle pulses. More advanced methods can target specific higher-order terms or even provide fully-custom dispersion profiles over broad bandwidths [83, 84].

2.1.2 Second- and Third-Order Nonlinear Responses

The electric response of a medium is encompassed in its constitutive relation, which relates its polarization density $\mathbf{P}$ to the applied electric field $\mathbf{E}$ [56, 57]. In the simplest case of a linear, nondispersive, homogeneous and isotropic dielectric medium, the two vectors are

parallel and proportional

$$\mathbf{P} = \epsilon_0 \chi \mathbf{E} \tag{2.14}$$

where χ is the electric susceptibility of the medium and in this case is a constant which can be related to the refractive index $n = \sqrt{1+\chi}$. This proportionality remains valid for electric fields that are much weaker than interatomic electric fields ($\sim 10^5\,\mathrm{V\,m^{-1}}$) and leads to linear optics as presented in section 2.1.1. However, dieletric media progressively displays a response which is more and more nonlinear as the intensity of light increases. In this regime known as perturbative nonlinear optics, this behavior can be expressed by expanding the constitutive relation as a Taylor series about $|\mathbf{E}| = 0$ [85]. In the scalar approximation, this takes the form

$$P = \epsilon_0 \left(\chi E + \chi^{(2)} E^2 + \chi^{(3)} E^3 + ... \right) \tag{2.15}$$

where the first term is the linear polarization $P_\mathrm{L} = \epsilon_0 \chi \mathbf{E}$, and $\chi^{(n)}$ is the n-th order nonlinear susceptibility. All the nonlinear terms are often group together as the nonlinear polarization

$$P_\mathrm{NL} = \sum_{n=2}^{\infty} \epsilon_0 \chi^{(n)} E^n \tag{2.16}$$

but theoretical models typically consider only one or two terms. This nonlinear relation allows for interactions between superimposed light waves, leading most notably to the generation of new frequency components. Classically this is described as a coupling between multiple light modes (wave mixing), and quantum mechanically it can be understood as multi-photon processes that are mediated by the nonlinear medium. To illustrate the richness of nonlinear optics, it is helpful to consider the form that the n-th order nonlinear polarization term takes for an input field composed of n distinguishable wavepackets. For instance, for second order nonlinearities, consider the sum of two wavepackets

$$E = E_1 \cos(\omega_1 t + \phi_1) + E_2 \cos(\omega_2 t + \phi_2) \tag{2.17}$$

where that spatio-temporal dependence of the (real) field envelopes E_1 and E_2 has been omitted to simplify the notation. This field yields the 2nd order nonlinear polarization

$$P_{\mathrm{NL}}^{(2)} = \frac{\epsilon_0 \chi^{(2)}}{2} \Big(E_1^2 \left(\cos(2\omega_1 t + 2\phi_1) + 1\right) + E_2^2 \left(\cos(2\omega_2 t + 2\phi_2) + 1\right) \\ + 2E_1 E_2 \left(\cos\left((\omega_1 + \omega_2)t + \phi_1 + \phi_2\right) + \cos\left((\omega_1 - \omega_2)t + \phi_1 - \phi_2\right)\right) \quad (2.18)$$

where the result of every second order effect can be seen from new terms that appeared. First is second-harmonic generation (SHG), which creates new frequency components at twice the input frequency ($2\omega_1$ and $2\omega_2$). Then, there is sum frequency generation (SFG) and difference frequency generation (DFG), which creates new frequency components at the sum and difference of the two input frequencies ($\omega_1 + \omega_2$ and $\pm(\omega_1 - \omega_2)$). Finally, there is optical rectification (also called intra-pulse DFG) which creates a pulse with a very low carrier frequency (usually in the mid infrared to sub-terahertz range).

A similar treatment can be done for higher-order nonlinearities, but leads to much longer expressions where most terms are simply called n-wave mixing. Moreover, in typical experimental conditions only a handful of nonlinear effects will actually be observable in a single system. Indeed, for these processes to occur efficiently, they must respect conditions related to energy and momentum conservation. For e.g. SFG, these conditions are

$$\hbar\omega_1 + \hbar\omega_2 = \hbar(\omega_1 + \omega_2) \quad (2.19)$$

$$\hbar\mathbf{k}_1(\omega_1) + \hbar\mathbf{k}_2(\omega_2) = \hbar\mathbf{k}_{\mathrm{SFG}}(\omega_1 + \omega_2) \quad (2.20)$$

and while the former is trivially satisfied, the latter will typically be satisfied for only one or a few interactions at once in a given system. This condition, known in the nonlinear optics community as the phase matching condition, measures whether the new frequency components generated at one point in the nonlinear medium will add constructively or destructively with those generated at a latter point.

Just like for linear propagation of pulses in section 2.1.1, it is practical to expand the propagation vectors $\mathbf{k}$ in equation (2.20) around some carrier angular frequencies Ω_1 and Ω_2, and combine like terms. After simplifying all the constants and assuming collinear propagation to obtain scalar equations, the frequency-independent terms yield the condition

$$\Omega_1 n_1(\Omega_1) + \Omega_2 n_2(\Omega_2) = (\Omega_1 + \Omega_2) n_{\mathrm{SFG}}(\Omega_1 + \Omega_2) \quad (2.21)$$

which is known as phase-velocity matching, while the linear terms yield the condition

$$\left(\frac{\partial k_1}{\partial \omega_1} - \frac{\partial k_{\mathrm{SFG}}}{\partial \omega_1}\right)(\omega_1 - \Omega_1) = \left(\frac{\partial k_{\mathrm{SFG}}}{\partial \omega_2} - \frac{\partial k_2}{\partial \omega_2}\right)(\omega_2 - \Omega_2) \tag{2.22}$$

which is known as group-velocity matching. While phase- and group-velocity matching can be satisfied in typical nonlinear media for a wide range of frequency combinations (e.g. [86,87]), higher-order phase-matching conditions would require dispersionless propagation of all three waves which is a much stricter condition to achieve experimentally. Indeed, for e.g. second order terms, we find the condition

$$\frac{\partial^2 k_{\mathrm{SFG}}}{\partial \omega_{1,2}^2}(\omega_1 - \Omega_1 + \omega_2 - \Omega_2)^2 = \frac{\partial^2 k_1}{\partial \omega_1^2}(\omega_1 - \Omega_1)^2 + \frac{\partial^2 k_2}{\partial \omega_2^2}(\omega_2 - \Omega_2)^2 \tag{2.23}$$

which can be satisfied if and only if $\partial^2 k_{\mathrm{SFG}}/\partial \omega_{1,2}^2 = \partial^2 k_1/\partial \omega_1^2 = \partial^2 k_2/\partial \omega_2^2 = 0$. Group-velocity dispersion is therefore most often the limiting factor for the phase-matching bandwidth of nonlinear interactions with femtosecond pulses.

A notable exception to these considerations appears for odd-order nonlinear interactions, where a term which is trivially phase-matched appears because it involves only a single wave interacting with itself. This effect, known as the optical Kerr effect, must therefore always be considered in the propagation of high-power lasers. It acts as a intensity-dependent change of the refractive index

$$\Delta n(I) = n_2 I + n_4 I^2 + n_6 I^3 + ... \tag{2.24}$$

where the i-th order nonlinear index n_i is related to $\chi^{(i+1)}$. The $\chi^{(5)}$ and higher-order contributions are often neglected, since they become significant only for extreme intensities of multiple tens of $\mathrm{TW\,cm^{-2}}$ [88].

For realistic laser light where the intensity is a function of time and space, the Kerr effect will therefore induce a space- and time-dependent refractive index, which can have dramatic consequences for short and tightly-focused laser pulses. The (transverse) spatial dependence can be understood as reproducing the effect of a lens (most often converging, with $n_2 > 0$ [57]) and is therefore often called Kerr-lensing or self-focusing [89]. By analogy, the temporal dependence can then be understood as a time lens, which focuses the pulse in time by expanding its optical spectrum in a process called self-phase modulation (SPM).

The interplay between the Kerr effect, any other phase-matched nonlinearity, diffraction, and dispersion leads to highly complex pulse propagation phenomena including notably filamentation (diffractionless propagation) [90], soliton formation (dispersionless propagation) [91]

and supercontinuum generation (dramatic increase of the optical bandwidth) [77, 78].

2.1.3 Pulse Measurements Methods

One of the most powerful applications of ultrashort light pulses is time-resolved pump-probe spectroscopy [59, 92–99], where the short duration of a pair of light pulses is used to a temporal gate during which a physical system is excited and then observed. Experimental determination of the pulse duration (or more generally its full temporal shape) is therefore an important task as it ultimately determines the temporal resolution for these experiments.

The most straightforward approach to measure the duration of an unknown pulse consist in directly measuring its temporal intensity profile $I(t)$ with a photodiode. The signal S one observes then is

$$S(\tau) \propto \int I(t)g(t-\tau)dt \tag{2.25}$$

where $g(t)$ here is the impulse response of the photodetector. In the limit where $g(t)$ has a much smaller support in time than the pulse $I(t)$, then $S(\tau) \to I(\tau)$. Otherwise, one needs very precise characterization of $g(t)$ to deconvolve it, and even then experimental noise will typically prevent deconvolution of pulse shapes that are much shorter than $g(t)$, limiting this strategy to picosecond pulses at the shortest [100]. One therefore needs a different approach to resolve the fast evolution of a femtosecond pulse and even more so to detect any potential change to the instantaneous frequency of the field underneath the envelope.

On the other hand, measurement of the optical spectrum remains relatively easy to implement even down to the few-cycle regime. Full characterization of the pulse compression therefore only requires an additional measurement of the spectral phase, after which the pulse shape can be calculated via the inverse Fourier transform. This section presents the working principles behind the methods used in this thesis to determine the spectral phase, which also serve as examples of the two main approaches to pulse measurement in the femtosecond regime.

Intensity Autocorrelation and Frequency-Resolved Optical Gating

A natural extension of the photodiode measurement consist in replacing the slow, linear detector with another, faster process that is sensitive to the instant intensity $I(t)$. A typical example consist in measuring the intensity cross-correlation with a known shorter pulse using a SFG process [101]. However, experimental access to a temporal gate is *a priori* known to be shorter than the pulse to be measured is not commonplace. Therefore, most of these

so-called optical gating techniques are self-referenced, i.e. they use a copy of the pulse itself as the measurement gate $g(t) = I(t)$. In that case, the measured signal is proportional to the intensity autocorrelation

$$S(\tau) \propto G^{(2)}(\tau) \equiv \int I(t)I(t-\tau)dt \tag{2.26}$$

which provides an upper bound for the pulse duration, but it is insufficient to recover the pulse shape even in conjunction with the spectrum [102, 103]. The autocorrelation remained the main pulse measurement technique until the introduction of frequency-resolved optical gating (FROG) in 1991 [104–106]. Its most common and simplest implementation, known as second-harmonic frequency-resolved optical gating (SH-FROG) [107], is sketched in Figure 2.3. It is an intensity autocorrelator where the photodetector is replaced with a spectrometer, yielding a 2D spectrogram

$$I_{\mathrm{SH-FROG}}(\omega,\tau) \propto \left|\mathcal{F}_t\left\{A_t(t)A_t(t-\tau)e^{i2\omega_0 t}\right\}\right|^2 \tag{2.27}$$

most commonly called a FROG trace. Determining the pulse shape $A_t(t)$ from the FROG trace is a so-called 2D phase-retrieval problem for which many retrieval algorithms exist [108–113] and are proven to converge to unique solutions [114], despite the absence of an analytical inversion solution.

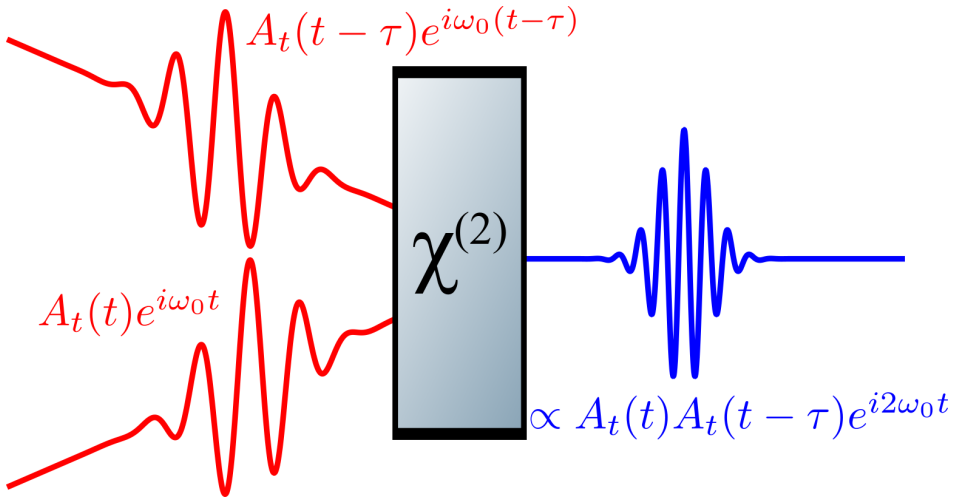

Figure 2.3 Principle of FROG measurements based on SHG.

.

The simplicity and low cost of SH-FROG make it the modern "gold standard" of pulse measurement techniques. FROG methods in general also have the advantages of requiring no

assumption to be made on the pulse shape, and of being able to retrieve a correct average pulse duration for unstable pulse train [115]. However, FROG measurements become experimentally more and more challenging as pulses shorten and bandwidths enlarge : the algorithms take longer to run, and dispersion internal to the FROG implementation stops being negligible in the retrieval. Some variant methods which tackle these specific issues can be found in the literature, e.g. d-scan [116] and FROST [117], but are not as widely adopted yet.

Two-Dimension Spectral Shearing Interferometry

An orthogonal approach to pulse measurement consist in measuring the spectral phase $\phi(\omega)$ of the pulse "directly" via interferometry, and combining this measurement with a (often separate, but potentially simultaneous) measurement of the optical spectrum to compute the pulse shape via the inverse Fourier transform. Spectral phase interferometry for direct electric-field reconstruction (SPIDER) [118] is the most well-known technique of this form, but its original implementation suffers from strict calibration requirements.

Recently, a more robust variant known as two-dimensional spectral shearing interferometry (2DSI) was demonstrated [119, 120] and is sketched in Figure 2.4. The pulse to be measured $\tilde{A}_\omega(\omega)$ (in frequency domain) is upconverted by two (quasi-)monochromatic beams with angular frequencies ω_0 and $\omega_0 + \Omega$ to create a pair of spectrally-overlapping copies of the pulse with a frequency detuning Ω. Measuring their combined optical spectrum yields an interference pattern given by the equation

$$S_{\text{2DSI}}(\omega', \tau) \propto |\tilde{A}_\omega(\omega')\tilde{A}_\omega(\omega' - \Omega)| \cos\left(\omega_0\tau + \phi(\omega') - \phi(\omega' - \Omega)\right) \tag{2.28}$$

which is measured as a function of the temporal delay τ between the two monochromatic beams, and where $\omega' = \omega + \omega_0$ is the upconverted angular frequency. If the shear $\Omega \ll \omega$, then the phase difference $\phi(\omega') - \phi(\omega' - \Omega)$ is approximately proportional to the spectrally-resolved group-delay of the upconverted pulses

$$\phi(\omega') - \phi(\omega' - \Omega) = \text{GD}(\omega')\Omega + \mathcal{O}(\Omega^2) \tag{2.29}$$

which can then be numerically integrated and frequency-shifted to obtain the spectral phase of the original pulse $\phi(\omega)$.

Compared to FROG, 2DSI has the advantages of providing a direct measurement of the spectral dispersion of the pulse (avoiding the need for an iterative algorithm), and of not

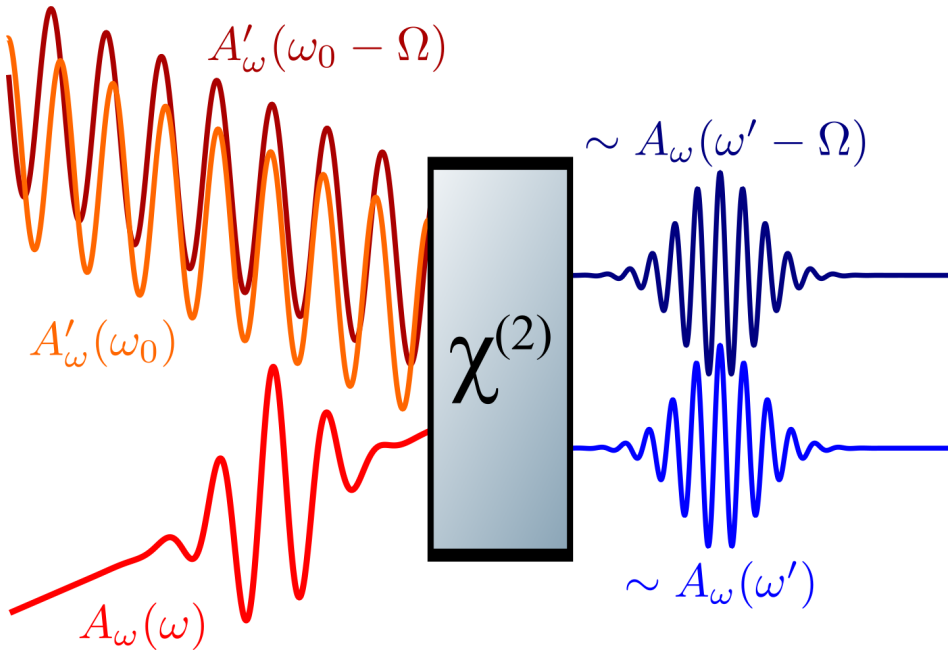

Figure 2.4 Principle of 2DSI measurements.

adding additional dispersion. Its standard implementation is however significantly more complex than SH-FROG, and can only be reliably used for very short pulses ($\leq \sim$10 fs). Indeed, the two (quasi-)monochromatic beams are most-commonly obtained from splitting the original pulse in three and propagating two copies through a series of dispersive elements. For this to work however, the input pulse needs to be 1) broadband and 2) nearly compressed such that the instantaneous frequency of these dispersed copies varies by less than the shear Ω over the duration Δt of the pulse. The measured trace however lacks any way to ensure this condition is satisfied, and in practice one should perform multiple measurements with different shears and levels of dispersion to ensure convergence of the measurement [120].

2.1.4 Pulse Compression Methods

Once the dispersion $\phi(\omega)$ of a pulse is characterized, its propagation through a physical system with the opposite dispersion will compress it to its transform limited duration. Modern experiments also often "pre-compress" pulses, i.e. cancel dispersion from optical elements *before* the pulse train propagates through them, in order to obtain compressed pulses at a specific latter point. To cancel i.e. group delay dispersion, the simplest method consist in propagating the pulse through a medium for which the sign of group velocity dispersion (GVD) is opposite at the carrier frequency of the pulse and with the proper thickness. However, in the visible and in the high-frequency end of the near infrared regions of the

electromagnetic spectrum, most transparent bulk media exhibit positive GVD and therefore other methods are needed if ones needs to impart negative group delay dispersion (GDD) or a more complex phase mask to a pulse train.

The three most common free-space solutions to this issue are sketched in Figure 2.5. All of them can be understood conceptually as using spatial separation of frequency components of a pulse to then geometrically impart a frequency-dependent group delay. In (a) grating [81] and (b) prism [82] compressors, the frequency components are first separated angularly and then made parallel to each other from reflecting off a diffraction grating or propagating through a prism made of dispersive material. Propagation through a mirrored setup or back reflection through the same configuration then recombines the pulse as one. In both cases, the geometry can be adjusted to yield a longer optical path length for longer (red) wavelengths than shorter (blue) ones, which corresponds to negative GDD. These two strategies are simple to implement and not too expensive, but they often introduce additional third- and higher-order dispersion to the pulse which can be significant for few-cycle pulses. Compared to one another, prism compressors typically have lower losses while grating compressors allow for much higher tunability and maximal absolute value of the GDD.

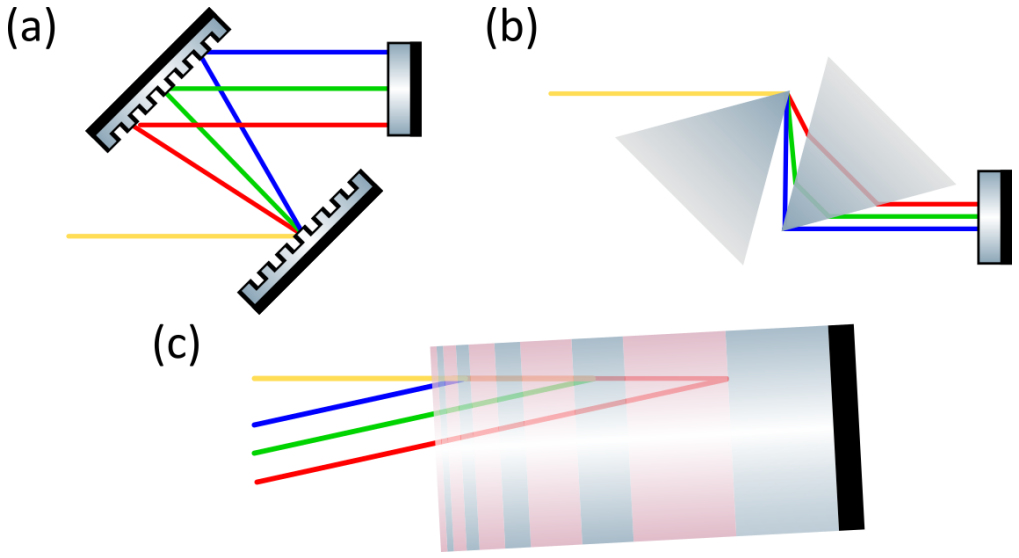

Figure 2.5 Schematic of 3 pulse compression methods : (a) grating pair, (b) prism pair, and (c) chirped mirrors.

In chirped mirrors compressors (c), the pulse is reflected off of a Bragg mirror where the thickness of the dielectric layers (and therefore the Bragg wavelength) varies within the structure. Conceptually, one can imagine that some frequency components will reflect off the outer layer of the mirror while others travel deeper into the mirror before being reflected

and therefore acquire a larger group delay from the reflection. The frequency-dependent group delay curve of a single mirror often contains oscillations, which can be mitigated by more intricate designs [121] and by the combined use of a matched pair of chirped mirrors with opposite oscillations. Modern off-the-shelf chirped mirror pairs can be bought with nearly-constant GDD or third-order dispersion over nearly-octave spanning bandwidths with 0.1 % loss per reflection, and custom designs can be ordered to correct for near-arbitrary dispersion profiles, making it the most suitable solution for the compression of few-cycle pulses. The biggest drawback of these compressors is the relatively low GDD ($\sim$30 fs^2) they can achieve in one reflection compared to other methods, which is typically addressed by performing multiple reflections on the mirror pair or combining it with a second dispersion control method.

2.2 Quantum Description of Light

The first signs of the quantum nature of light appeared at the start of the 20th century, as Plank and Einstein respectively showed that the spectrum of blackbody radiation [10, 11], and the photoelectric effect [12] could both be explained by admitting the existence of light quanta with an energy proportional to the optical frequency. Since then, the field of quantum optics has been in a constant evolution which greatly accelerated in the 1960s, experimentally by the invention of the laser [1], and theoretically by the first prediction of a purely nonclassical effect : photon anti-bunching [122]. Today, quantum light drives some of the most impressive technological and scientific achievements, such as quantum key distributions [123] and gravitational wave detectors [28].

The main theoretical concept of quantum optics necessary to understand the results presented in Chapters 4 and 5 are introduced here in a mostly-informal treatment. First, consider a classical electromagnetic wave in frequency domain

$$\tilde{E}(\omega) = \frac{1}{2}\left(A(\omega-\omega_0)e^{i\phi(\omega-\omega_0)} + \text{c.c.}\right) \tag{2.30}$$

where $\omega = 2\pi\nu$ is the angular frequency corresponding to an optical frequency ν, $A(\omega-\omega_0)$ is the amplitude spectrum of the field centered around the angular frequency ω_0, $\phi(\omega-\omega_0)$ is its spectral phase and c.c. denotes the complex conjugate. To describe the same field in quantum optics, two quantization steps must be taken. The first usually consists in decomposing the field into a (potentially infinite) series of orthonormal modes, and assuming there exist some complex amplitudes a_l such that the probability $|a_l|^2$ of detecting a photon in mode l is proportional to the classical intensity in that same mode. The most commonly used

decomposition is that of monochromatic modes [124], but alternatively broadband "temporal" modes [125] or even infinitely temporally-localized modes [126] can prove more convenient to use depending on the source and the measurement apparatus one tries to describe.

From there, the second quantization promotes the complex amplitude a_l to a so-called annihilation operator $\hat{a}_l$ and its complex conjugate a_l^* to a creation operator $\hat{a}_l^\dagger$. We then also define the Fock basis of states $|n\rangle_l$ that have a fixed number of photons n in mode l, such that

$$\hat{a}_l |n\rangle_l = \sqrt{n}\,|n-1\rangle_l \tag{2.31a}$$
$$\hat{a}_l^\dagger |n\rangle_l = \sqrt{n+1}\,|n+1\rangle_l \tag{2.31b}$$

showing that $\hat{a}_l$ and $\hat{a}_l^\dagger$ respectively describe the process of removing or adding a photon in the mode l. These operators also follow the canonical commutation relation

$$[\hat{a}_l, \hat{a}_m^\dagger] \equiv \hat{a}_l \hat{a}_m^\dagger - \hat{a}_m^\dagger \hat{a}_l = \delta_{lm} \tag{2.32}$$

where δ is the Kronecker delta function. While $\hat{a}_l$ and $\hat{a}_l^\dagger$ are non-Hermitian ($\hat{a}_l \neq \hat{a}_l^\dagger$) and therefore cannot be associated to any observable, they can be combined to create new operators which are Hermitian. Most relevant for the present thesis are the so-called in-phase field quadrature $\hat{x}_l$, its conjugate out-of-phase quadrature $\hat{p}_l$, and the number of photons $\hat{n}_l$

$$\hat{x}_l = \frac{1}{2}\left(\hat{a}_l + \hat{a}_l^\dagger\right) \tag{2.33a}$$
$$\hat{p}_l = \frac{1}{2j}\left(\hat{a}_l - \hat{a}_l^\dagger\right) \tag{2.33b}$$
$$\hat{n}_l = \hat{a}_l^\dagger \hat{a}_l \tag{2.33c}$$

with the notable absence of an operator corresponding to the phase of the field. Multiple attempts to define a phase operator can be found in the literature [127–131], but each of them come with their own mathematical and conceptual difficulties. Due to the unique challenges related to this observable and its major importance in the interpretation of some the results in chapter 5, it is discussed separately in section 2.5. In the following sections, the mode index l is dropped whenever a single mode state is considered to lighten the notation.

2.2.1 Vacuum State and the Heisenberg Uncertainty Principle

"Vacuum" is the term commonly used to describe the ground state of an electromagnetic field mode. It is denoted as $|0\rangle$, and can be defined as the state from which no photons can be extracted

$$\hat{a}\,|0\rangle = 0\ . \tag{2.34}$$

While it arguably the "simplest" state of the electromagnetic field, the vacuum marks one of the biggest departure between the classical and quantum theory of light. Classically, a mode without photons would have a perfectly null field amplitude. In quantum optics, one instead finds that for the vacuum state, this is true only on average

$$\langle x\rangle = \langle p\rangle = 0 \tag{2.35a}$$

$$\Delta x = \Delta p = \frac{1}{2} \tag{2.35b}$$

where $\langle z\rangle$ denotes the expectation value of observable $\hat{z}$, and $\Delta z = \sqrt{\langle z^2\rangle - \langle z\rangle^2}$ its standard deviation from repeated measurements. Equation (2.35b) describes the fundamental uncertainty of electromagnetic fields, often called vacuum fluctuations, which are found in quantum electrodynamics theory to be responsible for multiple nonclassical phenomena including the Casimir effect [132], the Lamb shift [133, 134], and the shot noise of light [135]. Those fluctuations are not unique to the vacuum state, and in fact appear in some way for *any* state of light, with a minimal uncertainty dictated by Heisenberg uncertainty principle [136]

$$\Delta x \Delta p \geq \frac{1}{4} \tag{2.36}$$

which applies to the uncertainty product of any pair of canonically conjugate observables, of which the pair $\hat{x}$ and $\hat{p}$ is only one example.

2.2.2 Coherent States and Shot Noise

A coherent state $|\alpha\rangle$ is defined as the eigenstate of the annihilation operator $\hat{a}$ with eigenvalue α, i.e. $\hat{a}\,|\alpha\rangle = \alpha\,|\alpha\rangle$. It is the state used to describe coherent radiation from a laser source with amplitude $|\alpha|$ and phase $\arg(\alpha)$. In the Fock basis, it takes the form

$$|\alpha\rangle = e^{-|\alpha|^2/2} \sum_n^\infty \frac{\alpha^n}{\sqrt{n!}} |n\rangle \tag{2.37}$$

showing that it is a coherent superposition of Fock states with weights that once squared correspond to a Poissonian probability distribution of photons with mean $\langle n\rangle = |\alpha|^2$ and standard deviation $\Delta n = \sqrt{\langle n\rangle}$. The relative uncertainty in the photocounts statistics of a coherent light source

$$\frac{\Delta n}{\langle n\rangle} = \frac{1}{\sqrt{\langle n\rangle}} \tag{2.38}$$

is most commonly called shot noise, and it defines the standard quantum limit of photocounts experiments performed with a light source with mean photon flux $\langle n\rangle$, i.e. the best relative precision achievable without using a nonclassical light state.

2.2.3 Thermal States and Photon Bunching

As its name suggest, a thermal state describes most notably (but not exclusively) the quantum light state of thermal radiation. It is a mixed state of light, contrary to the previous examples which were all pure states. It is therefore described by a density matrix

$$\hat{\rho}_{\text{thermal}}\left(\langle n\rangle\right) = \sum_{n=0}^\infty \frac{\langle n\rangle^n}{(1+\langle n\rangle)^{n+1}} |n\rangle \langle n| \tag{2.39}$$

where the only parameter is the average number of photons $\langle n\rangle$. Its photon statistics instead follow a Bose-Einstein distribution, resulting in a standard deviation $\Delta n = \sqrt{\langle n\rangle + \langle n\rangle^2}$ that is strictly greater than the Poissonian light of coherent states. These additional fluctuations are sometimes called photon bunching, as they correspond to a correlation in the arrival time of separate photons [137].

2.2.4 Single-Mode Squeezed Vacuum and Squeezing

Quite generally, in quantum optics the term *squeezed* is used to describe a quantum state of light for which the uncertainty in the measurement of a specific observable is made to be smaller than the standard quantum limit set by a coherent state. In accordance with Heisenberg's uncertainty principle, squeezing of some observable requires anti-squeezing of its conjugate. An extreme example of this are the Fock states, which exhibit infinite determinism of their photon number, and a completely undetermined phase.

For the specific case of squeezed vacuum, the two observables are the squeezed quadrature $\hat{q}(\phi) = \hat{x}\cos(\phi) + \hat{p}\sin(\phi)$ and its (anti-squeezed) conjugate $\hat{q}(\phi+\pi/2) = -\hat{x}\sin(\phi) + \hat{p}\cos(\phi)$. Contrary to what its name might suggest, a squeezed vacuum does contain photons. It is actually a superposition of even-number Fock states

$$|S_{\mathrm{SM}}\rangle\,(r,\phi) = \frac{1}{\sqrt{\cosh(r)}} \sum_{n=0}^{\infty} \left(-e^{i\phi}\tanh(r)\right)^n \frac{\sqrt{(2n)!}}{2^n n!}\,|2n\rangle \tag{2.40}$$

with an average number of photons $\langle n\rangle = \sinh^2(r)$, where r is the squeezing parameter and ϕ the squeezing angle, such that the $\Delta\hat{q}(\phi/2)$ is reduced by a factor e^{-r} while $\Delta\hat{q}(\phi/2+\pi/2)$ increases by a factor e^{r}. The reason for the "vacuum" naming is rather that the average field remains null at all times ($\langle x\rangle = \langle p\rangle = 0$) despite there being photons.

Experimentally, squeezed vacuum is obtained from any spontaneous (non-seeded) parametric process which generates photons in pairs, most often parametric down-conversion and four-wave mixing [23]. The most notable experimental use of squeezed vacuum is arguably in modern gravitational wave detectors [8, 28, 135], where a source of squeezed vacuum is combined with a high power coherent laser source to produce a phase-squeezed coherent state and reduce the noise of a gigantic interferometer. To date, the highest levels of squeezing ever reported is 15 dB for continuous wave light [138]. For pulsed light, the technical challenges involved in generating a local oscillator (LO) that is temporally mode-matched to the squeezed light have prevented the observation of such high levels of squeezing, and the current record of 5.88 dB has been achieved with few-ps pulses [139].

2.2.5 Two-mode Squeezed Vacuum

The preceding discussion assumed that the two photons in each photon pair constituting the squeezed vacuum were indistinguishable and were therefore contained in the same mode. However, one still obtains squeezed vacuum if the pairs are composed of distinguishable photon, i.e. if the photons are in separate modes. In that case, one instead obtains an entangled state of light composed of a superposition of two-mode Fock states

$$|S_{\mathrm{TM}}\rangle\,(r,\phi) = \frac{1}{\cosh(r)} \sum_{n=0}^{\infty} \left(-e^{i\phi}\tanh(r)\right)^n |n,n\rangle \tag{2.41}$$

where $|n,n\rangle = |n\rangle_1 \otimes |n\rangle_2$ describes a n-photons Fock state in modes 1 and 2. Contrary to the single-mode squeezed vacuum, there is not only one, but *multiple* two-mode observables that are squeezed, e.g. the in-phase quadrature difference $\hat{q}_1(\phi) - \hat{q}_2(\phi)$, the out-of-phase

quadrature sum $\hat{q}_1(\phi+\pi/2)+\hat{q}_2(\phi+\pi/2)$, the photon-number difference $\hat{n}_1-\hat{n}_2$, the phase sum $\hat{\phi}_1+\hat{\phi}_2$, and just as many anti-squeezed two-mode observables. If one considers only one mode of the squeezed vacuum by taking a partial trace over the second mode

$$\hat{\rho}_1 = \mathrm{Tr}_2\left(|S_{\mathrm{TM}}\rangle\langle S_{\mathrm{TM}}|\right) = \frac{1}{\cosh^2(r)}\sum_{n=0}^{\infty}\tanh^{2n}(r)\,|n\rangle\langle n| \tag{2.42}$$

the result is a thermal state with an average number of photons $\langle n\rangle = \sinh^2(r)$. The very rich entanglement properties of two-mode squeezed states make them a workhorse of experimental quantum optics [23], as they can be used as a starting point in post-selection schemes to produce a multitude of other quantum light states, including notably heralded single photons [14, 17], sub-poissonian light [19, 21], and band-conditioned states [32].

2.3 Parametric Down-Conversion

Parametric down-conversion (PDC) is a second-order nonlinear optical process, where photons from a (usually) strong optical pump of angular frequency ω_p and wavevector $\vec{k}_p$ are annihilated to create pairs of photons at a lower optical frequency via DFG. When the two photons from each pair that are generated are distinguishable (either by their polarization, frequency, or wavevector), they are traditionally labeled respectively as signal (with angular frequency ω_s and wavevector $\vec{k}_s$) and idler (with angular frequency ω_i and wavevector $\vec{k}_i$). As any parametric nonlinear process, it follows the laws of conversion of energy and momentum

$$\hbar\omega_p = \hbar(\omega_s+\omega_i) \tag{2.43a}$$
$$\hbar\vec{k}_p = \hbar(\vec{k}_s+\vec{k}_i) \tag{2.43b}$$

as presented in details in section 2.1.2. When either of the two down-converted mode is seeded (stimulated), this process of the basis behind classical optical parametric amplification. In the unseeded (spontaneous) case, PDC instead creates a squeezed vacuum state, which is here assumed to be in two modes (signal and idler). When considering only a single, well-defined narrowband mode $\hat{a}_{\mathrm{p}}$, $\hat{a}_{\mathrm{s}}$, and $\hat{a}_{\mathrm{i}}$ for each of the pump, signal and idler beams, and in the case of perfect phase matching $|\Delta\vec{k}| = |\vec{k}_s+\vec{k}_i-\vec{k}_p| = 0$, their interaction can be described by the set of coupled equations [140]

$$\frac{\mathrm{d}\hat{a}_\mathrm{s}}{\mathrm{d}z} = -ig\hat{a}_\mathrm{i}^\dagger\hat{a}_\mathrm{p} \tag{2.44a}$$
$$\frac{\mathrm{d}\hat{a}_\mathrm{i}}{\mathrm{d}z} = -ig\hat{a}_\mathrm{s}^\dagger\hat{a}_\mathrm{p} \tag{2.44b}$$
$$\frac{\mathrm{d}\hat{a}_\mathrm{p}}{\mathrm{d}z} = -ig\hat{a}_\mathrm{s}\hat{a}_\mathrm{i} \tag{2.44c}$$

where g is a constant describing the strength of the nonlinear coupling between all three modes, and z is the spatial coordinate along the propagation axis. There are no known general closed-form solution to this set of equations. It can be solved numerically when the pump has a sufficiently low enough number of photons, and a wide range of approximate solutions exist for various specific cases [23,54,141,142]. The most prominent strategy consist in treating the pump classically ($\hat{a}_\mathrm{p} \approx A_\mathrm{p}$) and assume that it is a static field ($A_\mathrm{p}(z) \approx A_\mathrm{p}(0)$). In this case, the set of equations (2.44) can be solved by taking a second derivative, yielding a pair of decoupled second order differential equations whose solution follow a Bogolyubov transformation [143]

$$\hat{a}_\mathrm{s}(L) = \hat{a}_\mathrm{s}(0)\cosh(G) + \hat{a}_\mathrm{i}^\dagger(0)\sinh(G) \tag{2.45a}$$
$$\hat{a}_\mathrm{i}(L) = \hat{a}_\mathrm{i}(0)\cosh(G) + \hat{a}_\mathrm{s}^\dagger(0)\sinh(G) \tag{2.45b}$$

where $G = gA_\mathrm{p}L$ is the parametric gain, and L is the interaction length of the PDC process (usually the thickness of the nonlinear medium). The output state is indeed a two-mode squeezed vacuum state as introduced in section 2.2.5 with squeezing parameter $r = G$.

2.3.1 Microscopic Regime: Photon Pairs

In the spontaneous regime $G \ll 1$ of PDC, also called the low-gain regime, a single signal-idler photon pair is produced with a probability

$$P(n=1) = \frac{\tanh^2(G)}{\cosh^2(G)} \approx G^2 \tag{2.46}$$

which allows for the generation of so-called heralded single photons [17,18], where the detection of an idler photon heralds the presence of another, *single* photon in the signal branch. The implementation of low-gain spontaneous parametric down-conversion (SPDC) sources

is the most prominent strategy to experimentally achieve single photon states $|1\rangle$, and they have been used in major experimental demonstration of quantum physics, including the Hong-Ou-Mandel effect [144] and the violation of Bell inequalities [14].

For these sources, increasing the parametric gain G yields a higher rate of photon pair production as predicted by equation (2.46) and therefore faster acquisition of data, but it also comes with a higher risk of production of multiple pairs of photons

$$P(n>1) = 1 - P(n=0) - P(n=1) = 1 - \frac{1+\tanh^2(G)}{\cosh^2(G)} \approx G^4 \tag{2.47}$$

and therefore, in the absence of affordable photon-number-resolving detectors, most heralded single photon sources operate with a very low parametric gain to ensure that a vast majority of experimental data points are generated from a single pair of photons.

2.3.2 Macroscopic Regime: Bright Twin Beams

Most texts distinguish the spontaneous, microscopic regime of PDC from a so-called high-gain regime where $G > 1$. Past this point, a two-mode PDC source produces (many) photon pairs more often than not, and only the number of downconverted photons changes from shot to shot, turning it into a light source that is often called twin beams [23]. This definition however includes a mesoscopic regime [39], from $G = 1$ up to $G \sim 3$, where the signal and idler beams contain < 100 photons on average and where quantization effects can still be observed with relative ease.

Conversely, recent advances of ultrafast laser technology enabled the demonstration of *macroscopic* PDC implementations where the parametric gain reaches records values of $G = 16$, corresponding to over 10^{13} photons per pulse on average [22]. These developments enabled experimental exploration of nonlinear optical phenomena driven by squeezed vacuum, including high-harmonic generation [40] and photoionization [37]. The rest of this thesis focuses on such sources, with over 10^6 photons per pulse on average, and interchangeably refers to this regime as high-gain or as macroscopic. The resulting state is labeled as bright twin beams (BTBs) to highlight its considerably high photon content making it visible to the naked eye, and its single-mode equivalent is labeled as bright squeezed vacuum (BSV).

2.3.3 Multimode Bright Twin Beams and the Schmidt Decomposition

The discussion so far assumed that the pump was nonlinearly coupled to a single pair of signal and idler modes. This assumption is reasonable for an optical parametric amplifier (OPA),

where a finite seed defines the signal mode, while energy and momentum conservation laws dictate the corresponding idler mode. In the spontaneous case however, more often than not a large number of vacuum mode pairs are coupled to the pump.

The information about the mode composition of twin beams is contained in the joint spectral amplitude (JSA) [143], which in the low-gain (microscopic) regime takes the form

$$\mathrm{JSA}(\mathbf{k}_\mathrm{s}, \mathbf{k}_\mathrm{i}, \omega_\mathrm{s}, \omega_\mathrm{s}) = \tilde{A}_\mathrm{p}(\mathbf{k}_\mathrm{s}, \mathbf{k}_\mathrm{i}, \omega_\mathrm{s}, \omega_\mathrm{i})\mathrm{sinc}\left(\frac{|\Delta\mathbf{k}(\omega_\mathrm{s}, \omega_\mathrm{i})|L}{2}\right)\exp\left(i\frac{|\Delta\mathbf{k}(\omega_\mathrm{s}, \omega_\mathrm{i})|L}{2}\right) \tag{2.48}$$

where $\tilde{A}_\mathrm{p}$ is the complex spectral amplitude of the pump, and $\Delta\mathbf{k} = \mathbf{k}_\mathrm{p} - \mathbf{k}_\mathrm{s} - \mathbf{k}_\mathrm{i}$ is the wave vector mismatch of the PDC process dictated by the chromatic dispersion of the nonlinear medium. In this regime, the JSA can be understood as the probability amplitude of detecting a pair of signal and idler photons with respectively wavevectors $\mathbf{k}_\mathrm{s}$ and $\mathbf{k}_\mathrm{i}$, and angular frequencies ω_s and ω_i.

In general, the full 6-dimensional form of the JSA is too complex for practical use. Most works therefore assume separability of the k and ω degrees of freedom as an approximation, and then use angular filtering to eliminate the k dependence and obtain a 2-dimensional JSA [143]. In this form, a Schmidt decomposition can be performed on the JSA

$$\mathrm{JSA}(\omega_\mathrm{s}, \omega_\mathrm{s}) = \sum_{l=0}^{\infty}\sqrt{\Lambda_l}\psi_l(\omega_\mathrm{s})\phi_l(\omega_\mathrm{i}) \tag{2.49}$$

to obtain the relative occupation (Schmidt coefficients Λ_l) and the shapes ($\psi_l(\omega_\mathrm{s})$ and $\phi_l(\omega_\mathrm{i})$) of the signal and idler frequency modes. From this decomposition, the Schmidt number

$$K = \frac{1}{\sum_{l=0}^{\infty}\Lambda_l^2} \tag{2.50}$$

further yields the effective number of spectral modes for *each* of the BTBs, e.g. $K = 3$ indicates that there are 3 occupied signal modes and 3 occupied idler modes.

2.4 Characterization of Quantum Light

This section introduces various standard characterization methods of quantum light states and their application to BTBs. For the sake of simplicity, the following examples assume free space, unidimensional and unidirectional propagation.

2.4.1 Second-Order Auto-Correlation and Photon Statistics

The classical second-order auto-correlation function

$$g^{(2)}(\tau) = \frac{\langle I(t)I(t+\tau)\rangle}{\langle I(t)\rangle \langle I(t+\tau)\rangle} \tag{2.51}$$

describes the correlation between the optical intensity I of two parts of an electromagnetic field that are temporally separated by a time delay τ. It is particular importance in ultrafast photonics, where its measurements yields an upper bound for the duration of optical pulses (as discussed in section 2.1.3). Its zero-delay value

$$g^{(2)} \equiv g^{(2)}(0) = \frac{\langle I(t)^2\rangle}{\langle I(t)\rangle^2} = 1 + \frac{\Delta^2 (I(t))}{\langle I(t)\rangle^2} \tag{2.52}$$

is also classically used as a metric of how "chaotic" a light source is [56]. In quantum optics, $g^{(2)}(\tau)$ describes how the fact of measuring one photon affects the probability of measuring a second photon at time delay τ. If we consider instantaneous detectors registering the instantaneous photon flux $n(t)$, we can define infinitely temporally-localized modes with ladder operators $\hat{a}(t)$ and $\hat{a}^\dagger(t)$ [126] to find a quantum description

$$g^{(2)}(\tau) = \frac{\left\langle \int_t a^\dagger(t)a^\dagger(t+\tau)a(t+\tau)a(t)\mathrm{d}t \right\rangle}{\langle \int_t a^\dagger(t)a(t)\mathrm{d}t\rangle \langle \int_t a^\dagger(t+\tau)a(t+\tau)\mathrm{d}t\rangle} = \frac{\langle \int_t n(t+\tau)n(t)\mathrm{d}t\rangle - \delta(\tau)\langle n\rangle}{\langle n\rangle^2} \tag{2.53}$$

where the commutation relation $a(t)a^\dagger(t+\tau) = \delta(\tau)$ is used for the last equality. At zero-delay and in the limit of high photon flux $\langle n\rangle \gg 1$, we recover the classical result

$$g^{(2)} \approx 1 + \frac{\Delta^2 n}{\langle n\rangle^2}$$

quantifying the statistical fluctuations of the photon flux. More generally, we find that $g^{(2)}$ describes the change in the expected number of photons when one performs a photon-subtraction post-selection

$$g^{(2)} = \frac{\langle n(n-1)\rangle}{\langle n\rangle^2} \tag{2.54}$$

as sketched in Fig 2.6. For a so-called bunched light source ($g^{(2)} > 1$), the measurement of a single photon on the conditioning detector is correlated with the probability of measuring

more photons than average on the second detector. For a "coherent" source (meant here broadly as a source for which $g^{(2)} = 1$, and not necessarily a coherent state), the measurement of a single photon on the conditioning detector yields no information on the number of photons arriving on the second detector. Finally, for an anti-bunched source ($g^{(2)} < 1$), the measurement of a single photon on the conditioning detector is anti-correlated with the probability of measuring more photons than average on the second detector. A famous non-classical result is that of the single photon state $|1\rangle$, where $g^{(2)} = 0$ because the photon can reach only one detector [14].

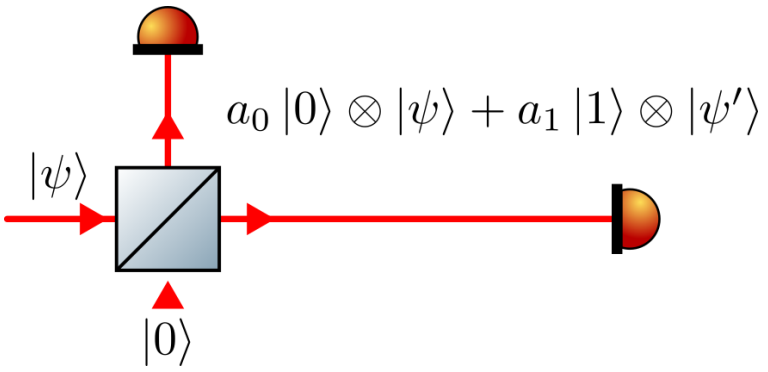

Figure 2.6 Setup for photon subtraction post-selection and $g^{(2)}$ measurement. The beam-splitter has a very low reflectivity such that at most a single photon is reflected toward the upper detector. If no photon is reflected, the transmitted state is the same as the input $|\psi\rangle$, with an average photon number $\langle n\rangle = \langle\psi|\,\hat{n}\,|\psi\rangle$. If a photon is reflected, the transmitted state is instead $|\psi'\rangle \propto \hat{a}\,|\psi\rangle$ with an average photon number $\langle\psi'|\,\hat{n}\,|\psi'\rangle = g^{(2)}\,\langle n\rangle$.

The photon number probability distribution and the corresponding value of $g^{(2)}$ for common quantum states of light are listed in table 2.1. Due to the simplicity of its measurement and its well-known values, $g^{(2)}$ is sometimes used as a metric to uniquely identify the photon statistics of a source. Yet, states that have otherwise very dissimilar photon statistics can share nearly-identical values of $g^{(2)}$, such as a coherent state and a macroscopic Fock state. So, while $g^{(2)}$ does yields insightful and experimentally-relevant information about a given state, one should always keep in mind its limitations and consider also looking at the full photon statistics of the source.

In the last decade, there has been a pronounced interest toward the use of BTBs and BSV as the driving field for multiphoton effects due to their high value of $g^{(2)}$ (and higher-order correlation functions $g^{(l)}$ with $l = 3, 4, 5, ...$) leading to a so-called statistical enhancement of the conversion efficiency [25, 26, 40]. This effect can be understood classically by considering a process with an efficiency that scales with the intensity I

Table 2.1 Photon statistics of common quantum states of light

State	Photon number probability distribution $P(n)$	$g^{(2)}$
Vacuum $\lvert 0\rangle$	$\delta_{n,0}$	0
m-photon Fock $\lvert m\rangle$	$\delta_{n,m}$	$\frac{m-1}{m}$
Coherent $\lvert\alpha\rangle$	$e^{-\lvert\alpha\rvert^2}\frac{\lvert\alpha\rvert^{2n}}{n!}$	1
Thermal $\rho_{\mathrm{th}}(\langle n\rangle)$	$\frac{\langle n\rangle^n}{(1+\langle n\rangle)^{n+1}}$	2
Squeezed vacuum $\lvert S_{\mathrm{SM}}(\langle n\rangle)\rangle$	$(n+1)\mathrm{mod}2\ \frac{n!}{2^n(\frac{n}{2}!)^2}\frac{\langle n\rangle^{n/2}}{(1+\langle n\rangle)^{(n+1)/2}}$	$3+\frac{1}{\langle n\rangle}$

$$\eta(I) \propto I^{\alpha}$$

with $\alpha \geq 1$. If this process is driven by a light source with a probability density distribution of intensity $P(I)$, the resulting average efficiency is therefore

$$\langle \eta \rangle \propto \frac{\int_0^\infty \eta(I) I P(I)\,\mathrm{d}I}{\int_0^\infty I P(I)\,\mathrm{d}I} \equiv \frac{\langle I^{\alpha+1}\rangle}{\langle I\rangle} = g^{(\alpha+1)}\langle I\rangle^{\alpha}$$

which is exactly $g^{(\alpha+1)}$ greater than a coherent source for which $g^{(2)} = g^{(3)} = g^{(4)} = ... = 1$. A functionally-identical result is obtained with the quantum formulation of auto-correlation functions [143].

2.4.2 Joint Spectral Intensity, Spectral Covariance and Schmidt Modes

Strictly speaking, a measurement of the JSA is generally necessary to obtain the mode composition of a BTBs source, but it is rarely measured due to the experimental challenges involved in simultaneously measuring the amplitude and phase of two broadband fields. Instead, the joint spectral intensity (JSI)

$$\mathrm{JSI}(\omega_{\mathrm{s}}, \omega_{\mathrm{s}}) = |\mathrm{JSA}(\omega_{\mathrm{s}}, \omega_{\mathrm{s}})|^2 = \left|\sum_{l=0}^{\infty} \sqrt{\Lambda_l}\psi_l(\omega_{\mathrm{s}})\phi_l(\omega_{\mathrm{i}})\right|^2 \tag{2.55}$$

is measured more often due to its intensity-only measurement being much simpler to implement, at the price of losing phase information. This is typically performed from a measurement of the spectral covariance [63]

$$\mathrm{COV}\left(n_{\mathrm{s}}(\omega_{\mathrm{s}}), n_{\mathrm{i}}(\omega_{\mathrm{i}})\right) = \left|\sum_{l=0}^{\infty} u_l v_l \psi_l(\omega_{\mathrm{s}}) \phi_l(\omega_{\mathrm{i}})\right|^2 \tag{2.56}$$

which is exactly equal to the JSI in the low gain limit. In the high-gain limit where $u_l \approx v_l \approx \sqrt{\Lambda_l}$ [143], the spectral covariance contains the same information as the JSI, but with redistributed coefficients. Therefore, if the phase of the underlying JSA is flat, i.e. if

$$\mathrm{JSA}(\omega_{\mathrm{s}}, \omega_{\mathrm{s}}) = |\mathrm{JSA}(\omega_{\mathrm{s}}, \omega_{\mathrm{s}})|\, e^{i\phi}$$

for any constant phase ϕ, then a Schmidt decomposition of $\sqrt{\mathrm{COV}\left(n_{\mathrm{s}}(\omega_{\mathrm{s}}), n_{\mathrm{i}}(\omega_{\mathrm{i}})\right)}$ yields the correct Schmidt modes and coefficients, up to detection efficiency [63]. The flat-phase assumption can be verified aposteriori by comparing the resulting Schmidt number to the one calculated from the zero-delay second-order auto-correlation function $g^{(2)}$ [145]

$$K = \frac{g_1^{(2)} - 1}{g^{(2)} - 1} \tag{2.57}$$

where $g_1^{(2)}$ is the single-mode value of $g^{(2)}$, e.g. 2 for BTBs. The JSI (and the spectral covariance) can also offer a visual indication of the number of modes. Indeed, by definition a single-mode source must have a JSI of the form

$$\mathrm{JSI}_1(\omega_{\mathrm{s}}, \omega_{\mathrm{s}}) = \left|\psi_0(\omega_{\mathrm{s}}) \phi_0(\omega_{\mathrm{i}})\right|^2 \tag{2.58}$$

which is a separable function of ω_{s} and ω_{i}. Therefore, the presence of any frequency correlations in the JSI can be interpreted as a sign of a source being multimode. Examples of the typical shapes of multimode and single-mode JSIs are presented in Figure 2.7.

The separability condition on the JSI for a single-mode source dictates that the pump amplitude bandwidth must match the phase-matching bandwidth (in the low-gain regime) [61–64]. Equivalently, in time domain this means that the duration of the pump envelope in time must match the correlation time of the phase-matched vacuum modes [145].

2.4.3 Q Function and Joint Measurement of Non-Commuting Quadratures

The Q function, first introduced by Husimi in 1940 [146], is a quasiprobability distribution used to represent a quantum state in phase space. It provides a visual representation of the density matrix $\hat{\rho}$ of a quantum state by projecting it against every coherent states $|\alpha\rangle$

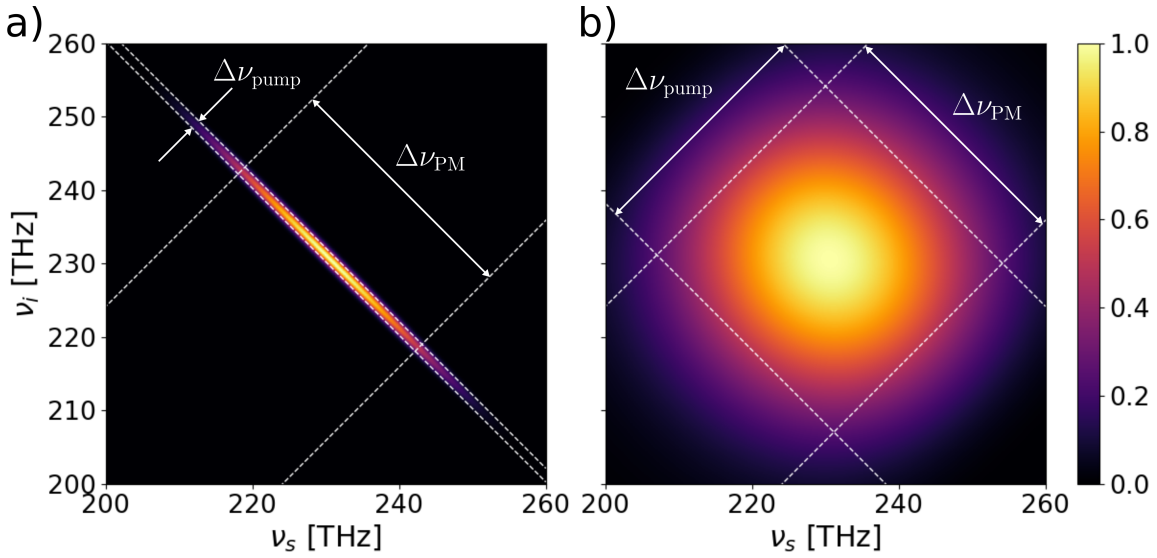

Figure 2.7 JSI of a) an heavily-multimode BSV, and b) a single-mode BSV.

$$Q(\alpha) = \frac{1}{\pi} \langle \alpha | \, \hat{\rho} \, | \alpha \rangle \tag{2.59}$$

and contrary to other popular representations such as the Wigner distribution [147] or the Glauber–Sudarshan P representation [148, 149], it has the peculiarity of being non-negative. Experimentally, the Q function can be directly sampled from the simultaneous measurements of canonically conjugate variables, via e.g. 8-ports homodyne detection or heterodyning [150–153], and can be understood as the probability density distribution of the result of such measurements. This feature makes it closely linked to the infamous measurement of the quantum phase, which is obtained by the same schemes [154–157]. It is also mathematically equivalent to the Wigner quasiprobability distribution $W(\alpha)$ convolved with a Gaussian window, but experimentally the two distributions do not perform identically for all states when they are reconstructed from finite and potentially noisy data [158, 159].

2.4.4 Nonclassicality Criteria and the Noise Reduction Factor

A major aspect of quantum optics is to distinguish between states of light that are compatible with classical electrodynamics, and those that are not and are thus called nonclassical. Many *sufficient* nonclassicality criteria can be found in the literature, e.g. negativity of phase space distributions [160], quadrature fluctuations below the vacuum level (i.e. squeezing) [23, 95], sub-shot-noise photon-number fluctuations [14, 19, 21, 144], violation of the Cauchy-Schwarz [161] or other inequalities [65]. Conversely, only a few *necessary* nonclassicality criteria have

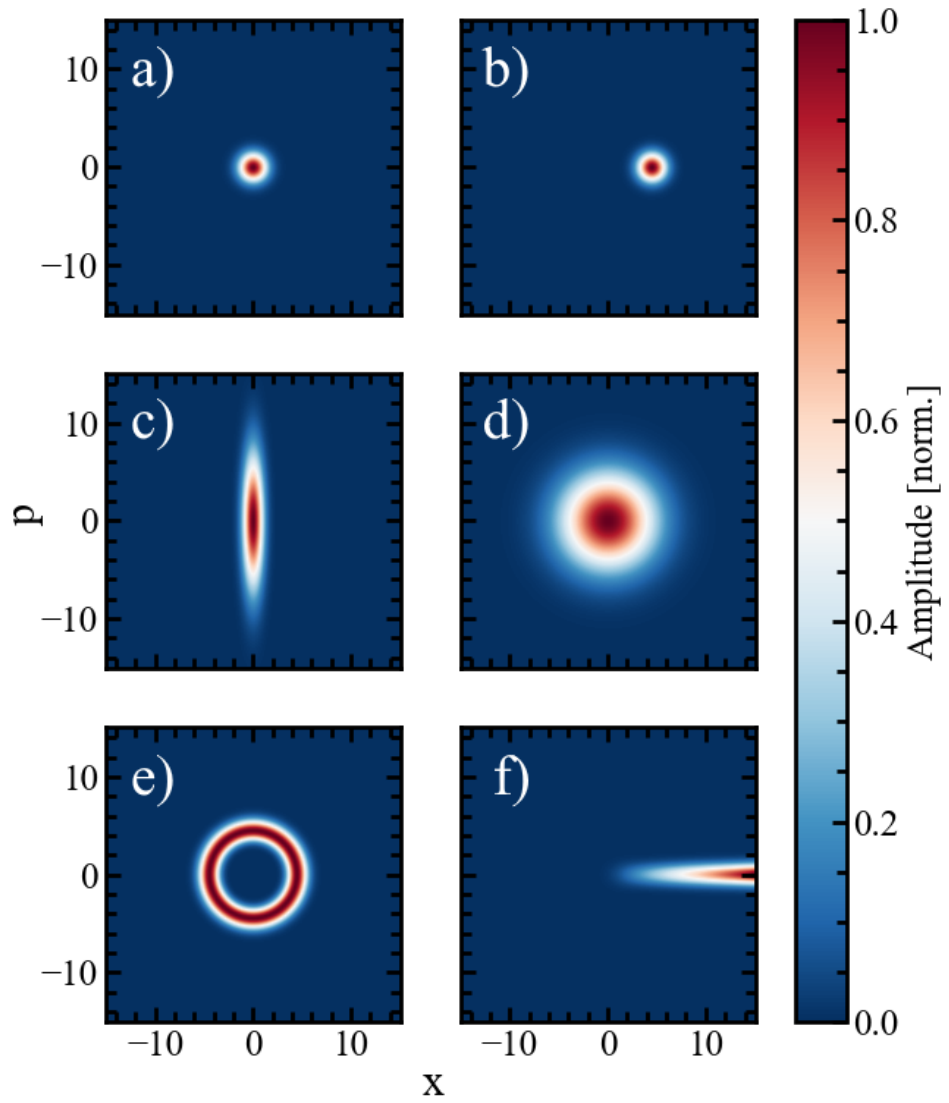

Figure 2.8 Q function of 6 states of light : a) vacuum, b) coherent, c) squeezed-vacuum, d) thermal, e) Fock, and f) an eigenstate of the Pegg-Barnett phase operator with $s = 300$ (see section 2.5 for details). States shown in plots b)-e) all have an average photon number $\langle n \rangle = 10$.

been demonstrated so far [162, 163] and require specific measurement apparatuses.

For this reason, it is important for experimental demonstrations of nonclassicality to identify the easiest criterion that can be demonstrated for the particular state considered. In the case of macroscopic BTBs, most criteria listed above trivially tend toward their classical limit due to a $1/\langle n \rangle$ dependence in their mathematical formulation. Instead, the nonclassicality of BTBs is most often demonstrated via a measurement of the noise reduction factor (NRF) [23, 65]

$$\mathrm{NRF} = \frac{\Delta^2 \left(m_\mathrm{s} - m_\mathrm{i}\right)}{\left\langle m_\mathrm{s} + m_\mathrm{i} \right\rangle} \tag{2.60}$$

which evaluates the (squared) ratio of the noise between any two light sources to the noise expected for two coherent light sources with the same average photon numbers. Here, m denotes the *measured* number of photons, and its operator is derived from the *emitted* number of photons n by modeling losses in the system as transmission through a beamsplitter right before detection [164]. The NRF is defined such that the standard quantum limit corresponds to NRF $= 1$, and any smaller value demonstrates a quantum advantage. Under perfect conditions, the signal and idler twin beams generated from PDC would reach NRF $= 0$, i.e. $\Delta^2 \left(m_s - m_i\right) = 0$, but any losses, sources of noise, or mismatch in the detection efficiency will increase it to a finite value. The first two issues are fundamental and limit the degree of squeezing that can be leveraged from the BTBs. The latter is however purely technical, and can be remedied either experimentally by introducing controllable losses on both detection channels, or numerically by using an alternate definition of the NRF [21]

$$\mathrm{NRF} = \frac{\Delta^2 \left(m_\mathrm{s} - \beta\left(m_\mathrm{s}\right) m_\mathrm{i}\right)}{\left\langle m_\mathrm{s} + \beta\left(m_\mathrm{s}\right) m_\mathrm{i} \right\rangle} \tag{2.61}$$

where $\beta\left(m_\mathrm{s}\right)$ is an experimentally-determined correlation function such that the NRF is minimized. Its simplest form $\beta = \left\langle m_\mathrm{s} \right\rangle / \left\langle m_\mathrm{i} \right\rangle$ is obtained with noiseless, perfectly-linear detectors and a single-mode source. Both definitions are used and compared for the results presented in Chapters 4 and 5, but more focus is given to the second definition (2.61) as it usually yields lower values due to its lesser sensitivity to imperfect experimental conditions. Typical values of the NRF ranging from 0.2 to 0.5 have been reported in the literature for multimode BTBs with 10^5–10^6 photons per pulse on average [21, 68, 73–75].

2.5 The Quantum Phase Problem

The search for a quantum theory of the phase of an electromagnetic field has been a long-standing open problem in physics, which started with the seminal work of Dirac in 1927 [127]. The search for a solution find importance in the determination of the physical limitations to e.g. the precision of interferometric measurements [135, 165], the stabilization of the CEP of few-cycle pulse trains [45, 48], and the noise propagation in phase-sensitive nonlinear phenomena such as HHG [47, 49].

Conceptually, the fundamental limit of optical phase precision can be understood from the (approximate) Heisenberg uncertainty relation

$$\Delta n \Delta \phi \geq \frac{1}{2} \tag{2.62}$$

which highlights that any hypothetical state of certain phase ($\Delta\phi = 0$) would also show complete indetermination of the photon number ($\Delta n = \infty$), i.e. either infinite energy or infinite measurement time. Nowadays, two limits are generally recognized. The first is the phase analogue to the shot-noise limit [135]

$$\Delta \phi \gtrsim \frac{1}{2\sqrt{\langle n \rangle}} \tag{2.63}$$

which is achieved for bright coherent states, and can be understood as the standard quantum limit of phase measurements. The second is known as the Heisenberg limit

$$\Delta \phi \gtrsim \frac{1}{\langle n \rangle} \tag{2.64}$$

which can be reached with e.g. suitable squeezed states [135] or SU(1,1) interferometers [166], and is generally understood as the maximal precision of phase measurements [165, 167, 168]. The so-called "quantum phase problem" [169–171] stems from the fact that defining any operator $\hat{\phi}$ following the canonical commutation relation

$$\left[\hat{n}, \hat{\phi}\right] = i$$

as Dirac attempted will always inadvertently lead to contradictory predictions due to eigenvalues of $\hat{n}$ being lower-bounded to 0 [169]. Following attempts in the 1960s explored new operators defined instead as the sine, cosine and exponential of the phase [128,172], which had other mathematical difficulties such as non-unitarity, and further implied the non-existence of an actual Hermitian "phase" operator. No single, universally-accepted solution to the quantum phase problem exists even today, but multiple formalisms have demonstrated good agreement both with experiments and with theoretical expectations stemming from the correspondence principle and the Heisenberg uncertainty principle.

Here, two of these "modern" solutions are briefly reviewed. The first is the Pegg-Barnett formalism [130,131], which is the latest and arguably the most recognized "operator approach" to the quantum phase problem. It first introduces a truncated Hilbert space of Fock states with a maximal number of photons $n_{\max} = s$, where a phase operator

$$\hat{\Phi}_s = \sum_{m=0}^{s} \phi_m \left|\phi_m\right\rangle \left\langle\phi_m\right| \tag{2.65}$$

with eigenstates

$$\left|\phi_m\right\rangle = (s+1)^{-1/2} \sum_{n=0}^{s} \exp(in\phi_m) \left|n\right\rangle \tag{2.66}$$

can be defined without the usual mathematical difficulties, and then the limit $s \to \infty$ is applied as a last step to compute physical quantities. This approach converges to the results of previous attempts for very bright states, but now also correctly predicts a uniform distribution over 2π for the phase of the vacuum.

The second solution is the so-called "phase-space approach", where a quasiprobability distribution of a state under study is first acquired by the standard means, and then the probability distribution of a phase measurement can be calculated from it [169]. For instance, starting from the Q-function $Q_{\hat{\rho}}$ of a quantum state with density matrix $\hat{\rho}$, we get the probability distribution [173]

$$P(\phi|\hat{\rho}) = \int_0^\infty \frac{\mathrm{d}r}{\pi} r Q_{\hat{\rho}}(re^{i\phi}) \tag{2.67}$$

from which e.g. the expectation value and variance can be calculated. The biggest strength of this formalism is that it shows that the probability distribution (2.67) is identical to the distribution of the phase difference between the quantum state $\hat{\rho}$ and a strong coherent-state LO as one measures in e.g. a multi-port homodyne interferometer [156, 174, 175], therefore directly connecting theory to experiments. This formalism is also directly connected to a family of phase operators introduced earlier by Paul [129], and it has recently been shown to be linked to the Pegg-Barnett formalism [173].

CHAPTER 3 METHODOLOGY AND DESIGN

This chapter presents the computational methodology used to perform the numerical simulations presented in Chapter 5, and the experimental methodology used to implement and characterize the bright twin beams (BTBs) source presented in Chapter 4.

3.1 Numerical Model of Ultrafast, High-Gain Parametric Down-Conversion

Recent advances in experimental implementations of bright squeezed states of light have seen the generation of bright squeezed vacuum (BSV) and BTBs with unprecedented parametric gain [22,40], resulting in quantum light sources with photon fluxes comparable to off-the-shelf laser systems. In this regime of extreme nonlinear gain, third-order nonlinear effects can play a vital role [176] and must be considered on top of the usual effects of diffraction [24,73,177] and chromatic dispersion [62, 63, 178–180]. The interplay between all 3 effects can create extremely complex pulse propagation phenomena [181] whcih are difficult to track in quantum models of parametric down-conversion (PDC), but are relatively well understood in classical models of ultrafast nonlinear pulse propagation [182].

Recent theoretical studies have highlighted how effective semi-classical models of PDC can be at predicting the statistical properties of squeezed light and even correlations in the observables of entangled BTBs [60, 183]. In theses models, a stochastic field mimicking the properties of the vacuum states of the electromagnetic field is used as a seed in a fully classical model of nonlinear pulse propagation. This strategy avoids all the challenges involved in implementing high-order dispersion and nonlinear effects in a quantum framework, with the main downside being that one needs to run the same simulation multiple times with a different vacuum seed to obtain statistics on the output observables. This however mimics the behavior of real-world quantum experiments, where one needs to repeat the same measurement of an observable on multiple systems prepared in the same quantum states in order to resolve its statistics, enabling a one-to-one comparison of results despite a seemingly inefficient computational methodology.

3.1.1 Unidirectinal Propagation Equation

We start from the standard wave equation of nonlinear optics [57]

$$\nabla^2\mathbf{E} - \frac{1}{c^2}\frac{\partial^2\mathbf{E}}{\partial t^2} = \frac{1}{\epsilon_0 c^2}\frac{\partial^2\mathbf{P}}{\partial t^2} \tag{3.1}$$

where $\mathbf{E} = \mathbf{E}(\mathbf{r}, t)$ is the electric field and $\mathbf{P} = \mathbf{P}^{(1)}(\mathbf{r}, t) + \mathbf{P}^{\mathrm{NL}}(\mathbf{r}, t)$ is the material polarisation (with linear response $\mathbf{P}^{(1)}$ and nonlinear response $\mathbf{P}^{\mathrm{NL}}$) at the spatial coordinate $\mathbf{r}$ and at time t, c is the speed of light, and ϵ_0 is the vacuum permittivity.

We first identify z as the preferred propagation direction for all light fields considered in this model, and take a Fourier transform over all other coordinates

$$\frac{\partial^2 \tilde{\mathbf{E}}}{\partial z^2} - (k_x^2 + k_y^2)\tilde{\mathbf{E}} - \frac{\omega^2}{c^2}\tilde{\mathbf{E}} = -\frac{\omega^2}{\epsilon_0 c^2}\tilde{\mathbf{P}} \ . \tag{3.2}$$

In the frequency domain, the linear polarization is given simply as $\tilde{\mathbf{P}}^{(1)} = \epsilon_0(n^2 - 1)\tilde{\mathbf{E}}$, where n is the linear refractive index of the medium which may depend on k_x, k_y and ω, but is assumed to be independent of z. Equation (3.2) becomes

$$\frac{\partial^2 \tilde{\mathbf{E}}}{\partial z^2} - (k_x^2 + k_y^2)\tilde{\mathbf{E}} + \frac{n^2\omega^2}{c^2}\tilde{\mathbf{E}} = -\frac{\omega^2}{\epsilon_0 c^2}\tilde{\mathbf{P}}^{\mathrm{NL}} \tag{3.3a}$$

$$\frac{\partial^2 \tilde{\mathbf{E}}}{\partial z^2} + k_z^2\tilde{\mathbf{E}} = -\frac{\omega^2}{\epsilon_0 c^2}\tilde{\mathbf{P}}^{\mathrm{NL}} \tag{3.3b}$$

where $k_z^2 = \frac{n^2\omega^2}{c^2} - k_x^2 - k_y^2$ is the squared longitudinal wavevector. In the linear propagation case $\tilde{\mathbf{P}}^{\mathrm{NL}} = 0$, equation (3.3b) is solved exactly by $\tilde{\mathbf{E}}(z) = \tilde{\mathbf{E}}_{\rightarrow}(0)e^{-ik_z z} + \tilde{\mathbf{E}}_{\leftarrow}(0)e^{ik_z z}$ which describes independent linear propagation of forward and backward propagating waves, as seen in section 2.1.1.

To consider only forward propagating components, a standard approach is to first separate the second-order spatial derivative in the left-hand side into two forward and backward propagating operators [182]

$$\left(\frac{\partial}{\partial z} + ik_z\right)\left(\frac{\partial}{\partial z} - ik_z\right)\tilde{\mathbf{E}} = -\frac{\omega^2}{\epsilon_0 c^2}\tilde{\mathbf{P}}^{\mathrm{NL}} \tag{3.4}$$

and then assume that $\tilde{\mathbf{E}}$ is composed mostly of forward-propagating components $\tilde{\mathbf{E}}_{\rightarrow}$, for which the backward propagating operator can be approximated as $\left(\frac{\partial}{\partial z} - ik_z\right) \approx -2ik_z$. Using this approximation, we obtain the unidirectional pulse propagation equation (UPPE) [79]

$$-\left(\frac{\partial}{\partial z}+ik_z\right)2ik_z\tilde{\mathbf{E}}=-\frac{\omega^2}{\epsilon_0 c^2}\tilde{\mathbf{P}}^{\mathrm{NL}}$$
$$\frac{\partial\tilde{\mathbf{E}}}{\partial z}=-ik_z\tilde{\mathbf{E}}-\frac{i\omega^2}{2k_z\epsilon_0 c^2}\tilde{\mathbf{P}}^{\mathrm{NL}} \tag{3.5}$$

3.1.2 Coupled Envelope Equations

We decompose the electric field into two orthogonal polarization modes, corresponding respectively to the ordinary (o) and extraordinary (e) axes of a uniaxial birefringent medium

$$\tilde{\mathbf{E}}=\tilde{E}_{\mathrm{o}}\hat{\mathrm{o}}+\tilde{E}_{\mathrm{e}}\hat{\mathrm{e}} \tag{3.6}$$

for which two scalar coupled-wave equations can be obtained. This decomposition is natural when modeling a pure type-I parametric down-conversion process, where one polarization is associated to the input pump (p) and the other is associated to the generated down-converted (d) light. Going forward, we will therefore substitute $\tilde{E}_{\mathrm{e}}\rightarrow\tilde{E}_{\mathrm{p}}$ and $\tilde{E}_{\mathrm{o}}\rightarrow\tilde{E}_{\mathrm{d}}$ to highlight how these equations are applied in the specific case of high-gain PDC in Chapter 5. One should however keep in mind that despite this notation, nonlinear polarization terms corresponding to other nonlinear effects also contribute to the total fields, meaning that the output value of $\tilde{E}_{\mathrm{p}}$ could also include e.g. cascaded SHG of the down-converted light.

For both modes, we also introduce an envelope $\tilde{A}$ which is shifted in ω and k spaces

$$\tilde{E}_{\mathrm{j}}=\frac{1}{2}\left(\tilde{A}_{\mathrm{j}}\left(\omega-\omega_{\mathrm{j}}\right)e^{-ik_{\mathrm{j}}z}+\tilde{A}_{\mathrm{j}}^{*}\left(-\omega-\omega_{\mathrm{j}}\right)e^{ik_{\mathrm{j}}z}\right) \tag{3.7}$$

where the index $\mathrm{j}=\{\mathrm{p},\mathrm{d}\}$ denotes the pump (p) or down-converted (d) mode, and ω_{j} (k_{j}) is the center angular frequency (longitudinal wavenumber) of envelope $\tilde{A}_{\mathrm{j}}$. This representation makes no assumption about the bandwidth of the fields $\tilde{E}_{\mathrm{j}}$, and only serves to ease numerical calculation 1) by reducing the required grid size by centering it around the carrier frequency of each mode and 2) by removing the fast oscillation of the carrier phase from the calculation.

In typical finite-difference schemes, ω_{j} is usually chosen as the central frequency of mode j, and from there the wavenumber is calculated as $k_{\mathrm{j}}=\omega_{\mathrm{j}}n_{\mathrm{j}}(\omega_{\mathrm{j}})/c$. This however usually leaves a phase mismatch factor $e^{i\Delta kz}$ which is observed to behave poorly numerically with the numerical integration technique used. So, we instead choose to set $\omega_{\mathrm{d}}=\omega_{\mathrm{p}}/2$ and $k_{\mathrm{d}}=k_{\mathrm{p}}/2$ to obtain a simpler set of equations which *a priori* assume a perfectly phase-matched, degenerate down-conversion process, and then lets the dispersion term $-ik_z\tilde{\mathbf{E}}$ in

equation (3.5) correct this initial assumption during the numerical simulations.

Finally, to further improve numerical stability, we introduce a reference frame that moves with the group velocity of the pump $v_{\mathrm{g}} = (\partial k_{\mathrm{p}}/\partial\omega)^{-1}$. The envelopes $\tilde{A}_{\mathrm{j}}$ become

$$\tilde{A}_{\mathrm{j}}\left(\omega-\omega_{\mathrm{j}}\right) \rightarrow \tilde{A}_{\mathrm{j}}\left(\omega-\omega_{\mathrm{j}}\right) e^{iv_{\mathrm{g}}^{-1}(\omega-\omega_{\mathrm{j}})z} \tag{3.8}$$

which can be inserted into equation (3.5) to obtain 2 final coupled propagation equations

$$\frac{\partial\tilde{A}_{\mathrm{d}}}{\partial z} = -i\left(k_z - \frac{k_{\mathrm{p}}}{2} - v_{\mathrm{g}}^{-1}(\omega-\omega_{\mathrm{p}}/2)\right)\tilde{A}_{\mathrm{d}} - \frac{i\omega^2}{2k_z\epsilon_0 c^2}\tilde{P}_{\mathrm{d}}^{\mathrm{NL}} \tag{3.9a}$$

$$\frac{\partial\tilde{A}_{\mathrm{p}}}{\partial z} = -i\left(k_z - k_{\mathrm{p}} - v_{\mathrm{g}}^{-1}(\omega-\omega_{\mathrm{p}})\right)\tilde{A}_{\mathrm{p}} - \frac{i\omega^2}{2k_z\epsilon_0 c^2}\tilde{P}_{\mathrm{p}}^{\mathrm{NL}}\ . \tag{3.9b}$$

3.1.3 Nonlinear Polarization

For each mode, we expand the nonlinear polarization up to third order:

$$\tilde{\mathbf{P}}^{\mathrm{NL}} = \epsilon_0\left(\sum_{m=2}^{\infty}\chi^{(m)}\mathcal{F}_{x,y,t}\left\{\mathbf{E}^m(x,y,z,t)\right\}\right) \tag{3.10a}$$

$$\approx \epsilon_0\chi^{(2)}\mathcal{F}_{x,y,t}\left\{\mathbf{E}^2\right\} + \epsilon_0\chi^{(3)}\mathcal{F}_{x,y,t}\left\{\mathbf{E}^3\right\} \tag{3.10b}$$

and we conserve only terms which are 1- assumed to be phase-matched and 2- overlapping in frequency with the fields under consideration in the scenario being simulated. For the second-order nonlinear polarization, this include parametric down-conversion

$$\tilde{P}_{\mathrm{d}}^{\mathrm{PDC}} = \epsilon_0\chi^{(2)}\mathcal{F}_{x,y,t}\left\{A_{\mathrm{d}}^* A_{\mathrm{p}} e^{i\omega_{\mathrm{p}}t/2}\right\} \tag{3.11}$$

and its reverse process, second-harmonic generation (SHG)/sum frequency generation (SFG) of the BTBs

$$\tilde{P}_{\mathrm{p}}^{\mathrm{SHG}} = \epsilon_0\chi^{(2)}\mathcal{F}_{x,y,t}\left\{A_{\mathrm{d}}^2 e^{i\omega_{\mathrm{p}}t}\right\} \tag{3.12}$$

which simultaneously models depletion of the pump. A notable exclusion from the $\chi^{(2)}$ effects

is upconversion of the BTBs by the pump via SFG which is often present in the high-gain regime even when not phase-matched [27]. Inclusion of this term would however require much larger frequency grids, and its main effect is to introduce very low losses ($\sim 10^{-6}$) for the down-converted light mode which is negligible compared to other sources of losses, and it is therefore neglected.

As for the third-order nonlinear polarization, only the optical Kerr effect is modeled

$$\tilde{P}_{\mathrm{d}}^{\mathrm{Kerr}} = \epsilon_0 \chi^{(3)} \frac{3}{4} \mathcal{F}_{x,y,t} \left\{ \left(|A_{\mathrm{d}}|^2 + \frac{2}{3} |A_{\mathrm{p}}|^2 \right) A_{\mathrm{d}} e^{i\omega_{\mathrm{p}} t/2} \right\} \tag{3.13a}$$

$$\tilde{P}_{\mathrm{p}}^{\mathrm{Kerr}} = \epsilon_0 \chi^{(3)} \frac{3}{4} \mathcal{F}_{x,y,t} \left\{ \left(\frac{2}{3} |A_{\mathrm{d}}|^2 + |A_{\mathrm{p}}|^2 \right) A_{\mathrm{p}} e^{i\omega_{\mathrm{p}} t} \right\} \tag{3.13b}$$

where the degeneracy factor of 2/3 for the cross-polarized terms is here included under assumption of propagation in a isotropic medium [57], and here used as a first-order approximation for propagation in a birefringent medium.

3.1.4 Numerical Propagation

We implement a split-step Fourier method [182] where for each spatial step Δz of the simulation, every term in the right hand side of equations (3.9) is solved separately. For the dispersion term, we analytically solve the set of differential equations

$$\frac{\partial \tilde{A}_{\mathrm{d}}}{\partial z} = -i \left(k_z - \frac{k_{\mathrm{p}}}{2} - v_{\mathrm{g}}^{-1} (\omega - \omega_{\mathrm{p}}/2) \right) \tilde{A}_{\mathrm{d}} \tag{3.14a}$$

$$\frac{\partial \tilde{A}_{\mathrm{p}}}{\partial z} = -i \left(k_z - k_{\mathrm{p}} - v_{\mathrm{g}}^{-1} (\omega - \omega_{\mathrm{p}}) \right) \tilde{A}_{\mathrm{p}} \tag{3.14b}$$

which in frequency domain yields a simple multiplication of the envelopes by a linear propagation operator

$$\tilde{A}_{\mathrm{j}}(z + \Delta z) = \tilde{A}_{\mathrm{j}}(z) \exp \left(-i \left(k_z - k_{\mathrm{j}} - v_{\mathrm{g}}^{-1} (\omega - \omega_{\mathrm{j}}) \right) \Delta z \right) \ . \tag{3.15}$$

Then, the nonlinear polarization term is numerically integrated in a standard fashion using the explicit fourth-order Runge-Kutta method [182]. After a step-size Δz, the envelopes

become

$$\tilde{A}_{\mathrm{d}}(z+\Delta z) = \tilde{A}_{\mathrm{d}}(z) + \frac{\Delta z}{6}\left(k_{\mathrm{d},1} + 2k_{\mathrm{d},2} + 2k_{\mathrm{d},3} + k_{\mathrm{d},4}\right) \tag{3.16a}$$

$$\tilde{A}_{\mathrm{p}}(z+\Delta z) = \tilde{A}_{\mathrm{p}}(z) + \frac{\Delta z}{6}\left(k_{\mathrm{p},1} + 2k_{\mathrm{p},2} + 2k_{\mathrm{p},3} + k_{\mathrm{p},4}\right) \tag{3.16b}$$

with

$$k_{(\mathrm{d,p}),1} = -\frac{i\omega^2}{2k_z\epsilon_0 c^2}\tilde{P}^{\mathrm{NL}}_{(\mathrm{d,p})}\left(z, \tilde{A}_{\mathrm{d}}, \tilde{A}_{\mathrm{p}}\right) \tag{3.17a}$$

$$k_{(\mathrm{d,p}),2} = -\frac{i\omega^2}{2k_z\epsilon_0 c^2}\tilde{P}^{\mathrm{NL}}_{(\mathrm{d,p})}\left(z + \frac{\Delta z}{2}, \tilde{A}_{\mathrm{d}} + \frac{k_{\mathrm{d},1}}{2}, \tilde{A}_{\mathrm{p}} + \frac{k_{\mathrm{p},1}}{2}\right) \tag{3.17b}$$

$$k_{(\mathrm{d,p}),3} = -\frac{i\omega^2}{2k_z\epsilon_0 c^2}\tilde{P}^{\mathrm{NL}}_{(\mathrm{d,p})}\left(z + \frac{\Delta z}{2}, \tilde{A}_{\mathrm{d}} + \frac{k_{\mathrm{d},2}}{2}, \tilde{A}_{\mathrm{p}} + \frac{k_{\mathrm{p},2}}{2}\right) \tag{3.17c}$$

$$k_{(\mathrm{d,p}),4} = -\frac{i\omega^2}{2k_z\epsilon_0 c^2}\tilde{P}^{\mathrm{NL}}_{(\mathrm{d,p})}\left(z + \Delta z, \tilde{A}_{\mathrm{d}} + k_{\mathrm{d},3}, \tilde{A}_{\mathrm{p}} + k_{\mathrm{p},3}\right) \tag{3.17d}$$

where $\tilde{P}^{\mathrm{NL}}_{(\mathrm{d,p})}$ is the sum of all the terms listed in section 3.1.3 when the highest accuracy is required. When the effects of self-steepening [184] can be neglected, i.e. for narrowband pulses or when the nonlinear phase-shift is low, the computational load of including the Kerr effect can be significantly reduced by applying a narrowband approximation $\omega \approx \omega_{\mathrm{j}}$ on its nonlinear polarization term (3.13). Indeed, this approximation allows for th eKerr term to be solved in time-domain, separately from the $\chi(2)$ terms, yielding the pair of equations

$$\frac{\partial A_{\mathrm{d}}}{\partial z} = -i\frac{\omega_{\mathrm{p}}}{2c}\left(n_{2,\mathrm{SPM}}I_{\mathrm{d}} + n_{2,\mathrm{XPM}}I_{\mathrm{p}}\right)A_{\mathrm{d}} \tag{3.18a}$$

$$\frac{\partial A_{\mathrm{p}}}{\partial z} = -i\frac{\omega_{\mathrm{p}}}{c}\left(n_{2,\mathrm{SPM}}I_{\mathrm{p}} + n_{2,\mathrm{XPM}}I_{\mathrm{d}}\right)A_{\mathrm{p}} \tag{3.18b}$$

where $I_{\mathrm{j}} = \epsilon_0 n(\omega_{\mathrm{j}})c|A_{\mathrm{j}}|^2/2$ is the optical intensity of mode j, and $n_2 = 3\chi^{(3)}/2n\epsilon_0 c$ is the Kerr nonlinear index for either self-phase modulation (SPM) or cross-phase modulation (XPM) [57]. These equations are then solved analytically by assuming that I_{d} and I_{p} remain approximately constant over one step size ΔZ, in which case the solutions are

$$\tilde{A}_{\mathrm{d}}(z+\Delta z) = \tilde{A}_{\mathrm{d}}(z)\exp\left(-i\frac{\omega_{\mathrm{p}}}{2c}\left(n_{2,\mathrm{SPM}}I_{\mathrm{d}} + n_{2,\mathrm{XPM}}I_{\mathrm{p}}\right)\Delta z\right) \tag{3.19a}$$

$$\tilde{A}_{\mathrm{p}}(z+\Delta z) = \tilde{A}_{\mathrm{p}}(z)\exp\left(-i\frac{\omega_{\mathrm{p}}}{c}\left(n_{2,\mathrm{SPM}}I_{\mathrm{p}} + n_{2,\mathrm{XPM}}I_{\mathrm{d}}\right)\Delta z\right)\ . \tag{3.19b}$$

The numerical solver is implemented in Python, using the cupy package to run the main computation loop on Nvidia GPUs with the CUDA library. It has been tested with a desktop RTX 2060 and a mobile RTX 3050, taking on the order of 2 minutes to fully solve the pulse propagation with typical parameters as used in chapter 5.

3.1.5 Vacuum-Equivalent Seed

We first determine the vacuum mode density g contained in the numerical grid. To implement the split-step Fourier method, we must consider a 3D box with spatial lengths L_x, L_y and L_z with periodic boundary conditions. In this scenario, the number of modes per unit wavevector $\mathrm{d}\kappa$ and unit solid angle $\mathrm{d}\Omega$ is

$$g(\kappa,\Omega)\mathrm{d}\kappa\mathrm{d}\Omega = \frac{\kappa^2 L_x L_y L_z}{(2\pi)^3}\mathrm{d}\kappa\mathrm{d}\Omega\ . \tag{3.20}$$

The solid angle $\mathrm{d}\Omega$ of a wavevector of norm κ over an "area" $\mathrm{d}k_x\mathrm{d}k_y$ is

$$\mathrm{d}\Omega = \frac{\sqrt{\kappa^2 - k_x^2 - k_y^2}}{\kappa^3}\mathrm{d}k_x\mathrm{d}k_y \tag{3.21}$$

which once inserted into equation (3.20) yields

$$g(\kappa,k_x,k_y)\mathrm{d}\kappa\mathrm{d}k_x\mathrm{d}k_y = \frac{\sqrt{\kappa^2 - k_x^2 - k_y^2}L_x L_y L_z}{(2\pi)^3\kappa}\mathrm{d}\kappa\mathrm{d}k_x\mathrm{d}k_y\ . \tag{3.22}$$

Next, we consider the dispersion relation $\kappa = \omega n/c$ of the nonlinear medium, which implies $\mathrm{d}\kappa = \mathrm{d}\omega/v_{\mathrm{g}}$. We also convert the longitudinal extent $L_z = v_{\mathrm{g}}T$, where T is the width of the temporal grid, and obtain

$$g(\omega,k_x,k_y)\mathrm{d}\omega\mathrm{d}k_x\mathrm{d}k_y = \frac{\sqrt{(\omega n/c)^2 - k_x^2 - k_y^2}L_x L_y T}{(2\pi)^3\omega n/c}\mathrm{d}\omega\mathrm{d}k_x\mathrm{d}k_y \tag{3.23}$$

Finally, we assume from quantum theory that each monochromatic mode contains a vacuum-equivalent energy of half a photon $E_0 = \hbar\omega/2$ to find the power density of the semi-classical seed

$$I_{\mathrm{vac}}(\omega, k_x, k_y) = \frac{\hbar\omega}{2} g(\omega, k_x, k_y) = \hbar \frac{\sqrt{(\omega n/c)^2 - k_x^2 - k_y^2} L_x L_y T}{2(2\pi)^3 n/c} \tag{3.24}$$

and a spectral electric field amplitude density

$$|E_{\mathrm{vac}}(\omega, k_x, k_y)| = \sqrt{\frac{2}{n\epsilon_0 c} I_{\mathrm{vac}}(\omega, k_x, k_y)} \tag{3.25}$$

which is fixed from one simulation to the next. The only parameter which changes is the spectral phase : for each monochromatic mode, a pseudo-random phase following an uniform distribution over 2π and which is uncorrelated from mode to mode is set at the start of every simulation in order to classically reproduce the statistical fluctuations of the quantum vacuum field.

3.1.6 Input Pump Beam

The distribution in spacetime of the input pump is assumed to be a separable function of space and time, i.e. $A_{\mathrm{p}}(z = 0, x, y, t) \propto A_{\mathrm{T}}(x, y) A_t(t)$. The temporal envelope $A_t(t)$ is determined from experimental measurements of the shape of the pulse that are presented in section 3.3.3. In absence of a precise characterization of the transverse spatial distribution of the beam, it is approximated as a Gaussian beam with independent beam waists $\mathrm{w}_{0,x}$ and $\mathrm{w}_{0,y}$ and focal planes across the x and y axes that are fitted to the measured beam shape on a Si camera

$$A_{\mathrm{T}}(x, y) = X(x)Y(y) = \frac{e^{-ik_0 \frac{x^2}{2q_x(z_x)}}}{\sqrt{q_x(z_x)}} \frac{e^{-ik_0 \frac{y^2}{2q_y(z_y)}}}{\sqrt{q_y(z_y)}} \tag{3.26}$$

where $q_{(x,y)} = z_{(x,y)} + i z_{\mathrm{R},(x,y)}$ is the complex beam parameter in the x and y directions, $z_{(x,y)}$ is the longitudinal distance between the focal planes of the beam and the entry face of the nonlinear medium, and $z_{\mathrm{R},(x,y)} = \pi n \mathrm{w}_0^2/\lambda_0$ is the Rayleigh range. In the implementation, $X(x)$ and $Y(y)$ are first calculated in their focal plane, and then the beam is propagated (forward or backward) to the entry face of the nonlinear medium using ray transfer matrix analysis with the transformations

$$q(z + \Delta z) = \Delta z + q(z) \tag{3.27}$$

for free-space propagation, and

$$q_2 = \frac{n_2}{n_1} q_1 \tag{3.28}$$

for refraction at a flat interface going from a medium with refractive index n_1 to a medium with refractive index n_2.

3.2 Experimental Characterization Methods

3.2.1 Spectrum Statistics

Optical spectra presented throughout this thesis have all been acquired using off-the-shelf, compact USB spectrometers from Ocean Insight (USB2000 and HR2000+ for UV-VIS-NIR spectra, NIRQUEST for NIR spectra), using an in-house python code which automatizes data acquisition. In all cases, the free space sources are focused directly onto the input slit of the spectrometer.

For classical sources where only the average spectrum is measured, the integration time is adjusted to exploit the full dynamic range of the instrument. For statistical measurements (expectation value, variance, covariance) of BTBs, the integration time is instead reduced to 1 ms and the repetition rate of the main laser system is reduced to 994 Hz. In the absence of synchronization electronics, this strategy ensures the spectrometer acquires at most one laser shot per integration, at the price of having 0.6% of spectra being acquired under dark conditions.

3.2.2 Photon Statistics

Modern photon number resolving detectors can go up to 100 photons [185]. Yet, photocounts experiments can still be performed in the macroscopic regime, albeit with a multi-photon resolution.

To measure the photon statistics of a given pulse train, it is focused onto the active area of an amplified photodiode, producing a voltage pulse $V(t)$ with an area proportional to the number of incident photons n

$$\left\langle \int V(t)\,\mathrm{d}t \right\rangle = Ge\eta n \tag{3.29}$$

where G is the gain of the amplification circuit (in $\mathrm{V\,A^{-1}}$), e is the elementary charge, η the quantum efficiency of the detector, and $\langle\ \rangle$ denotes the expectation value. To efficiently integrate the voltage pulse, the photodiodes are connected to a digital "boxcar" integrator [186], which performs real time calculation of the average voltage V_{bxr} over a given time window of length T synchronized with the pulse train

$$V_{\mathrm{bxr}} = \frac{1}{N}\sum_{i=0}^{N} V(t_i) \approx \frac{1}{T}\int V(t)\,\mathrm{d}t \tag{3.30}$$

where the last approximation holds if the sampling rate of the digitization is much faster than the photodiode bandwidth and if the boxcar window length T is much larger than the voltage pulse duration. The number of photons contained in the i^{th} pulse can therefore be approximated by

$$n_i \approx \frac{T}{Ge\eta} V_{\mathrm{bxr},i} \tag{3.31}$$

giving a direct measurements of the photon number from an integrated voltage. In practice however, better signal-to-noise performance can be obtained by matching the boxcar window to approximately the full-width at half maximum (FWHM) of the voltage pulse [186], in which case the approximation (3.30) cannot be used and a separate measurement of e.g. the average power of the pulse train is necessary to perform the conversion.

Estimation of Population Statistical Moments From Sample Statistics

Analysis of photon statistics involves estimation of the statistical properties of its source (mean, variance, $g^{(2)}$, NRF, etc.) from a finite sample of size M. This section presents the estimators used in this thesis and the associated standard error.

First, the population mean $\langle n \rangle$ is estimated from the sample mean μ_n. The standard error $\Delta\mu$ is then estimated from the sample standard deviation σ_n via the law of large numbers [187]

$$\Delta\mu = \frac{\sigma}{\sqrt{M}}\ . \tag{3.32}$$

Then, the population variance $\Delta^2(n)$ is estimated from the sample variance σ_n^2. Its standard error $\Delta\sigma^2$ is then given by [187, p. 438]

$$\Delta\sigma^2 = \sigma^2\sqrt{\frac{1}{M}\left(\kappa - \frac{M-3}{M-1}\right)} \tag{3.33}$$

where κ is the kurtosis of the distribution. For the types of sources studied in this thesis, the value of κ ranges between 3 (for coherent light following a normal distribution) and 6 (for thermal light following an exponential distribution). The later value is used as an upper bound for error estimation throughout this thesis, but it is left here as κ for generality. When the sample size $M \gg 1$, the standard error on the sample variance can be estimated as

$$\Delta\sigma^2 \approx \sigma^2\sqrt{\frac{\kappa-1}{M}}\ . \tag{3.34}$$

Since all other statistical parameters presented in this thesis are calculated from the sample mean and variance, their standard error can be estimated from equations (3.32) and (3.34) using the propagation of errors [188]

$$\Delta f(\mu,\sigma^2) \approx \sqrt{\left(\frac{\partial f}{\partial \mu}\right)^2(\Delta\mu)^2 + \left(\frac{\partial f}{\partial \sigma^2}\right)^2(\Delta\sigma^2)^2}\ . \tag{3.35}$$

First, for the standard deviation

$$\mathrm{STD}(n) \approx \sigma = \sqrt{\sigma^2} \tag{3.36}$$

we find a standard error

$$\Delta\sigma = \sqrt{\left(\frac{\partial\sigma}{\partial\mu}\right)^2(\Delta\mu)^2 + \left(\frac{\partial\sigma}{\partial\sigma^2}\right)^2(\Delta\sigma^2)^2} \tag{3.37a}$$

$$= \sqrt{\left(\frac{1}{2\sigma}\right)^2\left(\sigma^2\sqrt{\frac{\kappa-1}{M}}\right)^2} \tag{3.37b}$$

$$= \frac{\sigma}{2}\sqrt{\left(\frac{\kappa-1}{M}\right)}\ . \tag{3.37c}$$

Next, for the zero-delay auto-correlation function

$$g^{(2)} \approx \frac{\sigma^2}{\mu^2} + 1 \tag{3.38}$$

where $\mu \geq 1$ is assumed, we find a standard error

$$\Delta g^{(2)} = \sqrt{\left(\frac{\partial g^{(2)}(0)}{\partial \mu}\right)^2 (\Delta\mu)^2 + \left(\frac{\partial g^{(2)}(0)}{\partial \sigma^2}\right)^2 (\Delta\sigma^2)^2} \tag{3.39a}$$

$$= \sqrt{\left(-2\frac{\sigma^2}{\mu^3}\right)^2 \left(\frac{\sigma}{\sqrt{M}}\right)^2 + \left(\frac{1}{\mu^2}\right)^2 \left(\sigma^2\sqrt{\frac{\kappa-1}{M}}\right)^2} \tag{3.39b}$$

$$= \left(g^{(2)} - 1\right)\sqrt{\frac{4\left(g^{(2)}-1\right)+\kappa-1}{M}}\,. \tag{3.39c}$$

Then, for the Schmidt number estimated from $g^{(2)}$

$$K = \frac{g_1^{(2)} - 1}{g^{(2)} - 1} = \frac{1}{g^{(2)} - 1} \approx \frac{\mu^2}{\sigma^2} \tag{3.40}$$

where the single-mode value $g_1^{(2)} = 2$ is assumed for BTBs, we find a standard error

$$\Delta K = \sqrt{\left(\frac{\partial K}{\partial \mu}\right)^2 (\Delta\mu)^2 + \left(\frac{\partial K}{\partial \sigma^2}\right)^2 (\Delta\sigma^2)^2} \tag{3.41a}$$

$$= \sqrt{\left(2\frac{\mu}{\sigma^2}\right)^2 \left(\frac{\sigma}{\sqrt{M}}\right)^2 + \left(-\frac{\mu^2}{\sigma^4}\right)^2 \left(\sigma^2\sqrt{\frac{\kappa-1}{M}}\right)^2} \tag{3.41b}$$

$$= \sqrt{\frac{4K + K^2(\kappa-1)}{M}}\,. \tag{3.41c}$$

Finally, for the noise reduction factor (NRF)

$$\mathrm{NRF} = \frac{\Delta^2(n_-)}{\langle n_+ \rangle} \approx \frac{\sigma_-^2}{\mu_+} \tag{3.42}$$

where the subscripts "$-$" and "$+$" denote a photon number difference and sum respectively, we find a standard error

$$\Delta\mathrm{NRF} = \sqrt{\left(\frac{\partial \mathrm{NRF}}{\partial \mu_+}\right)^2 (\Delta\mu_+)^2 + \left(\frac{\partial \mathrm{NRF}}{\partial \sigma_-^2}\right)^2 (\Delta\sigma_-^2)^2} \tag{3.43a}$$

$$= \sqrt{\left(-\frac{\sigma_-^2}{\mu_+^2}\right)^2 \left(\frac{\sigma_+}{\sqrt{M}}\right)^2 + \left(\frac{1}{\mu_+}\right)^2 \left(\sigma_-^2 \sqrt{\frac{\kappa-1}{M}}\right)^2} \tag{3.43b}$$

$$= \mathrm{NRF}\sqrt{\frac{1}{KM} + \frac{\kappa-1}{M}}\,. \tag{3.43c}$$

3.2.3 Pulse Shape

The pulse shape of the various optical sources used throughout this thesis have been measured using either or both of two standard characterization techniques: frequency-resolved optical gating (FROG) and two-dimensional spectral shearing interferometry (2DSI). As detailed in Chapter 2, FROG usually works best for multi-cycle pulses (>10 fs) while 2DSI works best for few-cycles (<10 fs). A compact, homemade implementation of both techniques are assembled on the same optical breadboard with the same input leading to a mirror mounted on a magnetic base, enabling quick switching between the two. Details of the two implementations are presented here.

Frequency-resolved Optical Gating

The schematic of the FROG is presented in Figure 3.1. The pulse under study is first split into two copies by a thin, metal-coated beamsplitter. The two copies are retroreflected back together onto the two input ports of a second beamsplitter. One of the two retroreflectors is mounted on top of a piezoelectric stage (P-625.1CD, Physik Instrumente), enabling precise control over the temporal delay between the two copies. The pulses are then focused together by a single parabolic mirror into a 10 µm thick beta barium borate (BBO) crystal cut for type I phase matching of SFG. The generated sum frequency (SF) light is spatially filtered from its fundamental by an iris and then refocused onto the input slit of a spectrometer (USB2000, Ocean Insight). Data acquisition from the spectrometer and control of the stage is performed via an in-house python graphical user interface. The pulse shape is retrieved with the common pulse retrieval algorithm (COPRA) [113], using a modified version of its publicly-available python implementation Python for Pulse Retrieval (pypret). The pypret package also contains implementations of other popular FROG retrieval algorithms, including the principal components generalized projections algorithm (PCGPA) [109] and the ptycho-graphical iterative engine (PIE) [110]. A separate measurement of the fundamental spectrum

can be supplied to the retrieval algorithm to help with convergence.

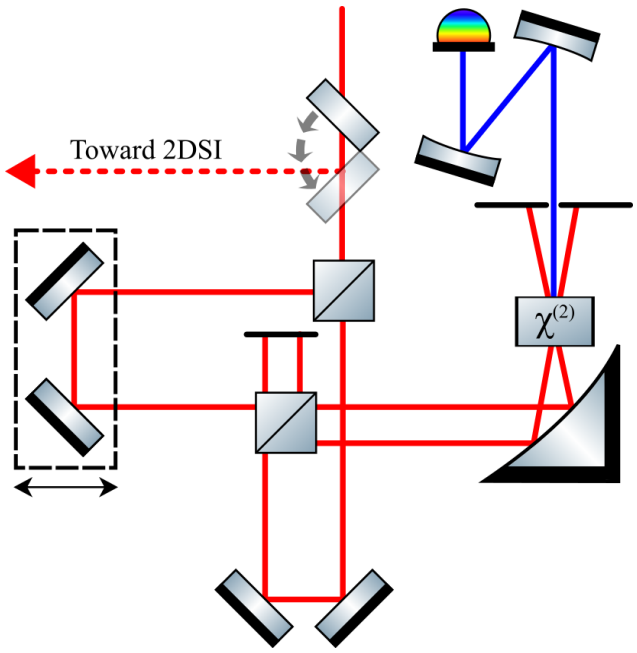

Figure 3.1 Schematic of the FROG implementation.

Two-dimensional Spectral Shearing Interferometry

The schematic of the 2DSI is presented in Figure 3.2. First, a weak and dispersionless copy of the pulse under study is created using the Fresnel reflection from a beam sampler (BSF10-B, Thorlabs). The rest of the pulse energy is then used to create two copropagating and highly dispersed copies of the pulse. The splitting and recombination is performed by sending the pulse through a cube beamsplitter (BS014, Thorlabs) twice, with an adjustable phase controlled via the same piezoelectric stage as in the FROG implementation. These two copies are naturally dispersed by linear propagation through the initial beam sampler, the 1 inch thick beamsplitter cube and an achromatic half-wave plate (AHWP05M-980, Thorlabs).

The three pulses (1 without added dispersion, 2 highly dispersed) are finally focused together by a single parabolic mirror into a 10 µm thick BBO crystal cut for type II phase matching of SFG. The generated SF light is spatially filtered from its fundamental by an iris and then refocused onto the input slit of a spectrometer (USB2000, Ocean Insight). Data acquisition from the spectrometer and control of the stage is performed via an in-house python graphical user interface. The pulse shape is then calculated using an in-house implementation of the standard 2DSI phase reconstruction algorithm [119, 120]. The fundamental spectrum can be estimated from the spectrum of the SFG, or it can be measured separately.

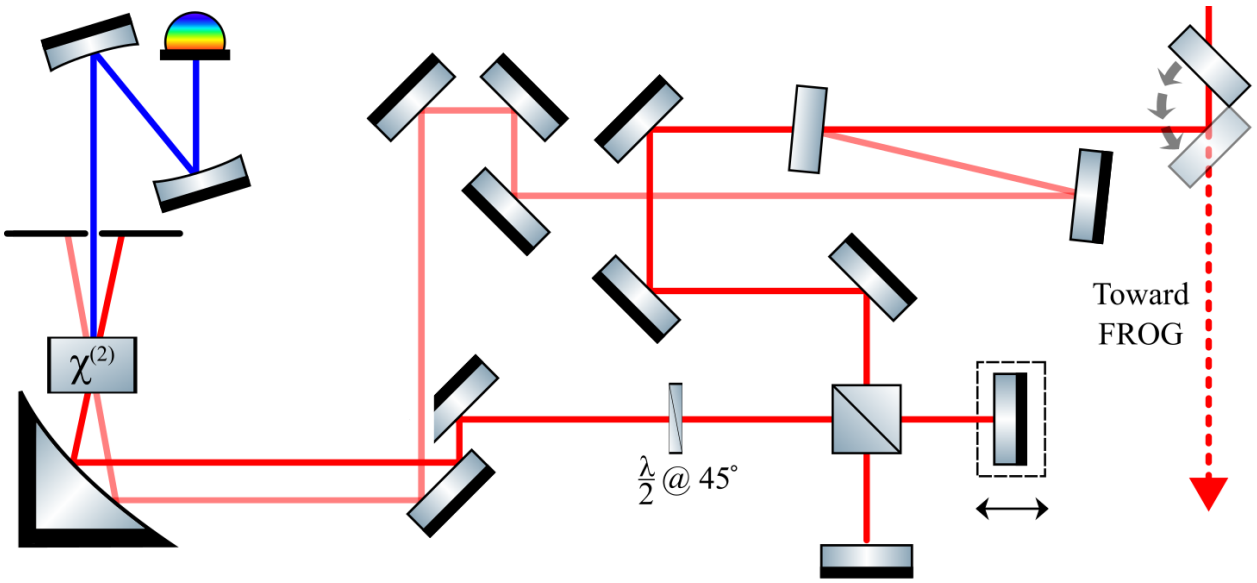

Figure 3.2 Schematic of the 2DSI implementation.

3.3 Twin Beams Source Design

3.3.1 Main Laser System

The main laser sytem driving all the experiments presented in this thesis is a Pharos Yb:KGW regenerative amplifier from Light Conversion [189]. The specifications of the particular unit used are summarized in table 3.1. The laser is always set to its minimal pulse energy setting of 20 µJ, such that the experiments may eventually be scaled up to operate at the maximum repetition rate of 993.9 kHz. However, for most experiments and measurements presented here, the repetition rate is reduced by the integrated pulse picker to 100 kHz or less. The reason for the down-picking is to match the acquisition bandwidth of some slower detectors (e.g. spectrometers, cameras) and to avoid thermal lensing effects, which have been observed at repetition rates of 200 kHz and above.

3.3.2 Design Criteria

Nonlinear Medium and Phase-Matching Bandwidth

First, in order to prepare BTBs with a few-cycle duration, the first step is to find a nonlinear medium with a suitable phase-matching bandwidth. As detailed in section 2.1.2, group velocity dispersion (GVD) is most often the limiting factor for the phase-matching bandwidth of nonlinear processes. A strategy to minimize its effects is to then operate the PDC process

Table 3.1 Pharos specifications

Model	PH2-20W-SP
Carrier wavelength	1026 nm
Average power	Up to 20W
Compressed pulse duration	260 fs
Pulse energy	20 µJ - 400 µJ
Repetition rate	Single shot - 993.9 kHz
Pulse-to-pulse energy stability	<0.5 %
Output beam waist	4 mm
M^2	<1.3
Polarization	p

at or near the zero-dispersion wavelength of the medium such that only the pump GVD term remains in equation (2.23). This scheme has been demonstrated with a narrowband pump and with collinear, quasi-degenerate, type-I PDC [178, 179], in which case the pump dispersion is negligible and the phase-matching bandwidth is limited only by fourth-order dispersion of the down-converted light. With a femtosecond pump however, its GVD cannot be neglected, but its detrimental effects can be mitigated with proper pulse precompression. Another advantage of this configuration is that the generated BTBs pulses should be nearly-transform-limited right at the output without need for further pulse compression.

Typical nonlinear media for the generation of bright squeezed light include e.g. lithium iodate [178], lithium niobate [70,179,190], KTP [62], and BBO [22,40,42,73,75,180,191,192]. Among those, BBO appears as not only the most popular choice, but also the medium which led to the brightest states to date [22, 40]. This can be attributed to its higher damage threshold and lower nonlinear index n_2 [193], which together allow the use of a pump with a higher peak intensity.

The zero-dispersion wavelength for the ordinary axis of BBO is at 1393 nm, which indicates a pump wavelength of 697 nm to obtain nearly-dispersionless down-converted light. Results from calculating the phase-matching function around these wavelength for noncollinear type-I PDC are presented in Figure 3.3. We find that phase-velocity and group-velocity matching can be achieved simultaneously at the zero-dispersion wavelength with a phase-matching angle $\theta = 22°$ and a noncollinearity angle $\alpha = 3.3°$. In practice, higher gain is expected if one of the two beams travels alongside the Poynting vector of the pump [24,177], i.e. with a noncollinearity angle $\alpha = 2.8°$. A slight detuning of the carrier frequency of the two beams is therefore expected in the experiment.

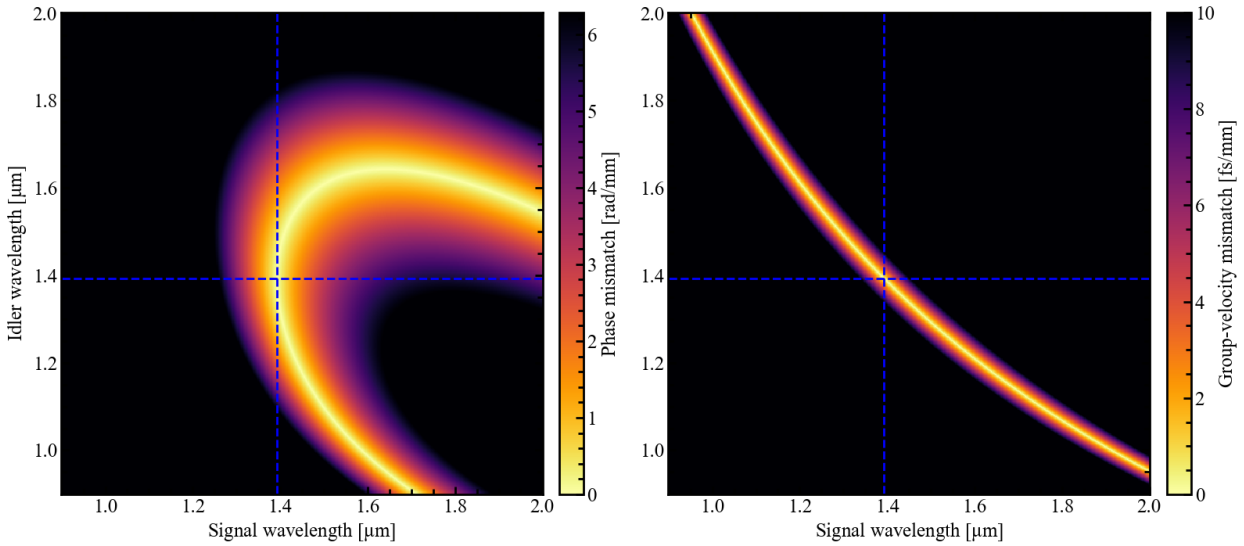

Figure 3.3 Phase- and group-velocity matching calculation for PDC in BBO. The blue dotted lines denote the zero-dispersion wavelength.

Parametric Gain

Next, we determine the minimal parametric gain needed for the source to drive nonperturbative nonlinear effects, using high-harmonic generation as an example. Recent advances in plasmonics have brought the threshold vacuum intensity to drive high-harmonic generation in the nonperturbative regime down to $0.03\,\mathrm{TW\,cm^{-2}}$ [58], compared to typical values of $30\,\mathrm{TW\,cm^{-2}}$ in rare gases [194] and $5\,\mathrm{TW\,cm^{-2}}$ in bulk crystals [195]. Considering a Gaussian pulse with FWHM duration Δt_{FWHM}, and a Gaussian transverse beam profile with a radius at $1/e^2$ of the maximal intensity w_0, the peak intensity is [56]

$$I_{\mathrm{peak}} = \frac{2U}{\sqrt{\pi/\log(16)}\Delta t_{\mathrm{FWHM}}\pi \mathrm{w}_0^2} \approx \frac{1.88U}{\Delta t_{\mathrm{FWHM}}\pi \mathrm{w}_0^2} \tag{3.44}$$

where U is the pulse energy. A target pulse energy for the source can now be established for the condition $I_{\mathrm{peak}} \geq 0.03\,\mathrm{TW\,cm^{-2}}$ by making assumptions about the pulse duration and the focused beam size. Conservatively assuming e.g. a 3-cycle pulse $\Delta t_{\mathrm{FWHM}} = 3\lambda_0/c = 14\,\mathrm{fs}$ focused down to a 5-wavelength-wide diameter $2\mathrm{w}_0 = 5\lambda_0 = 7\,\mu\mathrm{m}$, we find

$$U_{\mathrm{target}} = 86\,\mathrm{pJ}$$

which corresponds to a parametric gain $G = 10.8$ for an average photon energy $\hbar\omega = 0.14\,\mathrm{aJ}$. To avoid the detrimental effects of pump depletion which can appear even with %-level

conversion efficiencies [70, 142], we therefore target a pump energy budget of at least 100 nJ.

This target does not account for the higher repetition rate of the present source (1 MHz vs. 10 kHz in [58]), nor the statistical enhancement of multiphoton effects pumped with bunched light (a factor of 6 for BTBs [25] with the I^3 power scaling observed in [58]). Together, these two effects would reduce the required peak intensity by a factor $(600)^{(1/3)}$, setting a lower bound for the mean pulse energy

$$U_{\text{min}} = \frac{U_{\text{target}}}{(600)^{(1/3)}} = 10\,\text{pJ}$$

which corresponds to a parametric gain $G = 9.7$.

Pump Duration, Carrier-Envelope Phase Control, and Mode Selection

In the regime of extreme (nonperturbative) nonlinear optics, the response is sensitive not only on the amplitude of the driving pulse, but also on the maximal value of the electric field underneath the envelope [46,47,49]. For multi-cycle pulses, these two parameters are directly linked and can only be increased by an increase of the pulse energy, tighter focusing or by the use of shorter pulse. In the few-cycle regime however, where the pulse duration becomes comparable to the period of the carrier wave, the electric field strength also depends on the carrier-envelope phase (CEP).

For BTBs, achieving control over the CEP requires driving the source in the single-mode regime. Indeed, each downconverted modes in PDC have amplitudes and phases that are entirely uncorrelated to each other [23,143,191]. The envelope of pulses produced from PDC results from the superposition of all modes, and therefore in the multimode regime its shapes changes significantly from shot to shot. Meanwhile, the CEP of a pulse is only defined with respect to a single, well-defined envelope, a condition which is achieved only for a single-mode source.

In the low gain regime, the number of Schmidt modes is entirely determined by the frequency and angular bandwidth of the pump one one hand, and those of the phase-matching function on the other hand [62–64], with the single-mode limit being reached when the two coincide. In a spatio-temporal description, reaching the single-mode conditions therefore amounts to matching the space-time volume of the pump V_{pump} to the coherence volume V_{coh} of the amplified vacuum fluctuations [145], giving an approximate number of modes

$$K \sim \frac{V_{\text{pump}}}{V_{\text{coh}}} \,. \tag{3.45}$$

While this calculation can serve as a useful first-order approximation, it will typically overestimate the number of modes one experimentally observes in the high-gain regime. Indeed, as the gain increases (up to pump depletion), the number of modes naturally tends to diminish due to mode competition redistributing the relative weights of the Schmidt coefficients [63, 143, 196]. This reduction can be further accelerated by the diffraction [24, 73, 177] and dispersion [180] of high-order modes over the long interaction lengths typically necessary to reach the high gain regime. Furthermore, while the effective number of modes decreases, the overall bandwidth of the down-converted light increases with the gain [196], leading to an underestimation of V_{coh}.

For the present work, a pump duration $\Delta t_{\mathrm{p}} \leq 10\,\mathrm{fs}$ is selected to match a target pulse duration of approximately 2 cycles of the down-converted carrier wavelength ($\Delta t_{\mathrm{FWHM}} = 2\lambda_0/c = 9.33\,\mathrm{fs}$). Simulations performed with an early implementation of the numerical model presented in section 3.1 [1] indicated that the single-mode limit can be approached for this pulse duration and a focused beam diameter of $\sim$40 µm with a 4 mm thick BBO crystal, as long as the pump pulse reaches its compressed duration in the latter half of the interaction. This last condition can be seen as a temporal mode selection being performed progressively by the pump as it compresses, in a similar fashion to 2-crystal designs where diffraction [40, 73] and dispersion [180] effects restrict the number of modes that are amplified in the second crystal. The correspondence between the objectives of the project and the design criteria for the PDC source that have been derived here are summarized in table 3.2.

Table 3.2 Target design of the PDC source

Objective	**Design criteria**
Few-cycle pulses	PDC in BBO, pump @ 697 nm
Peak intensity $\geq 0.03\,\mathrm{TW\,cm^{-2}}$	100+ nJ pump energy
CEP control	sub-10 fs pump duration, 4-mm-thick crystal

3.3.3 Classical Ultrafast Pump Preparation

The pump pulse driving the PDC process is prepared in a homebuilt noncollinear optical parametric amplifier (NOPA). The overall design is based on existing state-of-the-art implementations [96,197,198], but it is customized toward the particular task of producing µJ-level sub-10 fs pulses in the visible to near infrared (VIS-NIR) range toward driving PDC in the near infrared (NIR). A conceptual schematic of the final NOPA design is presented in Figure 3.4 and a picture of the physical implementation is shown in Figure 3.5.

[1] This early version neglected all transverse effects, and had no $\chi^{(3)}$ term in the nonlinear polarization.

The pulse train from the Pharos system is first directed toward a quarter-turn periscope, which flips its polarization from p to s. From there, the overall design of the NOPA can be divided into four sections. The 20 µJ energy budget is split between the two first sections : (1) 2 µJ (10 %) is used to prepare a broadband seed via supercontinuum generation (SCG), and (2) 18 µJ (90 %) is used to prepare a high-power visible (VIS) pump via SHG.

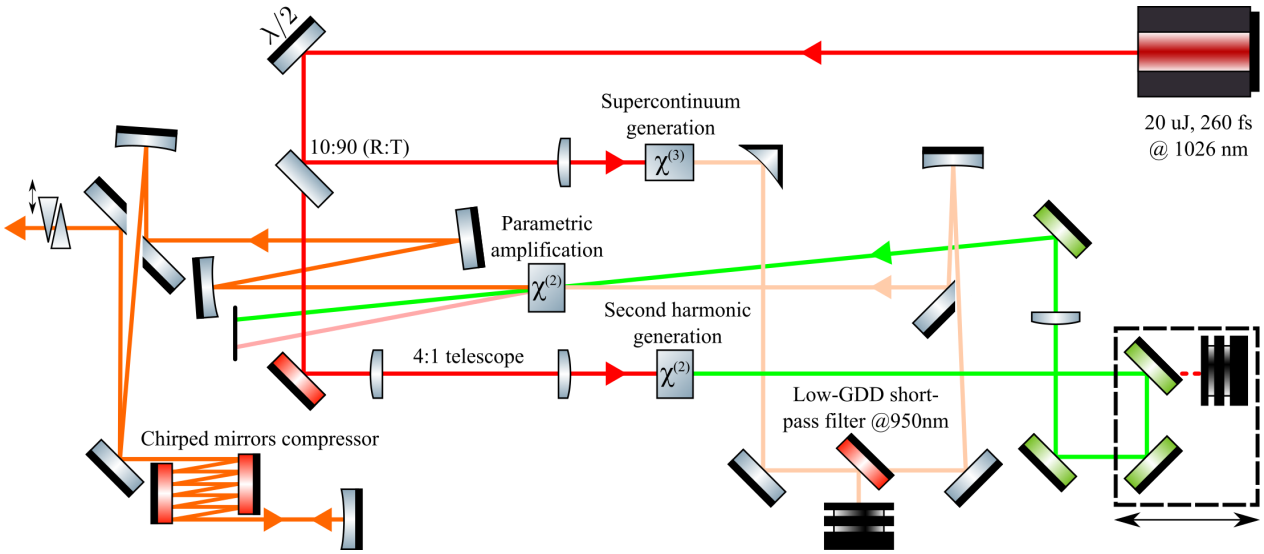

Figure 3.4 Schematic of the NOPA.

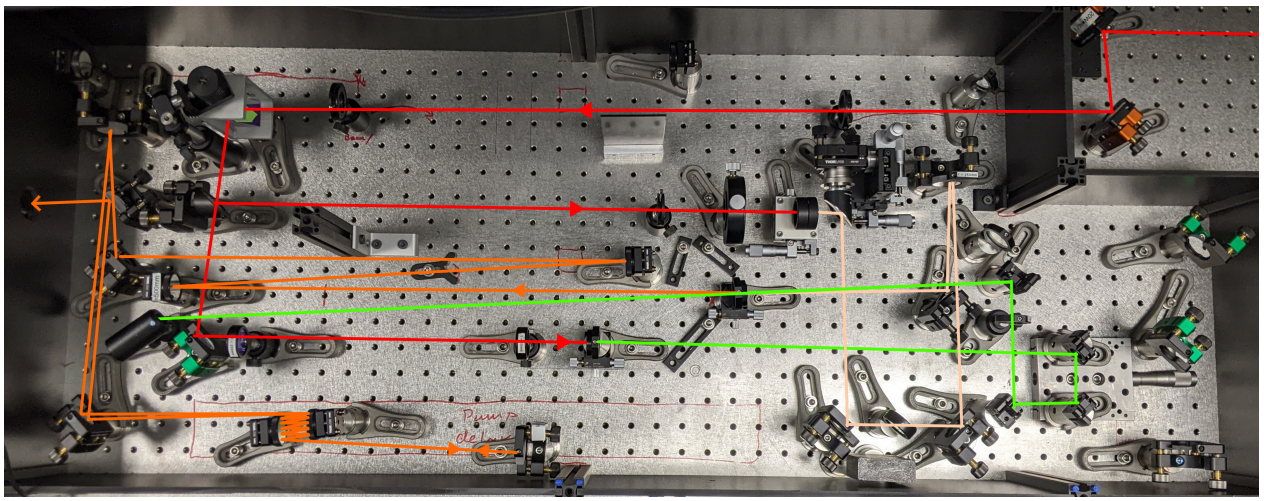

Figure 3.5 Picture of the NOPA with overlayed beam path

Then (3), the outputs of these two sections are nonlinearly mixed in a parametric amplification stage, transferring the optical power from the VIS pump to the broadband seed. Finally (4), this amplified output is compressed by multiple reflections on a pair of chirped

mirrors, which cancels the chromatic dispersion of the optics located both inside and outside the NOPA. Fine tuning of the dispersion can be performed by propagating the pulse through a pair of thin transparent wedged windows set at their Brewster angle right before the output, but for the experiments presented in this thesis this level of precision was not required. The specifications of the pulse train emitted at the output of the NOPA are summarized in table 3.3 and more details about the design of each section are presented in the following sections. The energy and duration of the output pulses are comparable to contemporary implementations of NOPA pumped with similar laser systems [96, 199].

Table 3.3 Summary of NOPA specifications

Pulse energy	1.4 µJ
Carrier wavelength	680 nm
Maximum repetition rate	1 MHz (small thermal lensing over 100 kHz)
Compressed pulse duration	9.5 fs
Fourier-limited pulse duration	8.3 fs
Precompressed pulse duration	120 fs (calculated)

Supercontinuum Seed

The broadband seed is generated via SCG in a bulk yttrium aluminium garnet (YAG) crystal. It is a popular choice for bulk SCG pumped at wavelengths near 1 µm due to its lack of birefringence, and its relatively high nonlinearity and optical damage threshold [181].

SCG is mediated by an interplay between third-order nonlinear phenomena (mostly self-phase modulation and self-focusing, although other effects e.g. Raman scattering and multiphoton absorption can become significant when strongly pumping) and linear propagation, i.e. chromatic dispersion and diffraction. The former extend the optical spectrum of the pump through multiphoton interactions, while the latter tend to impose a limit the extent of these interactions by pushing new optical components away from the main pulse.

The SCG pump is focused by a $f = 75$ mm fused-silica lens to a focal plane located about 5 cm before the entry face of the YAG crystal. This focusing geometry uses the divergence of the pump beam to balance out nonlinear self-focusing inside the YAG [181], which can lead to filamentation of the beam, pulse breakup and eventually optical damage of the medium. 3 different thickness of YAG were tested: 2 mm, 3 mm and 5 mm. The output spectrum obtained with all three crystals is presented in Fig 3.6.

For all three crystals, we observe an asymmetric broadening of the spectrum, with a relatively flat shape on the short wavelength side and an exponentially decaying shape on the long

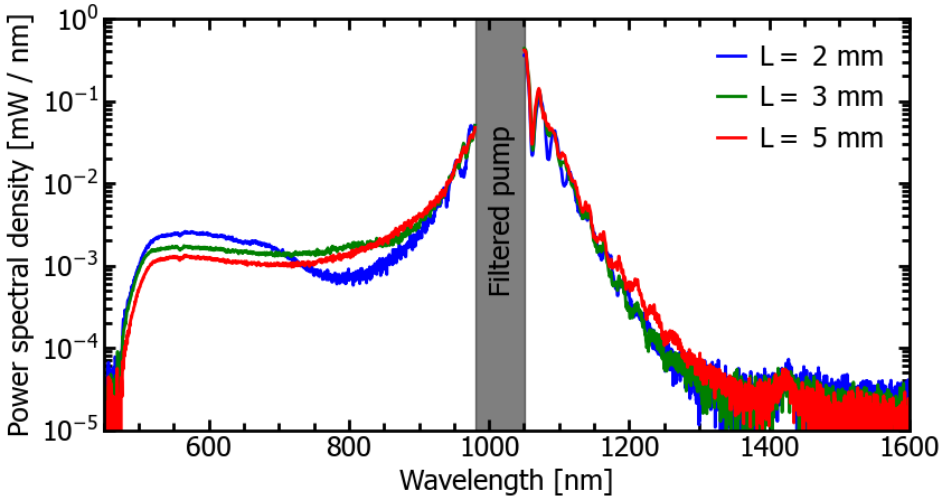

Figure 3.6 Supercontinuum spectra generated in YAG for 3 different crystal thicknesses L

wavelength side. The lower nonlinear phase shift in the thinnest crystal causes a dip in its spectrum around 800 nm, which would limit the achievable pulse duration out of the NOPA when using it as the seed. As for the two thicker crystals, they produce extremely similar spectra, implying that most of the nonlinear broadening occurs in the first 3 mm of propagation. As such, and in an attempt to reduce the overall chromatic dispersion of the seed in the setup, the 3 mm thick crystal is used in the final design.

After generation in YAG, the supercontinuum (SC) is collimated by a parabolic mirror and refocused toward the parametric amplification, after filtering the pump and the low-frequency part of the SC with a low-dispersion shortpass dielectric filter with a cut-off wavelength of 950 nm (Stock #14-030, Edmund Optics).

Efficient Second Harmonic Pump

To prepare a strong optical pump for the NOPA, a SHG process is driven using all the remaining energy (18 µJ) from the Pharos system. The nonlinear medium used is a 2 mm-thick BBO crystal, cut for type-I phase matching. BBO is used due to its high nonlinearity and damage threshold [57], helping toward achieving a high conversion efficiency. Its thickness is in turn selected due to the 260 fs pulse duration of the Pharos and the group velocity mismatch (GVM) of 99 fs mm^{-1} [87] for this specific process, which means that the fundamental and second harmonic (SH) pulses would not overlap anymore after roughly 2.6 mm of propagation.

For a monochromatic, flat-top fundamental beam with a constant optical intensity I, the

conversion efficiency of SHG is given by [56]

$$\eta = \tanh^2\left(\frac{g\sqrt{I}L}{2}\right) \tag{3.46}$$

where $g = \sqrt{(8d_{\text{eff}}\omega^2)/(\epsilon_0^3 c^3 n^3)}$ is a constant describing the overall strength of the nonlinear response of the medium, I is the intensity of the fundamental beam and L the length of the nonlinear medium. Experimentally, the intensity of the fundamental will most often be non-uniform, meaning that the more intense portions of the beam will be converted with a higher efficiency than its edges. If the space-time distribution of the intensity $I(\vec{r}, t)$ is known, one can consider this non-uniformity by calculating an average efficiency

$$\langle\eta\rangle = \frac{\int \eta(I) I \,\mathrm{d}\vec{r}\,\mathrm{d}t}{\int I \,\mathrm{d}\vec{r}\,\mathrm{d}t} \tag{3.47}$$

where the only assumption is that all diffraction and dispersion effects can be neglected throughout the nonlinear interaction. The former approximation can be applied here, since the high peak power of the fundamental (around 67 MW) permits the use of a collimated beam. However, a reduction of the conversion efficiency is to expected due to GVM pushing the SH pulse away from the fundamental throughout the propagation.

Figure 3.7 compares the measured SHG efficiency (blue dots) and the prediction of equation (3.47) (solid line), where a Gaussian intensity distribution is assumed in both space and time and the theoretical value of $g = 323\,\mathrm{mm\,kW^{-1}}$ [87, 198] is used. As expected, the measured SHG efficiency grows slower than the approximate theoretical prediction. By fitting the ratio between the measured and predicted efficiencies (dashed line), we find that GVM reduces the conversion efficiency by 25 %.

In the final design, the fundamental is resized to a 1 mm beam diameter by a pair of UV-fused silica lenses, yielding a peak pulse intensity of $16.6\,\mathrm{GW\,cm^{-2}}$. From extrapolating the fit in Figure 3.7, we find that this should push the SHG process to an efficiency of 64 %, yielding SH pulses with an energy of over 11.8 µJ. While tighter focusing of the fundamental could yield even higher conversion efficiency, this design is selected to keep the peak intensity to about 1 % of the damage threshold of BBO [200] to ensure good long-term stability of the NOPA. After reflection off of 4 consecutive dichroic separators (coating 103947, Layertec) to eliminate the fundamental, the measured energy of the SH pulses reaching the parametric amplification crystal is 11 µJ, for a total efficiency of over 59 %.

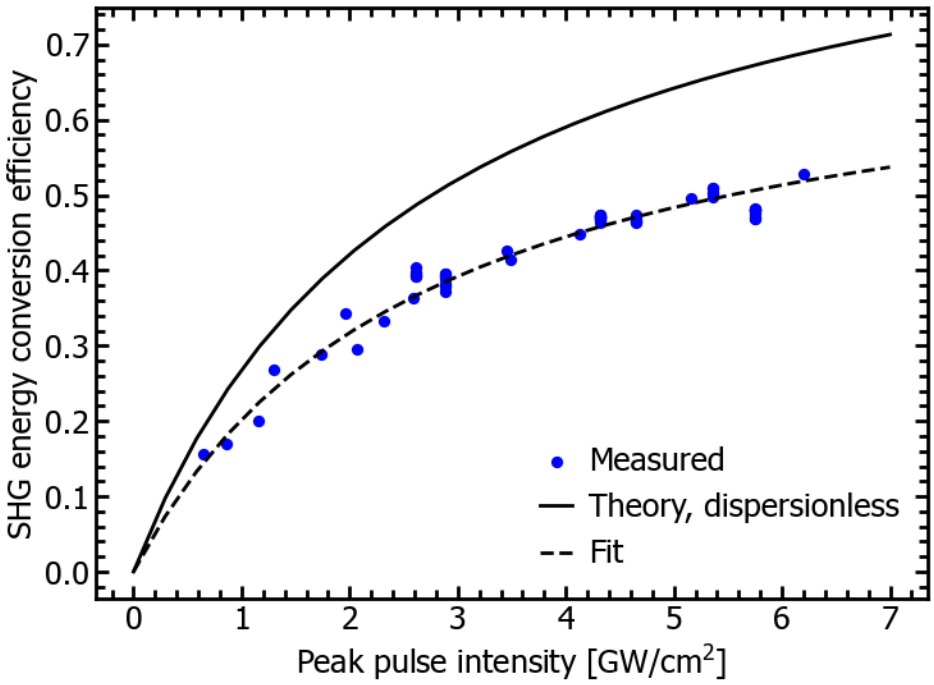

Figure 3.7 SHG conversion efficiency for a collimated Gaussian pump

Parametric Amplification and Pulse Compression

The SC seed and the SH pump are focused together inside a 1.5 mm thick BBO crystal cut for type-I phase matching, with an internal noncollinearity angle of 2.6°. Figure 3.8 compares the optical spectrum emitted at the output of the NOPA after the compression stage, with and without parametric amplification of the SC seed by the SH pump. Parametric amplification is observed in a bandwidth ranging from 580 nm to 860 nm, with a peak gain of over 900 at 640 nm, yielding a final pulse energy of 1.4 µJ and an overall power efficiency of 7 % for the entire NOPA.

The output amplified spectrum supports a transform-limited pulse duration of 8.3 fs, but the pulse is stretched in time due to chromatic dispersion in the YAG crystal, the shortpass filter and the parametric amplification BBO crystal. To compress the pulse train, it is reflected multiple times between a matched pair of chirped mirrors (coating 133200, Layertec) designed to introduce a nearly-constant group delay dispersion (GDD) of $-40\,\mathrm{fs}^2$ per reflection over the entire bandwidth. The beam is loosely focused on the mirror pair by a $f = 750$ mm concave spherical mirror and is then reflected back toward the mirror pair in a folded geometry to achieve up to 12 reflections per mirror ($-960\,\mathrm{fs}^2$). The number of reflections can be adjusted in multiples of 2 to produce nearly-compressed pulse at the output of the NOPA (6 reflections per mirror), or to precompress the pulse in anticipation of propagation through the shortpass

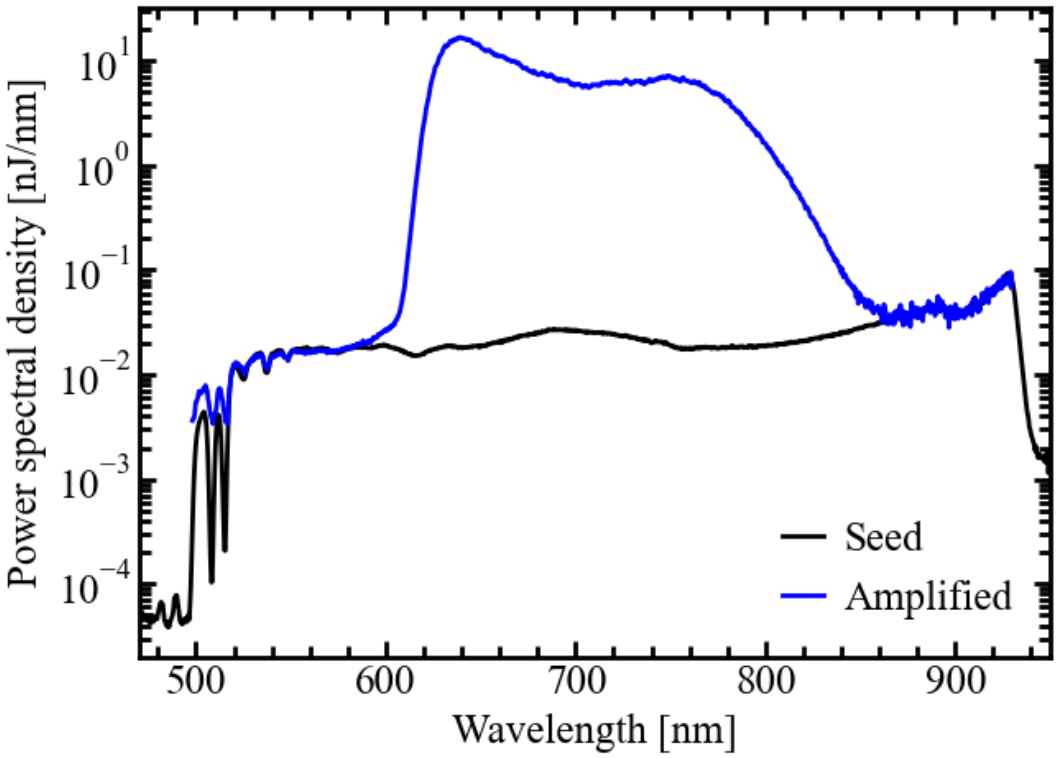

Figure 3.8 Optical spectrum outputted by the NOPA with and without parametric amplification.

filter (FELH0950, Layertec), the tunable neutral-density filter (NDL-25C-4, Thorlabs) and the PDC crystal that are placed past the compressor for certain experiments (12 reflections per mirror).

Figure 3.9 presents the pulse shape measured with FROG (top left trace, blue lines) and with 2DSI (bottom left trace, blue lines) when the compressor is adjusted to yield a compressed pulse. In time domain, both techniques find a main pulse peak with a FWHM pulse duration of 9.5 fs, and are in qualitative agreement over the shape of the pedestal caused by chromatic dispersion. The small mismatch between the two measurements can be attributed to the sensitivity of FROG measurements to the phase matching bandwidth, which for few-cycle pulses can lead to a imperfect retrieval of the optical spectrum. Indeed, the spectrum retrieved by FROG (solid blue line) doesn't quite match the spectrum measured directly with a spectrometer (solid red line) which is used as is in 2DSI. Therefore, the pulse shape obtained from 2DSI can be assumed to be more accurate in this case.

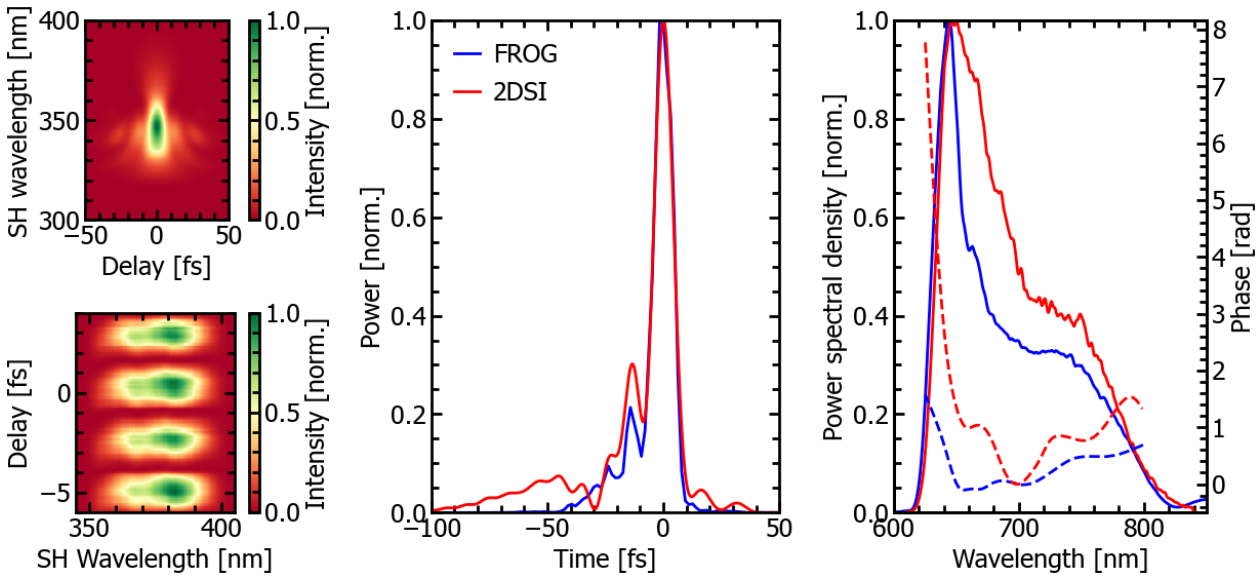

Figure 3.9 Compressed NOPA pulse shape measured via FROG (top left trace, blue curves) and 2DSI (bottom left trace, red curves). Dashed curves represent the spectral phase.

CHAPTER 4 FEW-CYCLE, SINGLE-MODE SOURCE OF BRIGHT TWIN BEAMS

This chapter first presents the technical details on the implementation of the bright twin beams (BTBs) source based on the design criteria established in section 3.3.2. Then, all results from characterization measurements performed on that source are presented, including standard characterization methods from the literature, and two novel measurements in the context of BTBs : frequency-resolved optical gating (FROG) and joint carrier-envelope phase (CEP) statistics.

4.1 Implementation

After its generation and precompression in the noncollinear optical parametric amplifier (NOPA) presented in section 3.3.3, the pump beam goes through a reflective hard-coated shortpass filter with a cut-off wavelength of 900 nm (FESH0900, Thorlabs) to remove any leak coming from the main laser system at 1030 nm. It is then focused by a silver parabolic mirror ($f = 76.2$ mm) down to a beam diameter of 40 µm inside of a 4-mm-thick beta barium borate (BBO) crystal to drive parametric down-conversion (PDC). For all experiments except for the Q function measurements presented in section 4.3, the pump energy is controlled by a continuously variable, metallic neutral density filter (NDL-25C-4, Thorlabs) offering tunability between 140 pJ and 1.4 µJ.

After generation, the pump, signal and idler are collimated either by a single silver parabolic mirror ($f = 50.8$ mm) for dispersion-sensitive measurements (FROG and Q function) or by a single plano-convex lens ($f = 25.4$ mm) for other measurements, and then the pump is separated from the BTBs using a reflective hard-coated longpass filter (LP0950 - Thorlabs).

The phase matching condition of the source can be tuned by rotating the BBO crystal in the horizontal plane. The configuration used throughout this chapter is found by first focusing the BTBs on a pair of InGaAs photodiodes and adjusting the phase matching until their photon number correlation (as measured in section 4.2.4) is maximized.

4.1.1 Focusing Geometry of the Pump

In early testing of the source, it has been observed that voluntarily introducing a small misalignment of the parabolic mirror which focuses the pump into the BBO crystal yields not only improves the parametric gain, but also increases the onset of saturation of the

PDC process. This behavior can be explained by an effective elongation of the interaction length for the PDC process and reduction of the peak pump intensity, both caused by the astigmatism induced by that misalignment.

To model this effect, consider the effective beam area $\pi w^2/2$ of a Gaussian beam with a waist w_0 at $1/e^2$ of its peak intensity and with a carrier wavelength λ_0, which is focused in the plane $z = 0$

$$\pi w^2(z)/2 = \pi w_0^2/2 \left(1 + \left(\frac{z}{z_R}\right)^2\right) \tag{4.1}$$

where $z_R = \pi w_0^2/\lambda$ is the Rayleigh length. If the same beam exhibits astigmatism such that it has two foci planes located at e.g. $z = z_R$ and $z = -z_R$, its beam area is instead

$$\begin{aligned} \pi w^2(z)/2 &= \pi w_0^2/2 \sqrt{1 + \left(\frac{z - z_R}{z_R}\right)^2} \sqrt{1 + \left(\frac{z + z_R}{z_R}\right)^2} \\ &\approx \pi w_0^2 \left(1 + \frac{z^4}{8 z_R^4}\right) + \mathcal{O}\left(z^6\right) \end{aligned} \tag{4.2}$$

where the last approximation holds remarkably well for $|z| \leq z_R$. For this implementation, with a 4-mm-thick crystal and a $\lambda_0 = 680$ nm beam initially focused down to a beam diameter $2w_0 = 40$ um, one finds that $z_R = 1.85$ mm and the approximation holds for most of the propagation in the nonlinear medium. From comparison of equations (4.1) and (4.2), it becomes clear that the astigmatic beam maintains its minimal effective beam area (and therefore its peak intensity) over a longer propagation distance. This comes at the price of a peak intensity twice as small as the original beam, but this effect can be mitigated via either a tighter focusing or an increased pulse energy.

One might wonder if similar or better results would be achieved simply from a looser focusing of the pump. Figure 4.1 therefore compares the effective beam area calculated for our parameters (blue line) to that of a aberration-free Gaussian beam with the same minimal effective beam area (red line). For the astigmatic beam, the relative variation of the peak intensity due to diffraction throughout the propagation inside the BBO crystal is reduced by a factor of 2 (14 % vs 28 %), supporting the conclusion that astigmatism helps in reducing variability of the peak pump intensity throughout the PDC process.

4.1.2 Power Scaling

With the phase-matching and pump geometry now fixed, the scaling of the photon statistics of the source with the pump energy is now investigated. Results from the measurement

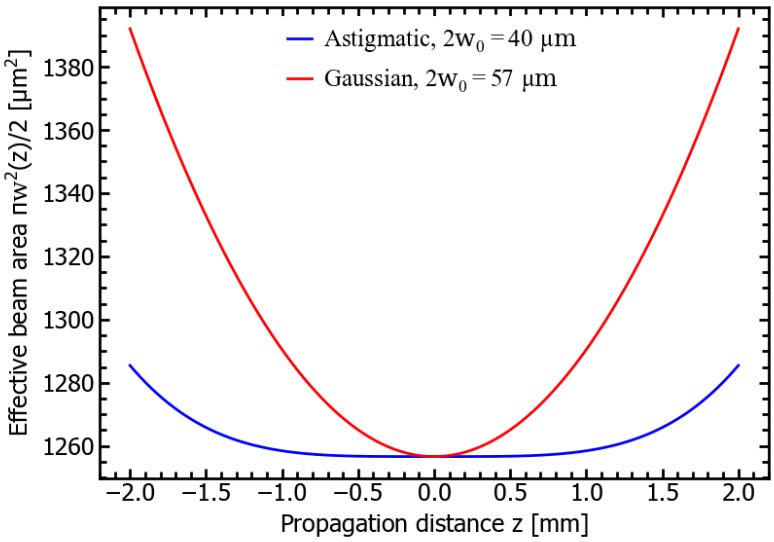

Figure 4.1 Reduction of diffraction via astigmatism.

of the average number of photons $\langle N \rangle$ and of the second-order autocorrelation function $g^{(2)}$ based on 10^6 consecutive laser pulses of one of the BTBs are presented in Figure 4.2. Vertically-aligned datapoints of $g^{(2)}$ in the plot correspond to measurements repeated with the same pump energy, but where the attenuation of the BTBs before impinging on the photodetector was adjusted to prevent the signal from saturating on the next measurement. For pump energies up to 110 nJ, the average number of photons increases exponentially with the square-root of the energy as expected in the parametric (undepleted) regime [23], while $g^{(2)}$ increases steadily toward the single-mode value $g_1^{(2)} = 2$.

Beyond this point, the parametric gain starts growing slower with the pump energy, albeit not linearly as one would expect in the regime of pump depletion [70], which is to be expected since at this point the conversion efficiency is barely 0.006 %. Instead, this saturation can be attributed to the pump experiencing a significant nonlinear phase shift from the Kerr effect during the propagation, which reduces the pump intensity by a degradation of the beam and pulse quality. The overall parametric gain is also reduced by the generation of additional Schmidt modes from self-phase modulation (SPM) [176], which can be observed by the simultaneous decrease of $g^{(2)}$ in this regime.

From these measurements, the range of pump energies from 90 nJ to 140 nJ, where $g^{(2)} > 1.9$, is identified as the operational range of the source, with 110 nJ being the ideal pump energy since it leads to a maximal value of $g^{(2)}$ and also show no signs of saturation. For the results in the following sections, the pump energy is adjusted within this range in order to

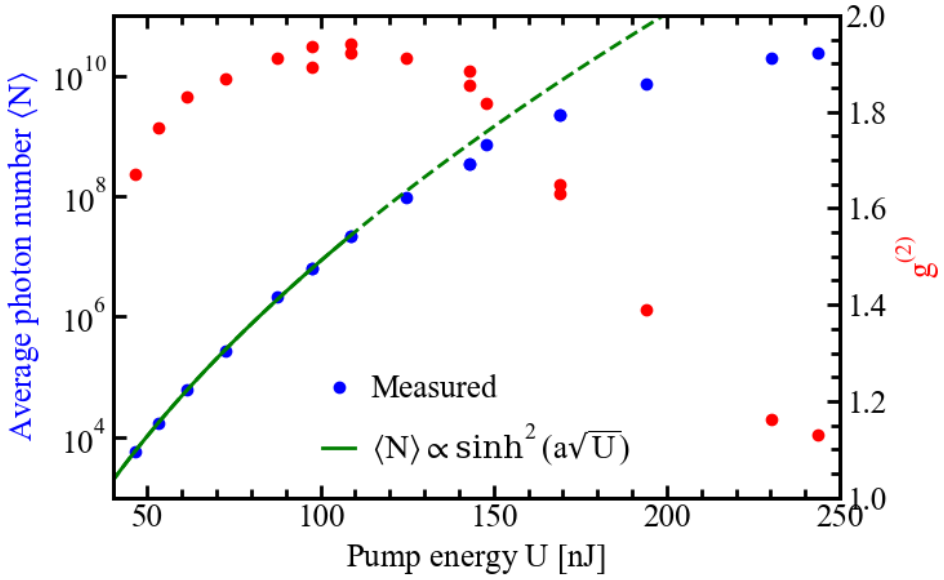

Figure 4.2 Power scaling of the source.

accommodate the dynamic range of the various instruments used. This variation in pumping can cause small quantitative inconsistencies between certain results as the exact shape and number of modes change. The minimal pulse energy of 10 pJ, identified with the design of the source in section 3.3.2, is obtained within the operational range with a 122 nJ pump. Meanwhile, the initial target energy of 86 pJ requires pushing the pump to 146 nJ, where a moderate degradation of the photon statistics ($g^{(2)} \sim 1.8$) is observed.

4.2 Characterization Results

4.2.1 Transverse Beam Shape

Figure 4.3 shows the average transverse shape of the BTBs after collimation by $f = 25.4$ mm plano-convex lens. The average is taken from 40000 single-pulse images of the beams taken with an InGaAs camera (Goldeye CL-008 SWIR TEC1, Allied Vision), with the dark noise separately measured and subtracted, and the pump energy is set to its optimal value of 110 nJ. Generation of beamlike signal (S) and idler (I) to the left and right of the pump (not visible in the figure, but observed separately) can be observed, rather than the typical conical emission of PDC.

This reshaping is the result of a combination of the high parametric gain and of the transverse Poynting-vector walkoff of the pump [24,177], which strongly favors parametric amplification of down-converted components propagating along the Poynting vector of the pump and its

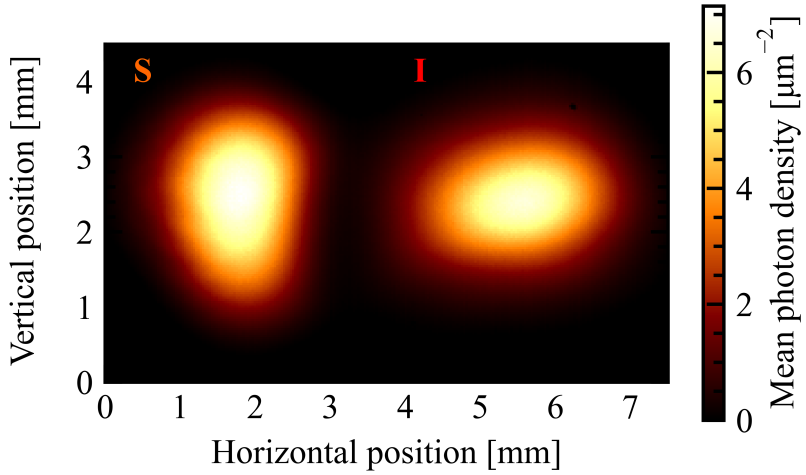

Figure 4.3 Average transverse beam shape of the bright twin beams.

.

conjugate axis in accordance with momentum conservation. The asymmetrical and elliptical shapes of the twin beams can respectively be attributed to the asymmetry in their generation conditions (as only one beam copropagates with the pump) and to the astigmatism of the pump beam.

From the 3.8 mm transverse separation of BTBs observed in this measurement, and knowing the collimation geometry, the noncollinearity angle of the twin beams with respect to the wave vector of the pump can be estimated. A geometric approximation of the propagation of the BTBs from their generation to the camera is sketched from a top-down view in Figure 4.4.

Assuming that the beams propagate nearly-symmetrically with respect to the pump, the external angular separation is approximately

$$\Delta\theta_{\text{out}} = 2\,\text{atan}\left(\frac{\Delta x}{2f}\right) \approx 8.6^\circ$$

from which the internal angular separation is estimated with Snell's law by taking the average refractive index of BBO in the InGaAs detection range $n = 1.65$ [87], yielding

$$\Delta\theta_{\text{in}} = 2\,\text{asin}\left(\frac{\sin(\Delta\theta_{\text{out}}/2)}{n}\right) \approx 5.2^\circ$$

which corresponds to an average noncollinearity angle $\alpha = 2.6^\circ$ for each beam. This result is very close to the angular Poynting-vector walkoff of the pump $\rho = 2.8^\circ$, and one may

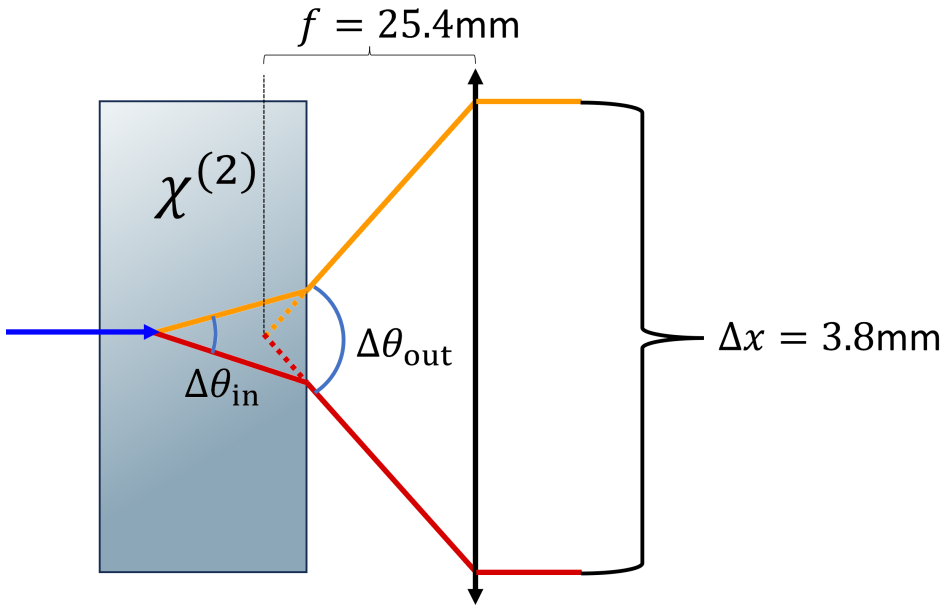

Figure 4.4 Approximate beam propagation from the PDC crystal to the camera.

therefore reasonably assume that the idler copropagates with the Poynting vector of the pump ($\alpha_i = \rho = 2.8°$), giving a noncollinearity angle for the signal beam $\alpha_s = \Delta\theta_{\text{in}} - \alpha_i = 2.4°$. In accordance with the phase matching conditions, this small asymmetry implies that the signal and idler beam have slightly different carrier frequencies, which is indeed observed from the measurement of their spectrum in section 4.2.2.

4.2.2 Spectral Statistics and Schmidt Decomposition

Figure 4.5c summarizes the spectral statistics of the source, calculated from 10000 acquisitions of the single-pulse spectrum with a pump energy of 110 nJ and measured separately for each beam. On average (solid lines), the signal (top row) and idler (bottom row) spectra are centered around wavelengths of 1215 nm and 1375 nm respectively, and support a transform-limited pulse duration of 8 and 9 fs full-width at half maximum (FWHM), corresponding to less than 2 optical cycles for both.

The small mismatch between the two pulse durations can be explained by the sharp cut-off of the response of the InGaAs sensor near 1650 nm, which truncates the measured idler spectrum more significantly than that of the signal. Large fluctuations of the photocounts (shaded area) with a standard deviation nearly equal to the average spectral density are also observed throughout the spectrum and are a direct consequence of the thermal photon statistics of the source.

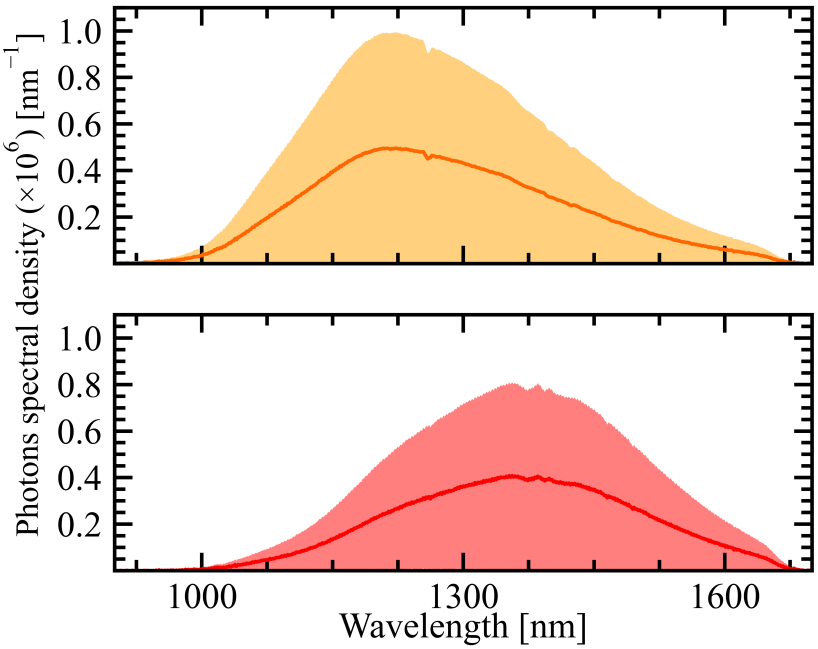

Figure 4.5 Characterization of the spatio-temporal mode structure.

Having access to the statistics of the spectrum of the BTBs enables calculation of their spectral covariance. Since the signal and idler spectra are collected separately, two "self-covariances" are obtained

$$\mathrm{COV_s}\left(N_\omega(\omega_1), N_\omega(\omega_2)\right) = \left|\sum_{l=0}^{\infty} \Lambda_l \psi_l(\omega_1)\psi_l(\omega_2)\right|^2 \tag{4.3a}$$

$$\mathrm{COV_i}\left(N_\omega(\omega_1), N_\omega(\omega_2)\right) = \left|\sum_{l=0}^{\infty} \Lambda_l \phi_l(\omega_1)\phi_l(\omega_2)\right|^2 \tag{4.3b}$$

which together should yield the same decomposition as the cross-covariance (2.56) if the joint spectral amplitude (JSA) possesses a flat phase [63]. This last assumption can be verified a posteriori by comparing the Schmidt coefficients of both decompositions to each other, and also by comparing the resulting Schmidt numbers to the one calculated from the measurement of $g^{(2)}(0)$.

The top row of Figure 4.6 presents the joint spectral intensity (JSI) obtained for the signal and the idler beams, based on the calculation of their (individual) spectral covariance using the same set of spectra as in Figure 4.5. A singular value decomposition performed on the the square-root of the two JSI yields the Schmidt modes of each beam and their corresponding

coefficients. The first two modes of each beam are respectively presented in the bottom row of Figure 4.6, while the coefficients for the first 20 modes are presented in Figure 4.7. The two decompositions yield nearly-identical coefficients for the first two modes, which account for over 99 % of the photon content of the twin beams on average, and therefore very similar quasi-single mode Schmidt numbers are obtained for both beams, i.e. $K_s = 1.04$ and $K_i = 1.05$.

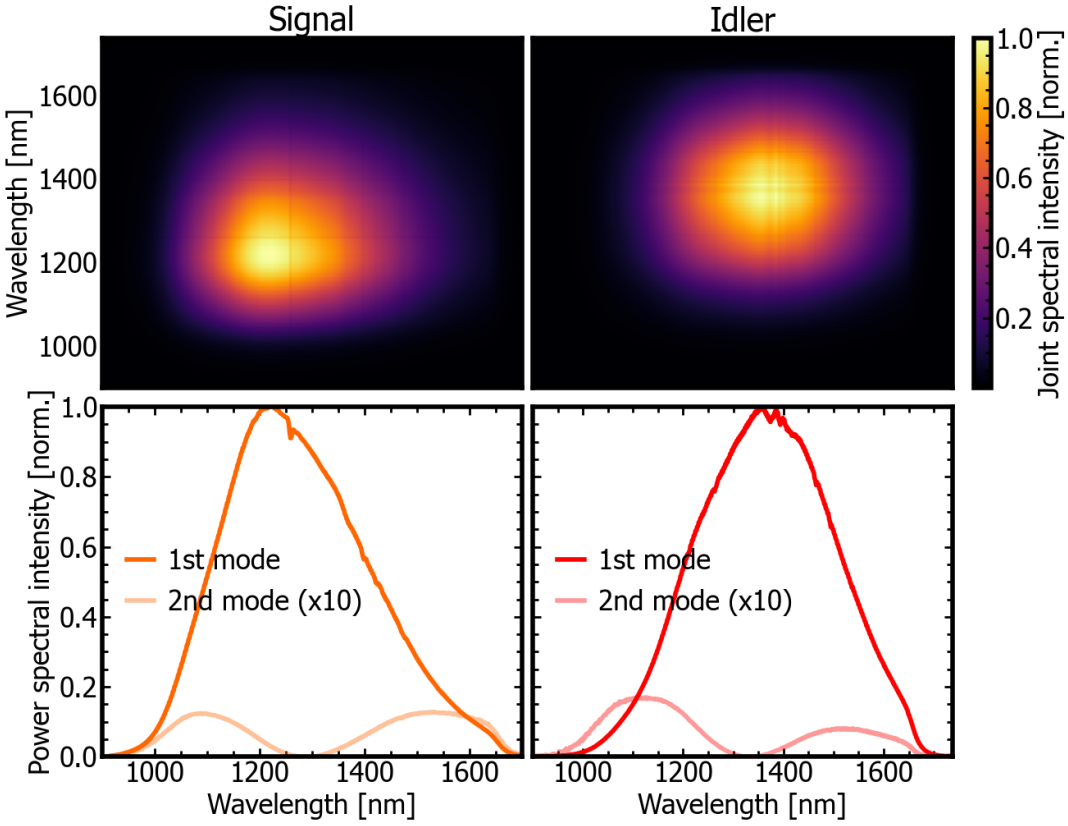

Figure 4.6 Joint spectral intensity and first two modes of the Schmidt decomposition.

The low dimensionality of the state suggests that the relative mode occupation of a given pulse could be estimated from a measurement of the power spectrum alone [42]. As a proof-of-principle implementation of this idea, Figure 4.8 presents the results from fitting the relative weights and phase of only the first two modes of the Schmidt decomposition to the measured spectral intensity on a set of 6 consecutive single-shot spectra of the signal beam which is selected for its large diversity. An excellent agreement between the measured and the fitted spectra is obtained despite the two-mode truncation. By accelerating the measurement of the spectrum via e.g. optical time-stretch [201, 202], this feature could enable shot-to-shot temporal mode sorting of the BTBs [203] toward entanglement distillation [204] by rejecting multimode events in post-selection.

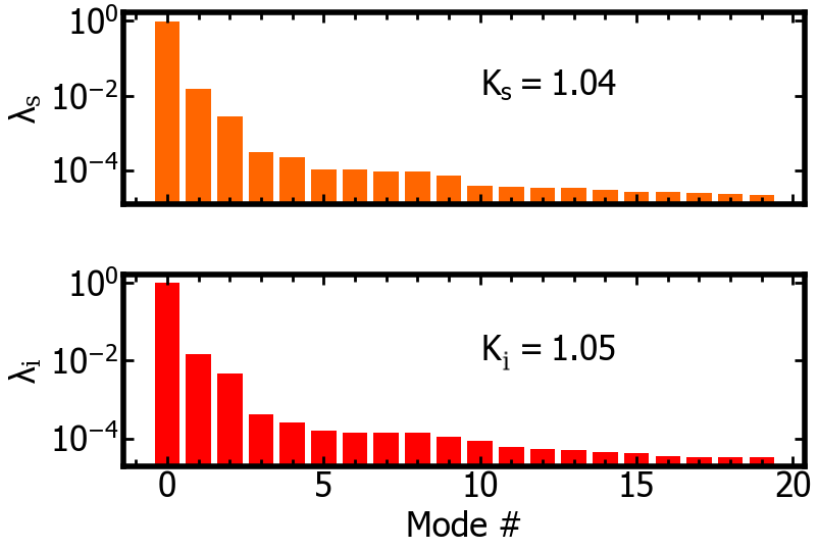

Figure 4.7 Schmidt coefficients of the spectral modes.

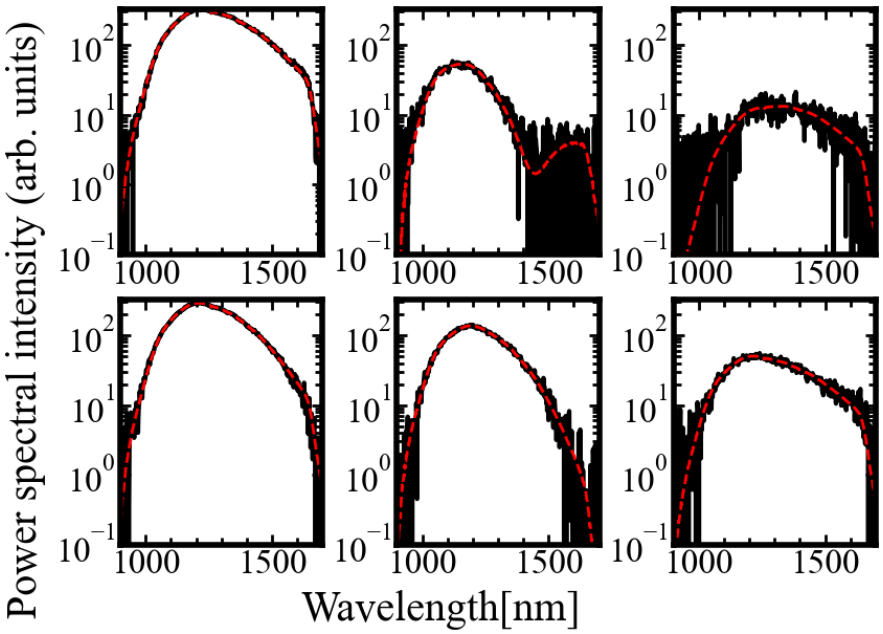

Figure 4.8 Proof-of-principle two-mode decomposition from spectral intensity measurements. The subset of 6 spectra here presented is selected for its particularly high diversity, and is not representative of the larger set.

4.2.3 Pulse Duration

Since the twin beams are generated close to the zero-dispersion wavelength of BBO [87], they are expected to be nearly-compressed after their generation. To confirm this, a second-

harmonic frequency-resolved optical gating (SH-FROG) measurement is performed on the signal beam. To obtain a sufficiently strong signal, the pump energy is here increased to 140 nJ. The measured trace, along with results from the retrieval performed with the common pulse retrieval algorithm (COPRA) [113] are presented in Fig. 4.9. The retrieved pulse indeed has a nearly-transform-limited duration of 14 fs, which corresponds to 3.4 optical cycles. The retrieved transform-limited pulse duration of 10 fs closely matches the compressed FWHM of the pump, and is slightly longer than the value calculated from the power spectrum due to the phase-matching bandwidth of the second-harmonic generation (SHG) process used in the FROG measurement. To the best of the author's knowledge, this is also the first report of a FROG measurement being performed on either BTBs or bright squeezed vacuum (BSV) [72].

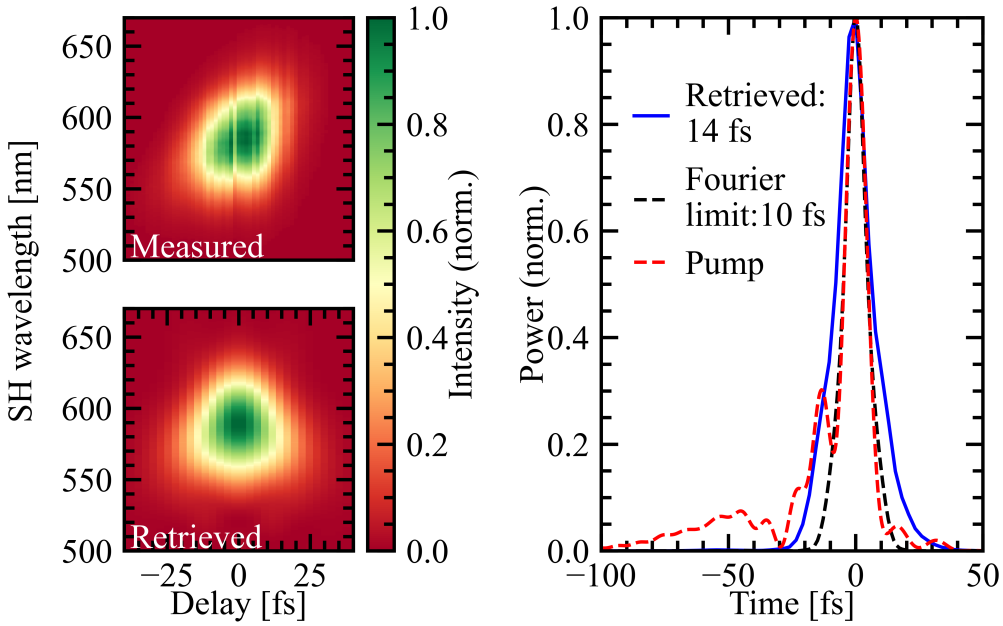

Figure 4.9 FROG measurement of the signal pulse.

The considerable mismatch between the measured and retrieved traces is a telltale sign of an unstable pulse train, and here can be attributed to the shot-to-shot changes in the pulse shape resulting from the admixture between the first and higher-order modes. Despite this, the retrieval process still typically yields the correct average pulse duration of the pulse train in these conditions [115]. The absence of a well-defined coherent artifact in the middle of the trace, which would be expected for a heavily multimode state, leads further credence to the quasi-single-mode Schmidt decomposition obtained in the spectral measurements of section 4.2.2. The pulse is also expected to be slightly shorter at its optimal parametric regime, where the occupation of higher-order modes is minimized. While no measurements were performed for the idler beam, it is expected to exhibit slightly better compression since

its carrier wavelength is even closer to the zero-dispersion wavelength of BBO.

4.2.4 Photon Statistics

Next are the photon statistics of the BTBs, which are measured using a pair of amplified high-efficiency InGaAs photodiodes connected to a digital time-gated integrator synchronized to the seed laser. To avoid saturation of the digital integrator, the pump energy is lowered to 92 nJ. Here, the integrated voltages are converted to a number of photons by normalizing their mean (58.8 mV) to the average photon flux measured with a power meter (3.5×10^{11} photons/s at a 99 386 Hz repetition rate with a central wavelength of 1300 nm), yielding a conversion factor of 59500 photons/mV. An example of the resulting two-channel photon number readout is plotted in Figure 4.10, where the large shot-to-shot fluctuations expected for a single-mode source can be observed.

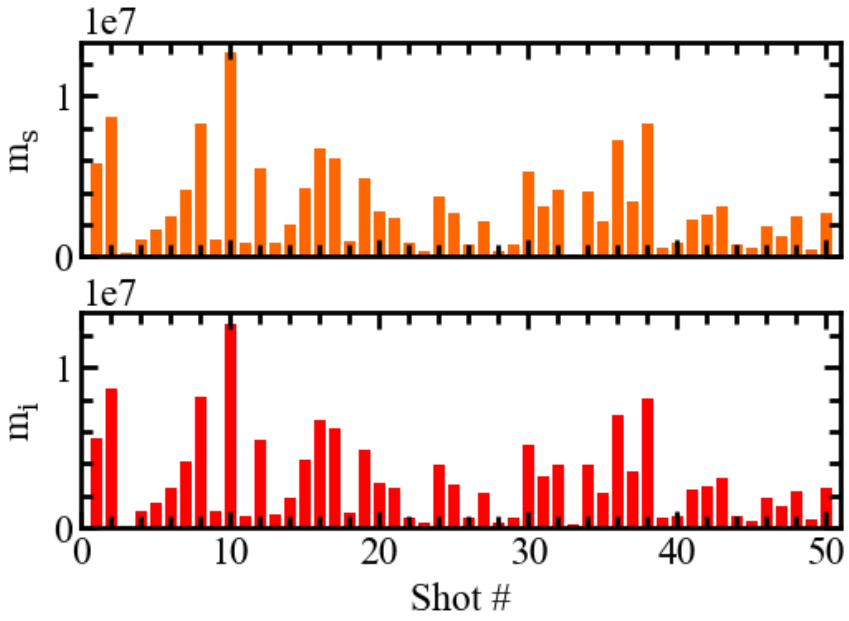

Figure 4.10 50 consecutive and simultaneous readouts of the photons number of the BTBs.

The histograms resulting from over 5.9×10^6 consecutive shots recorded over 1 min are presented in Fig. 4.11. The length of the joint distribution (top right plot) along the diagonal direction is indicative of the fluctuations of the total number of photons measured for both beams $m_+ = m_\mathrm{s} + m_\mathrm{i}$, while its width along the anti-diagonal direction instead represents the fluctuations of the measured photon number difference $m_- = m_\mathrm{s} - m_\mathrm{i}$, and where $m_{(s,i)}$ is the measured number of photons in the signal (s) or idler (i) mode. The sharp and elongated shape of the distribution is a direct visual consequence of the PDC process which imposes

that all down-converted photons are produced in pair.

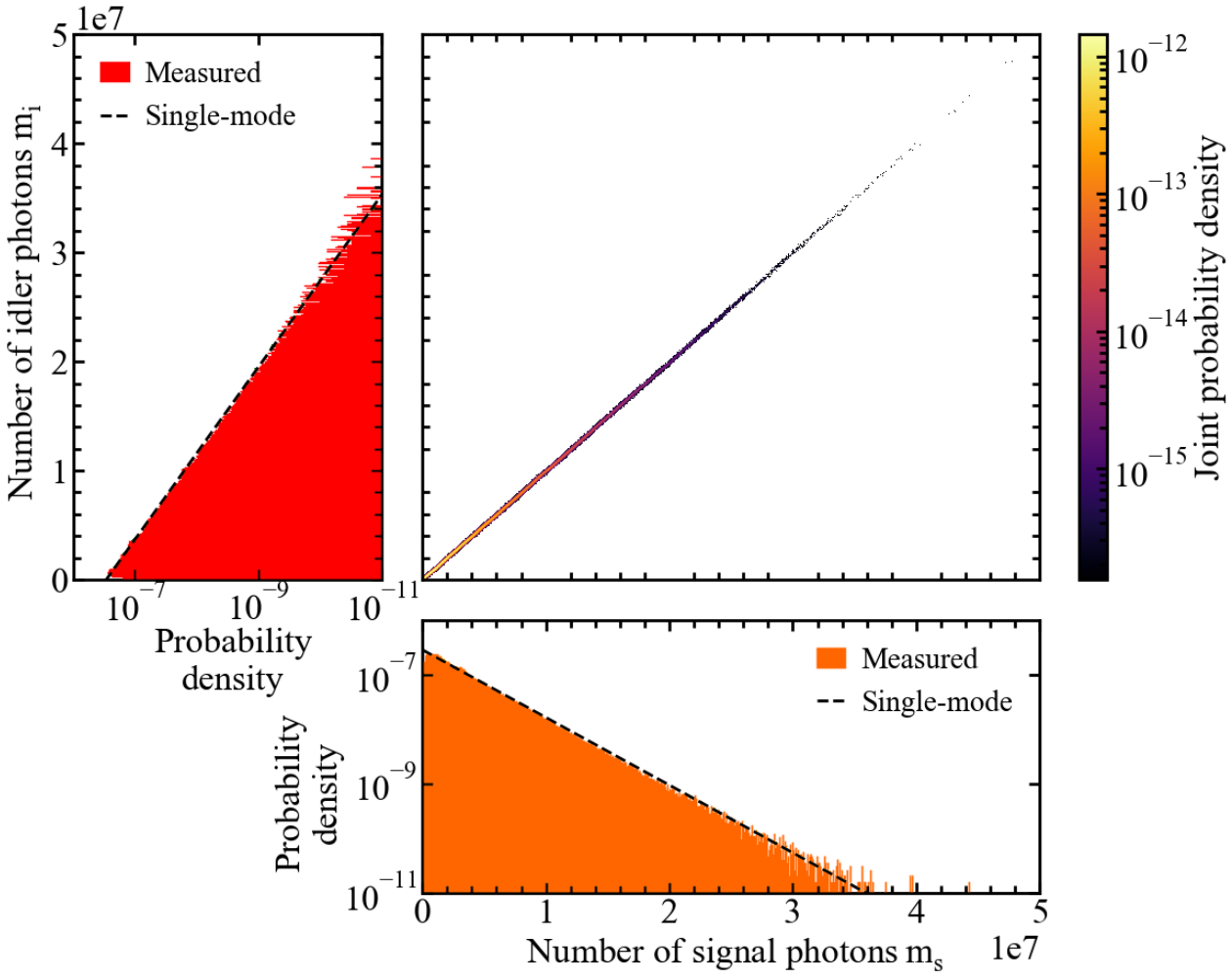

Figure 4.11 Joint (top right plot) and marginal (left and bottom plots) photon probability distributions.

Turning to the marginal distributions (bottom right for the signal, top left for the idler), an average photon content $\langle m_{\mathrm{s}} \rangle = 3.50 \times 10^6$ and $\langle m_{\mathrm{i}} \rangle = 3.43 \times 10^6$ per pulse is observed for the signal and the idler respectively. The measured number of photons $\hat{m}$ are related to the photon number of the light source $\hat{n}$ via the standard beamsplitter transformation [164], such that its first two statistical moments are

$$\left\langle m_{(\mathrm{s,i})} \right\rangle = \eta_{(\mathrm{s,i})} \left\langle n_{(\mathrm{s,i})} \right\rangle \tag{4.4}$$

$$\Delta^2 \left(m_{(\mathrm{s,i})} \right) = \eta_{(s,i)}^2 \Delta^2 \left(n_{(\mathrm{s,i})} \right) + \eta_{(\mathrm{s,i})} (1 - \eta_{(\mathrm{s,i})}) \left\langle n_{(\mathrm{s,i})} \right\rangle \tag{4.5}$$

where $\eta_{(s,i)}$ is the total quantum efficiency for the detection of the signal or the idler photons. The difference between $\langle m_\mathrm{s} \rangle$ and $\langle m_\mathrm{i} \rangle$ can therefore be attributed to the slight mismatch between the detection efficiency of each beam on an InGaAs sensor first observed in the spectrum measurements of section 4.2.2. Similarly, the measured values of the second-order auto-correlation functions of each beam

$$g_\mathrm{s}^{(2)} \approx \frac{\langle m_\mathrm{s}^2 \rangle}{\langle m_\mathrm{s} \rangle^2} = 1.924$$
$$g_\mathrm{i}^{(2)} \approx \frac{\langle m_\mathrm{i}^2 \rangle}{\langle m_\mathrm{i} \rangle^2} = 1.951$$

are slightly mismatched due to the truncation of the idler spectrum effectively acting as a frequency mode filter. Nonetheless, the two values are close to the single-mode limit $g_\mathrm{thermal}^{(2)} = 2$, which explains the near-perfect fit of the two marginal distributions to the fitted thermal photon statistics. The corresponding effective number of spatio-temporal Schmidt modes

$$K_\mathrm{s} \approx (g_\mathrm{s}^{(2)} - 1)^{-1} = 1.082$$
$$K_\mathrm{i} \approx (g_\mathrm{i}^{(2)} - 1)^{-1} = 1.051 \ .$$

The slightly higher values of K observed here in comparison to the ones obtained from the Schmidt decomposition in section 4.2.2 can be attributed to the fact that the present measurement is also sensitive to spatial (transverse) modes of the BTBs which are traced out in the JSI measurement. Taking the value found for the signal due to its spectrum being detected more efficiently, and assuming separability of spatial and temporal modes [143]

$$K = K_\mathrm{space} K_\mathrm{time} \ , \tag{4.6}$$

this implies that the BTBs effectively occupy $K_\mathrm{space} = K_\mathrm{s}/K_\mathrm{time,s} = 1.04$ spatial modes.

4.2.5 Noise Reduction Factor

In an attempt to demonstrate nonclassicality of the generated BTBs, the noise reduction factor (NRF) is calculated from the joint photon statistics presented in section 4.2.4. The separately-measured dark noise is first deconvolved from the total measured photon number

difference noise, as shown in Figure 4.12. After deconvolution, the standard deviation of the photon-number difference $\Delta n_- = 35\,400$ photons, which corresponds to

$$\mathrm{NRF} = 181$$

where the second definition (2.61) was used. This corresponds to a root-mean square noise 13.5 times higher than the shot noise level $\sqrt{\langle m_+ \rangle} = 2640$ photons.

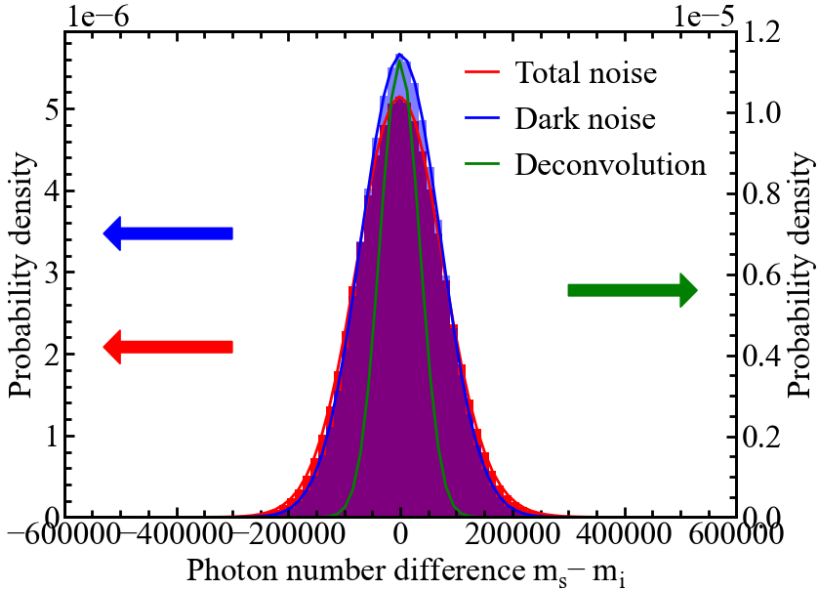

Figure 4.12 Measured photon number difference statistics. All three histograms follow a Gaussian distribution.

While a quantum advantage is not demonstrated here, getting this close to the shot noise limit with these experimental conditions still demonstrate a very high level of photon-number correlations. For comparison, sub-unity values of the NRF have been reported for source of BTBs with comparable average photon number per pulse [68, 75], but only in the heavily multimode ($K > 500$) where the noise stemming from mismatched detection efficiencies and the required dynamic range for the detectors are both reduced by a factor $\sqrt{K}$ [23]. Furthermore, the relative stability of the source $\Delta m_- / \langle n_+ \rangle = 0.5\,\%$ is comparable to the long-term pulse-to-pulse energy stability of the driving laser system (see specifications in table 3.1).

Technical Limits on the Measurement of the Noise Reduction Factor in the High-Gain, Nearly-Single-Mode Regime

To demonstrate the challenges involved in measuring low values of the NRF in the high-gain, nearly-single-mode regime, first consider a purely single-mode source of BTBs. Using its standard definition (2.60), the NRF is

$$\mathrm{NRF} = \frac{(\eta_\mathrm{s} - \eta_\mathrm{i})^2 \Delta^2 n + (\eta_\mathrm{s} - \eta_\mathrm{s}^2 + \eta_\mathrm{i} - \eta_\mathrm{i}^2)\,\langle n \rangle}{(\eta_\mathrm{s} + \eta_\mathrm{i})\,\langle n \rangle} \tag{4.7}$$

where $\langle n \rangle = \langle n_\mathrm{s} \rangle = \langle n_\mathrm{i} \rangle$ is the average number of photons generated in either the signal or idler beam, and $\Delta^2 n = \Delta^2 n_s = \Delta^2 n_i$ is its variance. The first term of the numerator corresponds to an increase of the NRF from mismatched detection efficiency between the two beams, while the second term corresponds to addition of quantum noise from losses. The first term highlights the fact that experimentally measuring NRF < 1 is harder in the high gain regime, since for twin beams $\Delta^2 n \approx \langle n \rangle^2$. Using the alternative definition (2.61), the NRF is only bounded by the detection efficiencies

$$\mathrm{NRF} = \frac{\eta_\mathrm{s} - \eta_\mathrm{s}^2 + \beta^2(\eta_\mathrm{i} - \eta_\mathrm{i}^2)}{(\eta_\mathrm{s} + \beta\eta_\mathrm{i})} = \frac{1 + \eta_\mathrm{s}/\eta_\mathrm{i}}{2} - \eta_\mathrm{s}\ , \tag{4.8}$$

but this definition introduces an asymmetry between the signal and idler such that the NRF will have a lower value if $\eta_\mathrm{s} < \eta_\mathrm{i}$ than if $\eta_\mathrm{s} > \eta_\mathrm{i}$. To illustrate this, equation (4.8) is plotted in Figure 4.13. This asymmetry is a typical result for heralded photon sources [205], and should be interpreted as meaning that whichever beam is detected with the highest quantum efficiency (here assumed to be the idler) would work best as an herald to reshape the photon statistics of its twin in a post-selection scheme [17, 19, 21, 32], rather than the other way around. In practice, the subscripts s and i can be exchanged freely in equation (4.8) and the nonclassicality condition NRF < 1 can be achieved for arbitrary detection efficiencies.

Setting the results of this first analysis as a reference point, we can now consider how the presence of a weakly-excited, potentially unbalanced second spatio-temporal mode in the detection affects equation (2.61). The relative photon number occupation of mode l is

$$\Lambda_l = \frac{\langle n_l \rangle}{\langle N \rangle} \tag{4.9}$$

where $\langle N \rangle = \sum_l \langle n_l \rangle$ is the mean total number of photons. To highlight the effects of the second mode, we assume a nearly single mode source ($\lambda_1 \gg \lambda_2$, $\lambda_{3+} = 0$) where the photons in the first mode are detected with 100% quantum efficiency, yielding $\beta \approx 1$. In this scenario,

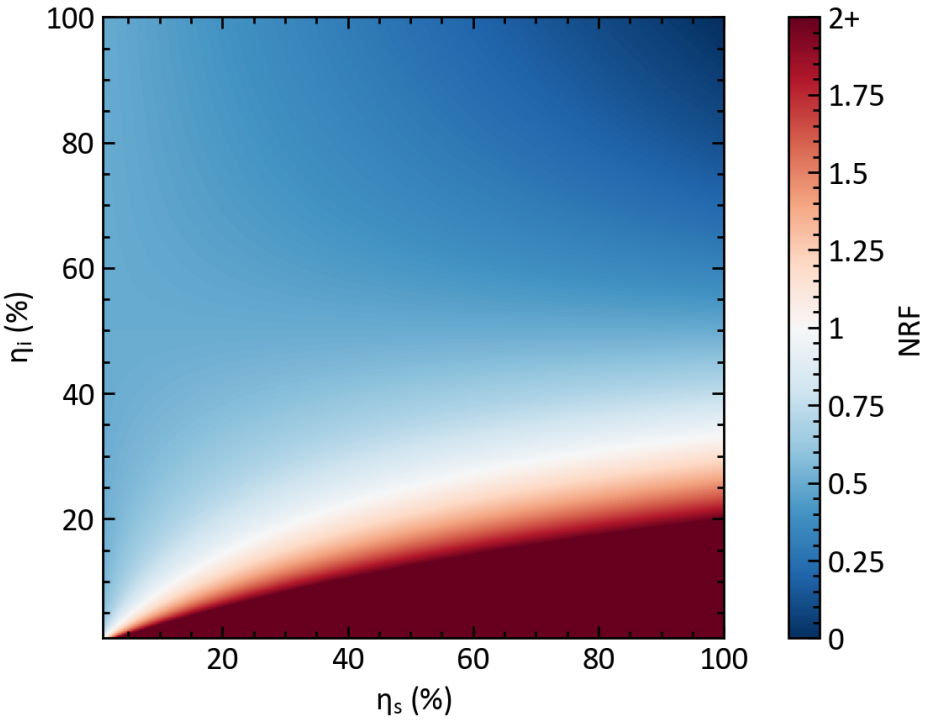

Figure 4.13 Noise reduction factor for single-mode twin beams.

the NRF is dictated solely by the detection efficiencies η_s and η_i of the second mode

$$\mathrm{NRF} = \frac{(\eta_s - \eta_i)^2 \Delta^2 n_2 + (\eta_s - \eta_s^2 + \eta_i - \eta_i^2) \langle n_2 \rangle}{2 \langle n_1 \rangle + (\eta_s + \eta_i) \langle n_2 \rangle} \tag{4.10}$$

and now the first term of the numerator cannot be canceled without unbalancing the losses of the first mode, unless some efficient form of mode filtering (e.g. a quantum pulse gate [62]) is available. Therefore, in the high gain regime where $\Delta^2 n_2 \approx \langle n_2 \rangle^2 \gg \langle n_2 \rangle$, the NRF will be dominated by the unbalanced detection of that second mode. Considering only the contribution from this first term and the maximum value of the denominator, we find a minimum value for the NRF

$$\mathrm{NRF} > \frac{(\eta_s - \eta_i)^2 \langle n_2 \rangle^2}{2 \langle N \rangle} \tag{4.11}$$

from which a maximum tolerance on the balancing $\Delta\eta = |\eta_s - \eta_i|$ of the losses in the second mode is derived by applying the condition NRF < 1, resulting in

$$\Delta\eta < \frac{\sqrt{2}}{\Lambda_2\sqrt{\langle N\rangle}} \tag{4.12}$$

showing that the NRF becomes more sensitive to the presence of a second mode as the parametric gain increases. Equation (4.12) is plotted in Figure 4.14 for arbitrary admixtures of two spatio-temporal modes. For the conditions of the experiment

$$\langle N\rangle = \frac{\langle m_{\rm s}\rangle}{\eta_{\rm s}} = \frac{\langle m_{\rm i}\rangle}{\eta_{\rm i}} \approx 4.2\times 10^6$$
$$\lambda_2 \approx \frac{K-1}{2} = 0.04$$

one finds a tolerance $|\Delta\eta| < 1.7\%$. Ideally, one would design a source where the tolerance $\Delta\eta \geq 1$, such that any potential unbalancing of the second mode does not prevent measurement of nonclassical values of the NRF. Near the single mode limit $K-1 \ll 1$, this condition is achieved if

$$K \leq 1 + \frac{4}{\sqrt{\langle N\rangle}} \tag{4.13}$$

again showing the increasing difficulty of measuring nonclassicality at higher values of the parametric gain. Equation (4.13) is plotted in Figure 4.15. For $\langle N\rangle \approx 4.2\times 10^6$, we find $K \leq 1.002$.

4.3 Carrier-Envelope Phase Correlations and Q function

As presented in Chapter 2, driving of extreme nonlinear phenomena with few-cycle pulse requires control over the CEP [46, 47, 49]. Each excited modes of the signal (s) and idler (i) BTBs are known to have a completely random phase ϕ individually, and yet be phase-locked to the pump (p) with a correlation which is centered around the classical relation [206–208]

$$\phi_{\rm s} + \phi_{\rm i} - \phi_{\rm p} = \text{const.} \tag{4.14}$$

and which improves with the squeezing parameter r (or equivalently the parametric gain G). This phase relationship has been observed for a single pair of narrowband modes in a heterodyne or multi-port homodyne detection schemes [150–153, 209], but not for few-cycle

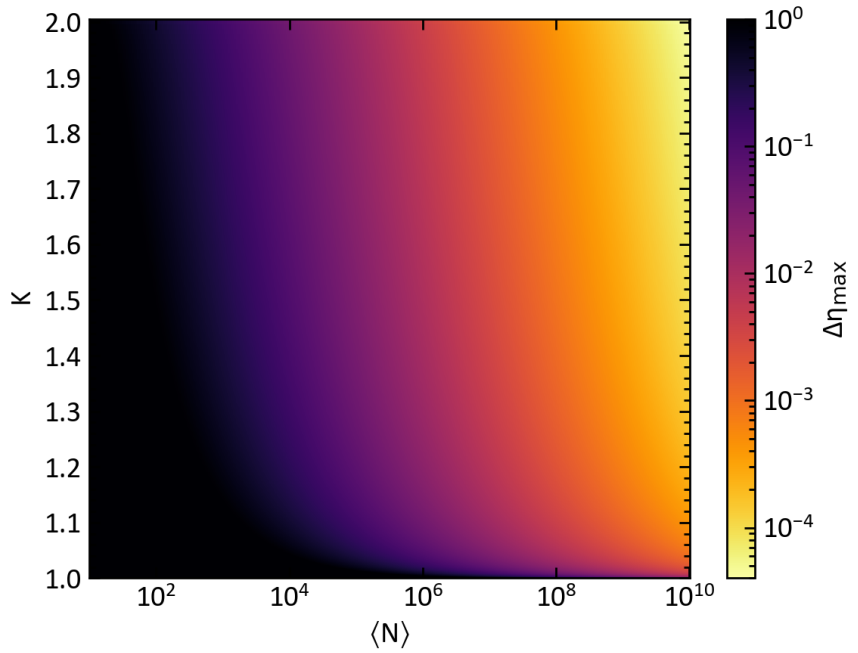

Figure 4.14 Maximum loss unbalance for the second mode for sub-2 modes twin beams.

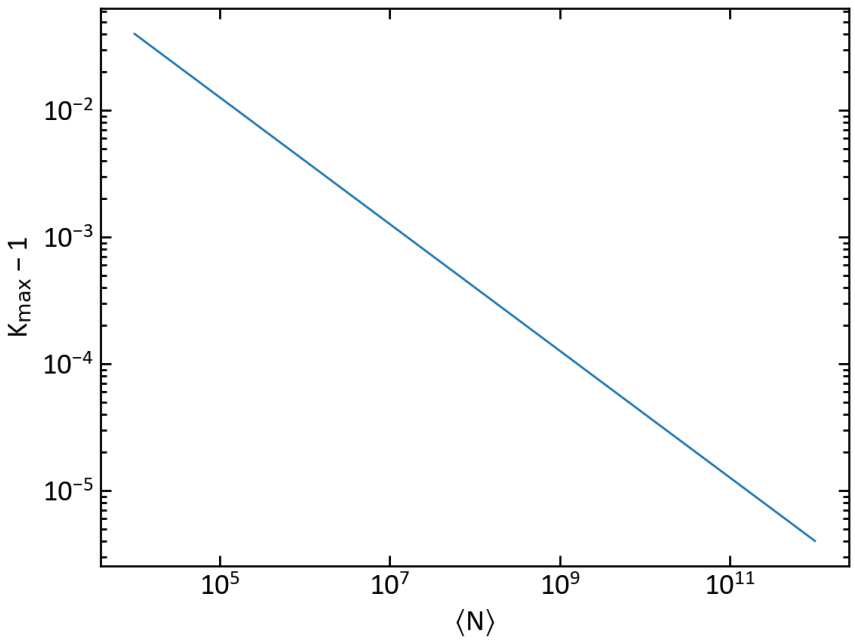

Figure 4.15 Maximum effective number of spatio-temporal modes K to reach NRF < 1 with a completely unbalanced ($\Delta\eta = 1$) second mode.

modes where this phase now amounts to the CEP of the twin pulses.

In this section, a proof-of-principle implementation of an alternative technique based on

standard f-to-2f interferometry [45] is demonstrated, where the BTBs are upconverted via SHG and sum frequency generation (SFG) to spectrally overlap with the pump, which is temporally-delayed to generate interference patterns in the frequency domain. Measurement of the spectral fringes on a single-shot basis allows for the simultaneous measurement of 3 phase differences

$$\theta_{\mathrm{SH,s}} = 2\phi_{\mathrm{s}} - \phi_{\mathrm{p}} \tag{4.15a}$$

$$\theta_{\mathrm{SF}} = \phi_{\mathrm{s}} + \phi_{\mathrm{i}} - \phi_{\mathrm{p}} \tag{4.15b}$$

$$\theta_{\mathrm{SH,i}} = 2\phi_{\mathrm{i}} - \phi_{\mathrm{p}} \tag{4.15c}$$

and 3 amplitudes

$$A_{\mathrm{SH,s}} \propto A_{\mathrm{s}}^2 \tag{4.16a}$$

$$A_{\mathrm{SF}} \propto A_{\mathrm{s}} A_{\mathrm{i}} \tag{4.16b}$$

$$A_{\mathrm{SH,i}} \propto A_{\mathrm{i}}^2 \tag{4.16c}$$

which we use to 1) observe the phase correlations between the signal and idler, 2) measure the individual and joint Q functions of the second harmonic (SH) of the signal and the idler, and 3) demonstrate the capability to implement post-selection schemes bases on both the amplitude and the phase of BTBs. This scheme is enabled by the fact that the twin beams here generated are nearly-single-mode, broadband and intense.

4.3.1 Implementation

The schematic of the experiment is presented in Fig. 4.16. From the 1.4 µJ pulse train generated in the NOPA, about 10% of the pulse energy is picked off from the reflection of a beam sampler (BSF10-B - Thorlabs) and serves as the PDC pump. The reminder of the energy is used to sequentially drive supercontinuum generation (SCG) in a 2-mm-thick calcium fluoride window and SHG in a 10-µm-thick BBO crystal, producing a f-to-$2f$ interferometric signal on the spectrometer at ultraviolet (UV) wavelengths that gives access to the CEP of the pump/local oscillator (LO) for the experiment.

After generation of the BTBs, the pump, signal and idler are collimated by a single silver parabolic mirror ($f = 50.8$ mm), then the pump is split using a reflective hard-coated longpass

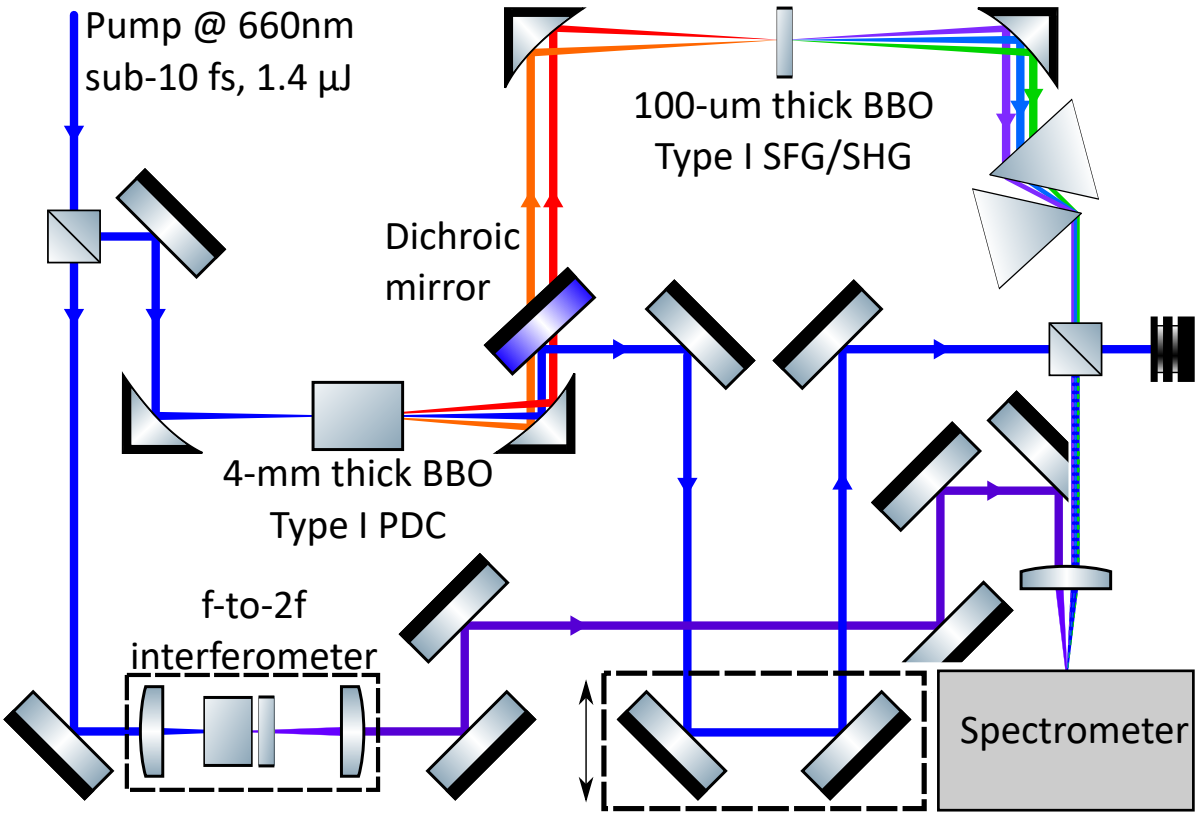

Figure 4.16 Detailed schematic of the experiment.

filter (LP0950 - Thorlabs). The signal and the idler are refocused into a 100 µm thick BBO crystal by a silver parabolic mirror (f = 76.2 mm) to drive SHG and SFG. The SH and sum frequency (SF) beams are collimated by another silver parabolic mirror (f = 50.8 mm) and then sent trough a pair of dispersing SF11 prisms. The separation of the prisms is adjusted such that all three beams (SH of the signal, SH of the idler, and their SF) overlap spatially. The upconverted beams are then mixed linearly with a small fraction of the pump (which serves as the LO) via a beam sampler (BSF10-C - Thorlabs) which here acts as a low-reflectance beamsplitter.

The combined beams are finally focused on the slit on a Si-based spectrometer (HR2000+ - Ocean Insight), together with the UV light from the f-to-2f interferometer. The pulse picking frequency of the driving laser is lowered to 994 Hz and the integration time of the spectrometer is set to 1 ms. As such, at most one laser shot is registered by the spectrometer per recording. Recorded spectra containing no laser light (about 0.6% of the raw dataset) are then identified in post-treatment by tracking the integrated optical power and are discarded. A total of 500000 spectra are acquired as 5 sets of 100000 spectra over 30 minutes, for an average acquisition rate of 278 Hz.

Amplitude and Phase Extraction

All collected spectra are first interpolated to a grid of constant frequency spacing. Then, for each upconverted beam (signal SH, idler SH, and their SF), an hyper-Gaussian window is used to isolate the spectral region in the LO spectrum where the interference fringes are located. A high-pass filter is then applied to the windowed spectra to isolate the interference fringes from the DC background. A single-shot example of the resulting interferometric signal (left in wavelength space for clarity) is presented in Figure 4.17.

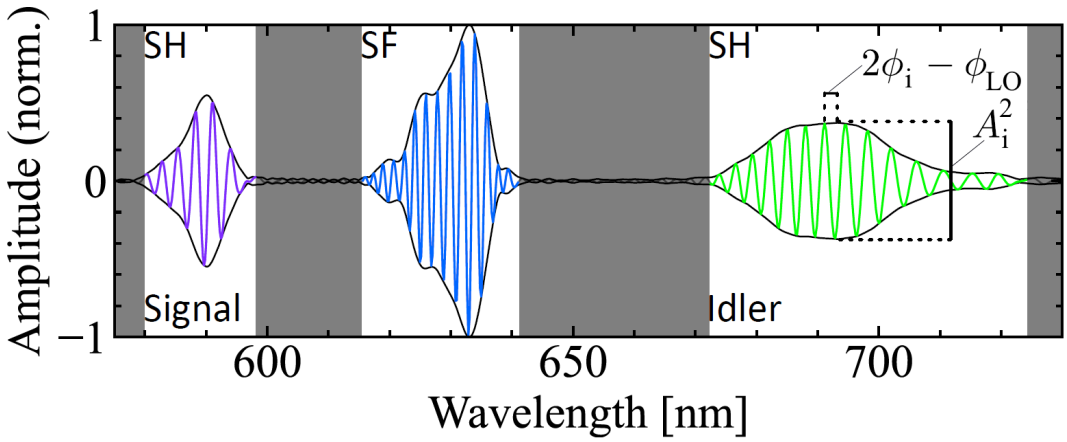

Figure 4.17 Example of a single-shot interferometric signal on the spectrometer, after digital removal of the DC background. The fringe phase is equal to the phase differences (4.15), while the peak-to-peak amplitude of the fringes is proportional to the amplitude of the nonlinear signals (4.16).

From this dataset, the single-shot spectrum where the fringes have the highest peak-to-peak amplitude is selected as a reference signal $R(\omega)$. All spectra $S_l(\omega)$ are then compared to the reference to extract their in-phase $x_l = \mathrm{Re}(R \cdot S_l)$ and out-of-phase $p_l = \mathrm{Im}(R \cdot S_l)$ components with respect to the reference, where $\cdot$ denotes the scalar product. Finally, the measured distributions of x and p for the two SHs are rescaled by a constant factor to yield the correct average number of photons of each beam as measured on the sensor of the spectrometer $\left\langle m_{(\mathrm{s,i})} \right\rangle = \left\langle x_{(\mathrm{s,i})}^2 + p_{(\mathrm{s,i})}^2 - 1 \right\rangle$, which are measured separately in the absence of the LO to be $\langle m_{\mathrm{s}} \rangle = 4900$ and $\langle m_{\mathrm{i}} \rangle = 7400$ photons per pulse. For brevity, here and going forward in this section the subscripts s and i are used to denote the SH of the signal and idler beams, rather than their fundamentals.

Over the 30-minute total measurement interval, the phase of the interferometer slowly drifts due to temperature variations in the lab. This drift is tracked using the SF beam, which is phase-locked to the LO but copropagates with the two SH beams. The phase fluctuation

between the SF and the LO is shown in the top plot of Figure 4.18, and the corresponding spectral noise density is presented for the 1st dataset as an example in Figure 4.19, where the drift appears as $1/f$ noise at frequencies below 2 Hz. For each of the 5 datasets, a digital high-pass filter is applied to remove this classical noise, yielding the phase distribution in the bottom plot of Figure 4.18.

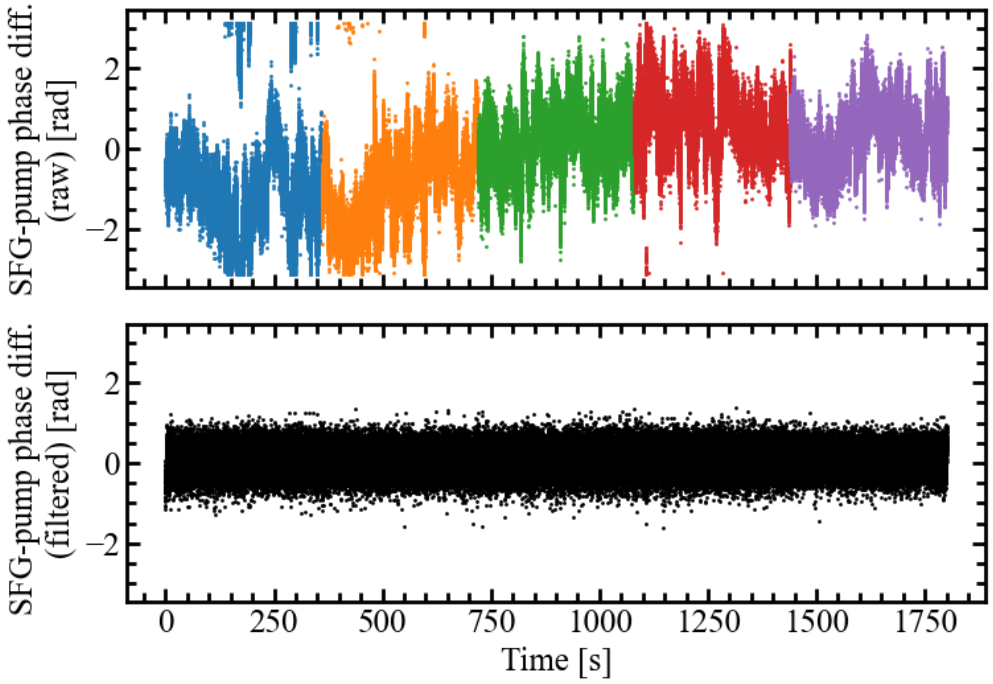

Figure 4.18 Long-term drift of the phase of the interferometer, measured from the interference of SF beam with the LO.

4.3.2 CEP Anti-Correlation

We first look at the joint probability distribution of the CEP of the BTBs, which is plotted in Figure 4.20a. The anti-correlation relation (4.14) visually appears from the high concentration of measured events around the anti-diagonal line, while the uniform spread of the distribution over 2π in the orthogonal direction highlights the full indetermination of the individual CEPs. To highlight the importance of the pump/LO in this measurement, its CEP is digitally added to the measured fringe phase, resulting in the histogram presented in Figure 4.20b. The resulting white noise pattern visually demonstrate that by themselves and in the absence of a CEP-stable pump, the twin beams exhibit completely random and uncorrelated CEPs.

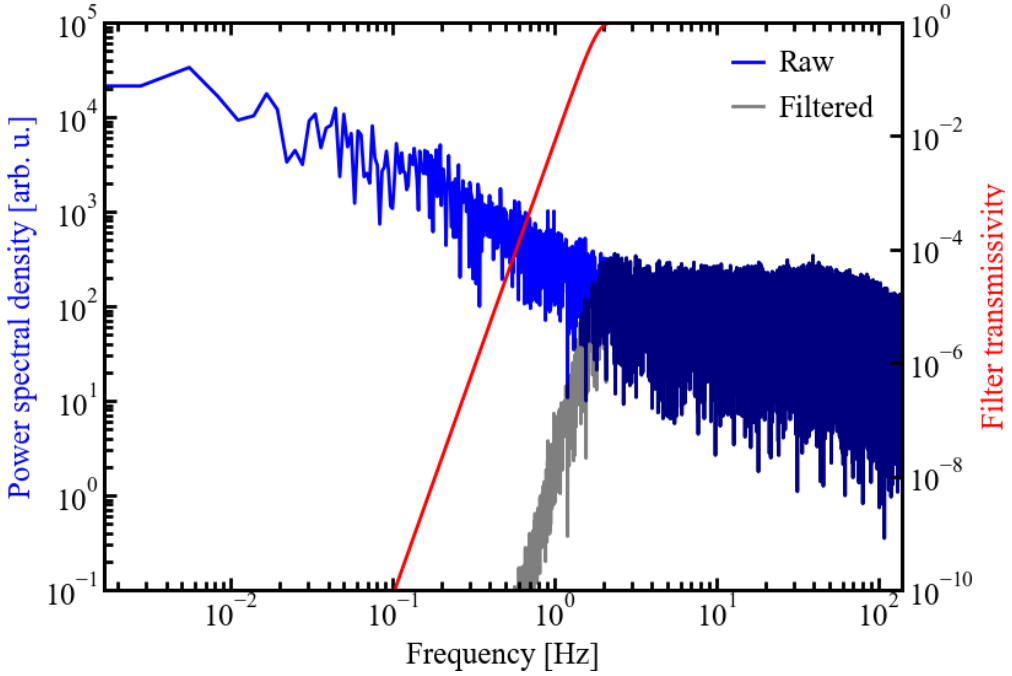

Figure 4.19 Spectral noise density of the phase of the interferometer for the 1st (blue) dataset of Figure 4.18.

From this measurement, the standard deviation of the CEP sum is found to be

$$\Delta\left(2\phi^{\mathrm{S}} + 2\phi^{\mathrm{I}} - 2\phi^{\mathrm{P}}\right) = 730 \text{ mrad}$$

where the factor of 2 comes from the SHG process. While this value is relatively large, it is largely dominated by the dark noise of the measurement, as demonstrated in the following analysis.

The measurement apparatus effectively implements a frequency-domain equivalent to heterodyne detection [154]. Instead of detecting both quadratures of a narrowband field at frequency ω_0 via a LO at a detuned frequency $\omega_0 + \delta\omega$, the present setup detects a pulsed field at group delay τ_{g} via a LO at a delayed group delay $\tau_{\mathrm{g}} + \delta\tau_{\mathrm{g}}$. In both cases, the detection is also sensitive to the quadratures of an image mode with the opposite detuning with respect to the LO ($\omega_0 + 2\delta\omega$ for heterodyning, here $\tau_{\mathrm{g}} + 2\delta\tau_{\mathrm{g}}$). When the image is in the vacuum state, the detection setup effectievly implements the same measurement as an 8-port homodyne detector [151]. The measured quadratures $\hat{x}_m$ and $\hat{p}_m$ are therefore related to the intrinsic quadratures $\hat{x}$ and $\hat{p}$ of the input state by

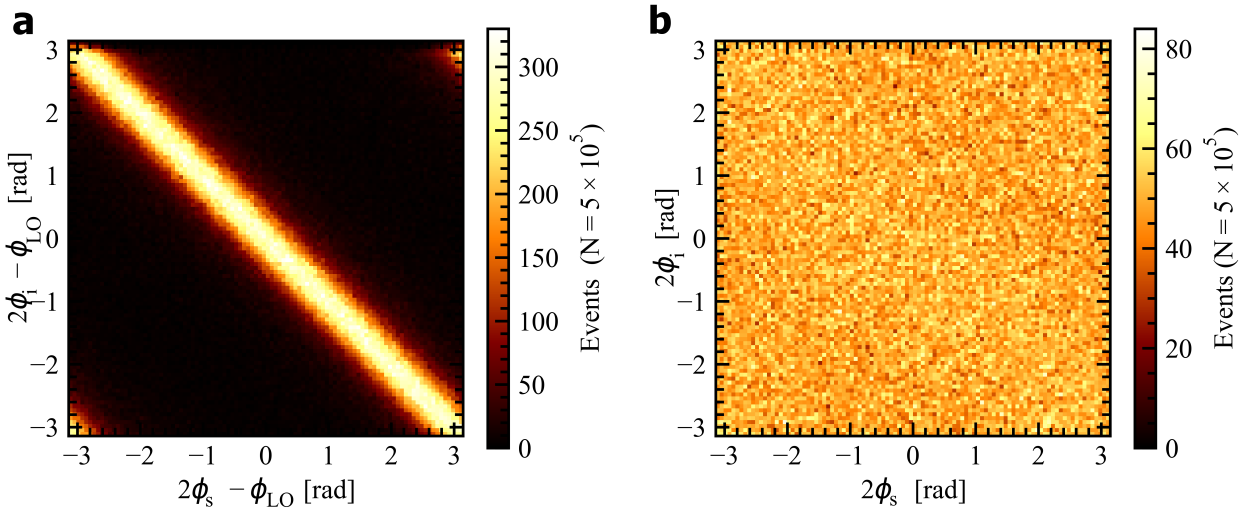

Figure 4.20 CEP correlation measurements.

$$\hat{x}_m = \sqrt{\eta}\hat{x} + \sqrt{2-\eta}\hat{x}_0 + \delta_x \tag{4.17a}$$

$$\hat{p}_m = \sqrt{\eta}\hat{p} - \sqrt{2-\eta}\hat{p}_0 + \delta_p \tag{4.17b}$$

where $\hat{x}_0$ and $\hat{p}_0$ are the quadratures of the vacuum added by both the image mode and the detection losses, η is the overall quantum efficiency of the detection scheme, and δ_x and δ_p are classical stochastic variables modeling technical noise. In the ideal case $\eta = 1$ and $\delta_x = \delta_p = 0$, the simultaneous measurement of $\hat{x}_m$ and $\hat{p}_m$ yields exactly the Q function of the input state [152], while any other case instead yields a smoothed version of the distribution.

The impact of vacuum and technical noise on the measured quadratures is experimentally characterized by measuring the statistics of the two quadratures $\hat{x}_m$ and $\hat{p}_m$ under dark conditions, i.e. when the input state is the vacuum. In this scenario, knowing that the first two statistical moments of the quadratures for the vacuum state are $\langle x_0 \rangle = 0$ and $\langle x_0^2 \rangle = 1/4$, those of the measured quadratures are

$$\langle 0 | \hat{x}_m | 0 \rangle = \langle \delta_x \rangle \tag{4.18a}$$

$$\langle 0 | \hat{p}_m | 0 \rangle = \langle \delta_p \rangle \tag{4.18b}$$

$$\langle 0|\, \hat{x}_m^2\, |0\rangle = \frac{1}{2} + \left\langle \delta_x^2 \right\rangle \tag{4.19a}$$

$$\langle 0|\, \hat{p}_m^2\, |0\rangle = \frac{1}{2} + \left\langle \delta_p^2 \right\rangle \ . \tag{4.19b}$$

From this measurement, it is found that the dark noise distribution follows a Gaussian distribution in phase space centered around zero for both the signal and idler SHs readouts, with standard deviations $\sigma_{\mathrm{dark,s}} = 5.2$ and $\sigma_{\mathrm{dark,i}} = 5.0$ respectively, meaning that the detection is limited by technical noise. This noise distribution broadly defines the confidence area for the localization in phase space for the set of joint measurements $\{x_l, p_l\}$. The contribution of this noise to the measured CEP sum fluctuations depends on the amplitudes $A_{\mathrm{s}} = \sqrt{{x_{\mathrm{s}}}^2 + {p_{\mathrm{s}}}^2}$ and $A_{\mathrm{i}} = \sqrt{{x_{\mathrm{i}}}^2 + {p_{\mathrm{i}}}^2}$ of the signal and idler SHs (the SH subscript used previously is here dropped to lighten the notation). The numerically calculated dependence is presented in Figure 4.21.

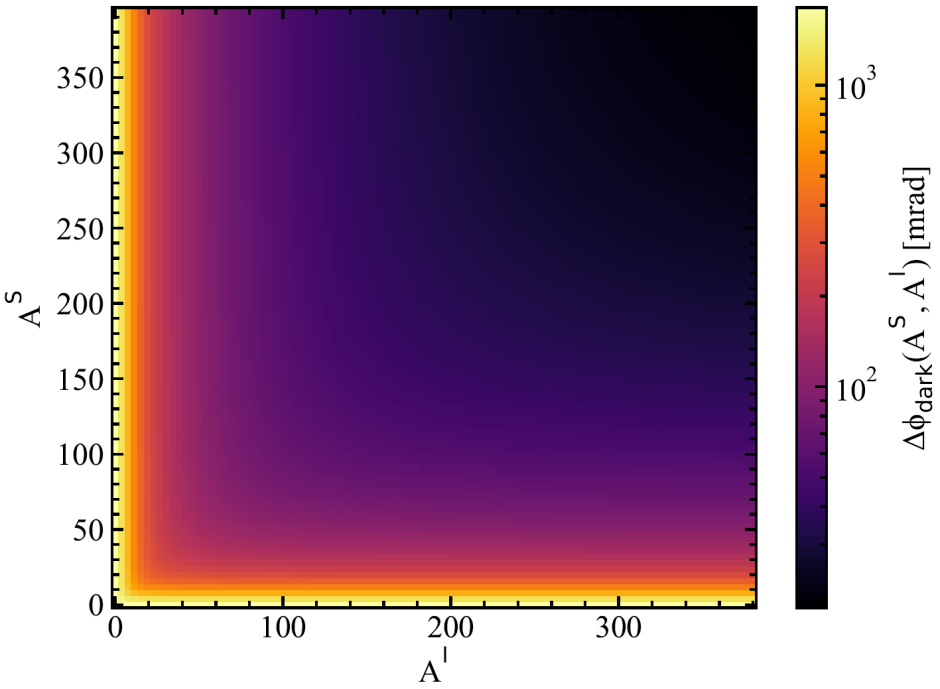

Figure 4.21 Amplitude dependence of the dark noise contribution to the measured CEP fluctuations.

For high amplitude events ($A_{\mathrm{s}} \gg \sigma_{\mathrm{dark,s}}$ *and* $A_{\mathrm{i}} \gg \sigma_{\mathrm{dark,i}}$), the contribution is small and can be approximated as

$$\Delta\phi_{\mathrm{dark}}(A_{\mathrm{S}}, A_{\mathrm{I}}) \approx \sqrt{\left(\frac{\sigma_{\mathrm{dark,s}}}{A_{\mathrm{s}}}\right)^2 + \left(\frac{\sigma_{\mathrm{dark,i}}}{A_{\mathrm{i}}}\right)^2} \tag{4.20}$$

while for very low amplitude events ($A_\mathrm{s} \ll \sigma_\mathrm{dark,s}$ *or* $A_\mathrm{i} \ll \sigma_\mathrm{dark,i}$), the measured CEP sum can fluctuate anywhere around 2π from the dark noise alone, and its contribution converges toward the standard deviation of a uniform distribution with a width of 2π

$$\Delta\phi_\mathrm{dark}(0, A_\mathrm{i}) = \Delta\phi_\mathrm{dark}(A_\mathrm{s}, 0) = \pi/\sqrt{3} \ . \tag{4.21}$$

Since the (fundamental) BTBs follow thermal photon statistics, in most measured events either or both SH beams have an amplitude below the dark noise level, despite the *average* amplitude being over 10 times above the dark noise level. The overall contribution $\langle\Delta\phi_\mathrm{dark}\rangle$ of the dark noise to the CEP sum statistics is therefore quite significant, and it is numerically evaluated from its quadratic mean over the measured joint amplitude distribution

$$\langle\Delta\phi_\mathrm{dark}\rangle = \sqrt{\frac{1}{M}\sum_{i=0}^{M}\Delta\phi^2_\mathrm{dark}(A_{\mathrm{s},l}, A_{\mathrm{i},l})} = 540 \text{ mrad} \ .$$

After deconvolution of the dark noise, the conclusion of the measurement is that the signal and idler SHs are phase-locked to the pump and to each other with an uncertainty of 490 mrad on average. On one hand, this value is over 54 times greater than the standard quantum limit $\Delta\phi_\mathrm{SQL} \sim \left(2\sqrt{\langle n\rangle}\right)^{-1} \approx 9\,\mathrm{mrad}$ one finds for coherent states with the same average number of photons [135]. On the other hand, based on the present analysis it is only 4.5 greater than the average quantum-limited phase noise $\langle\Delta\phi_\mathrm{QL}\rangle = 110\,\mathrm{mrad}$ one finds for two light sources with the same amplitude distribution as those measured here. The stark difference between these two limits illustrates the fact that any hypothetical state which would minimize phase fluctuations would cover a pie-slice in phase space (see e.g. the Q function of the Pegg-Barnett phase eigenstate in Figure 2.8) and would therefore always have a large amplitude, contrary to the thermal-like states here considered.

4.3.3 Q Function

The present scheme yields not only a readout of the CEP, but also the amplitude of each pulse pair, therefore performing a direct sampling of their Q function (smoothed by the dark noise). Figure 4.22 show the individual distribution measured for the two SH beams. In each plot, the contour lines represent the circumference in phase space past which the number of event per bin drops below the indicated number. Both distributions are broad and circularly symmetric, owed to the thermal photon statistics and random phase of the fundamentals.

Taking now one quadrature from each beam, the joint distributions plotted in Figure 4.23 are obtained. Here, squashing of two-mode quadratures resulting from the PDC process can be

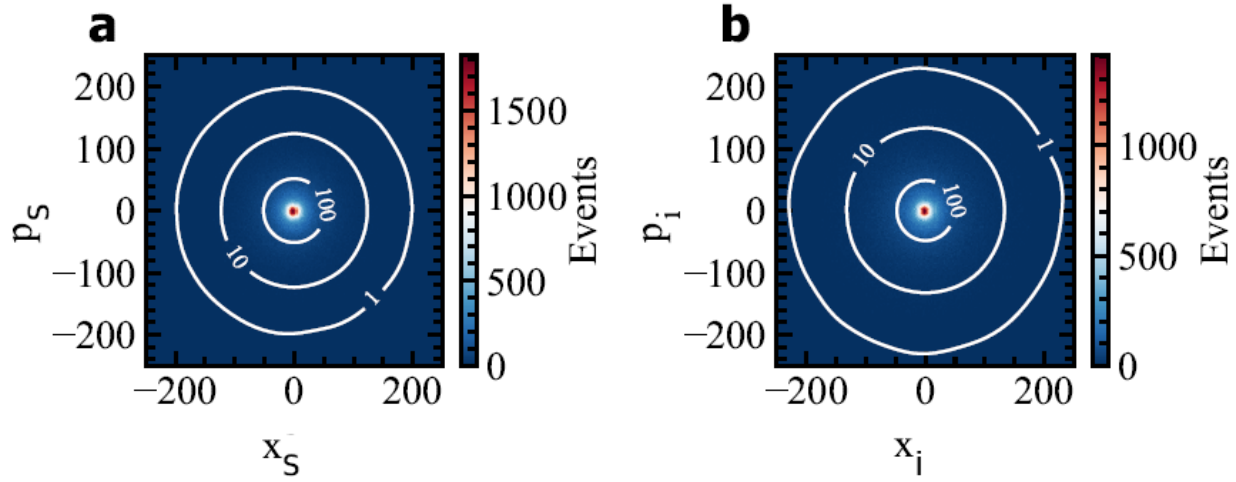

Figure 4.22 Q function of the signal (a) and idler(b) SHs.

observed from the reduced width of the distribution along either the diagonal or anti-diagonal directions compared to the individual distributions in Figure 4.22. The joint distributions resulting from the other combinations of quadratures (i.e. x_s with p_i, and p_s with x_i) are not plotted since they are entirely uncorrelated to each other and therefore show no distinctive feature.

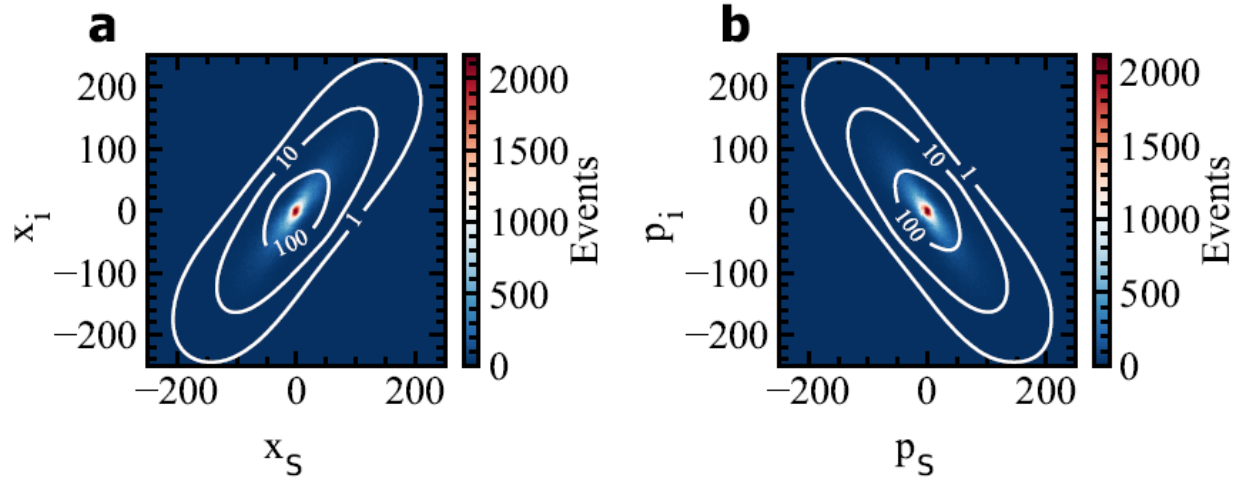

Figure 4.23 Q function of the two-mode in-phase (a) and out-of-phase (b) quadratures of the two SH beams.

Finally, a proof-of-principle demonstration of the ability to perform post-selection conditioning using protocols based on both the amplitude and the CEP of BTBs is presented in Figure 4.24. Each subplot presents the Q function of the idler SH obtained after a applying a binary post-selection based on the measured amplitude and phase of the signal SH.

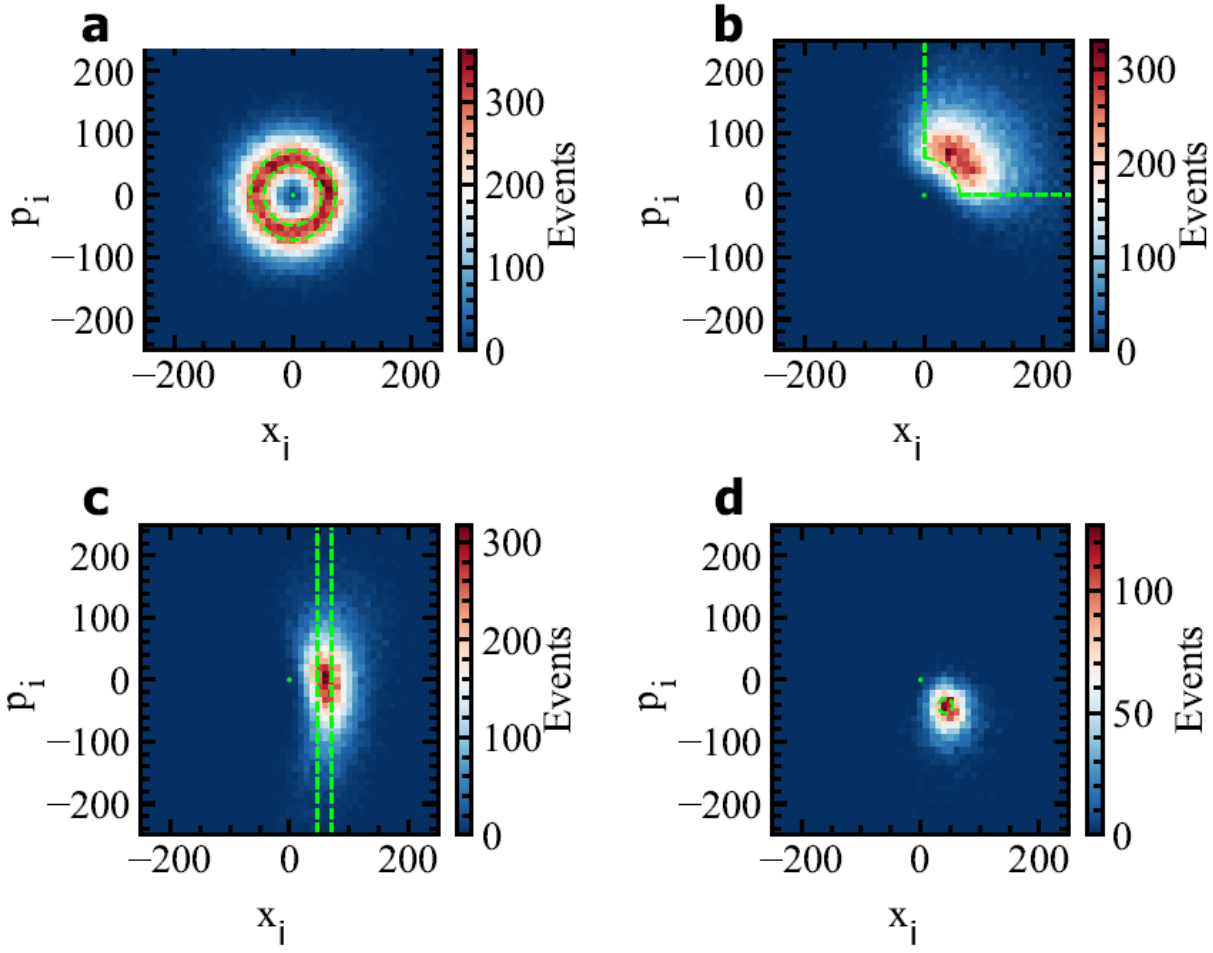

Figure 4.24 Q function of 4 post-selected idler states aiming to mimic the shapes. The dashed green lines show the delimitation of the post-selected distributions expected in the limit of infinite squeezing.

Thanks to the large area covered in phase space by the initial state, a wide variety of states can be generated with a relatively high efficiency and in parallel. In Figure 4.24a, the post-selection protocol selects events where the signal amplitude fits within a narrow bin, a similar strategy to those used to generate sub-Poissonian light [21], resulting in a distribution visually resembling that of a Fock state. In Figure 4.24b, the protocol now selects events where the signal CEP fits within one quadrant and where the amplitude exceeded 10 times the dark noise. In Figure 4.24c, the protocol instead selects events where the in-phase quadrature of the signal fits within a narrow bin. Finally, Figure 4.24d presents the result of a protocol where only events located near a specific point in phase space are kept, resulting in a coherent-like state.

CHAPTER 5 SEMI-CLASSICAL SIMULATIONS OF PARAMETRIC DOWN-CONVERSION IN THE HIGH-GAIN, FEW-CYCLE REGIME

This chapter presents simulation results that aim to model the parametric down-conversion (PDC) process in the bright twin beams (BTBs) implementation presented in Chapter 4, using the semi-classical numerical model presented in section 3.1. The objectives here are to clarify the role of the Kerr effect in the generation of ultrafast BTBs, allow the observation of the internal dynamics of the PDC process i.e. beyond the input/output experimental observation, and identify potential strategies to experimentally demonstrate nonclassicality via the noise reduction factor (NRF) with this source.

5.1 Reproduction of Experimental Conditions

As a first step and to establish a reference point for the rest of the numerical analysis, this section present results of the simulation where the input parameters aim to reproduce the experimental conditions as faithfully as possible. The pulse shape of the pump right before entering the beta barium borate (BBO) crystal is measured via second-harmonic frequency-resolved optical gating (SH-FROG), and the retrieved pulse shape from that measurement is used as the temporal envelope of the pump in the simulation. In the absence of a detailed characterization of the transverse beam profile, a Gaussian beam shape with the same beam waist $\mathrm{w}_0 = 20\,\mu\mathrm{m}$ is assumed. To model the astigmatism of the pump beam, the x and y focal planes are set to $z = L/2 - z_\mathrm{R}$ and $z = L/2 + z_\mathrm{R}$ respectively, where $L = 4\,\mathrm{mm}$ is the thickness of the BBO crystal along the propagation direction.

Here, the statistics are calculated from repeating the simulation $M = 10^3$ times with different RNG seeds for the pseudo-random phase of the vacuum-like seed. The pump energy is set to 86.5 nJ, which is equivalent to the pumping conditions in the photon statistics measurements of section 4.2.4 when accounting for Fresnel reflection.

5.1.1 Results

Figure 5.1 presents the evolution of the photon statistics (the average $\langle n \rangle$, the second-order autocorrelation function $g^{(2)}$ and the NRF) of the BTBs as they propagate through the 4 mm-thick BBO crystal. As expected from the theory of low-gain PDC, the BTBs states starts off in a heavily multimode regime ($g^{(2)} \sim 1$) due to the strongly-chirped pump pulse. As the pump approaches temporal compression around $z = 2.5\,\mathrm{mm}$, the number of down-converted

photons starts rising at a super-exponential rate while the number of spatio-temporal modes is rapidly decreasing. Simultaneously, the NRF can be seen to suddenly increase and reach unity around $z = 3\,\text{mm}$.

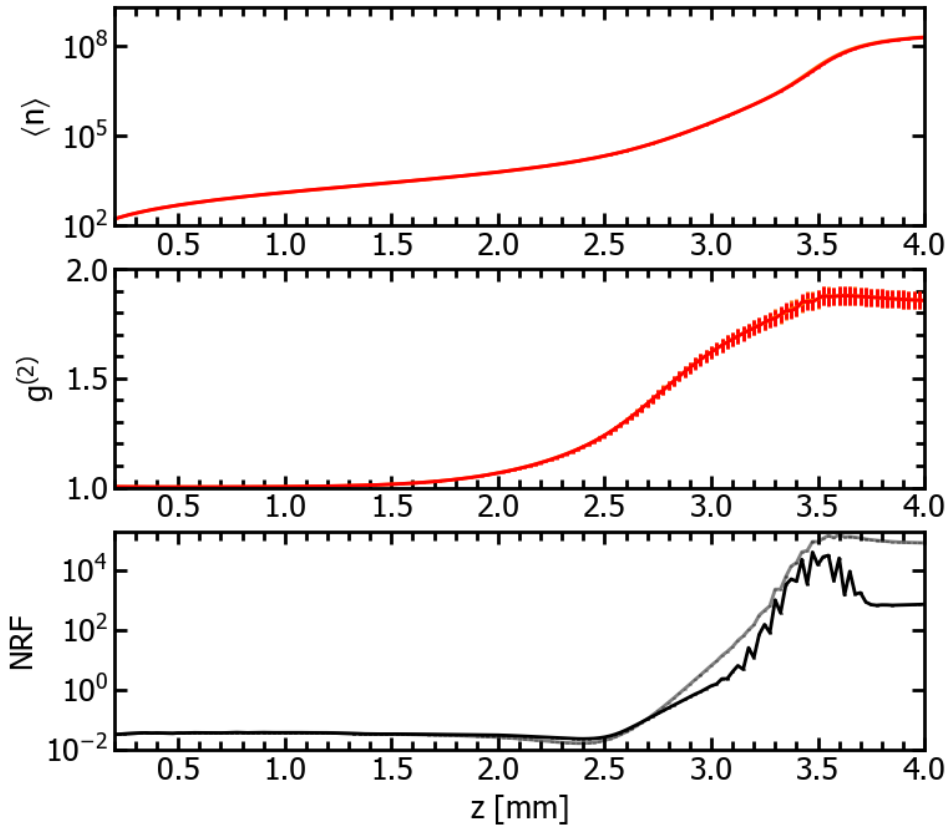

Figure 5.1 Evolution of the photon statistics of the BTBs for the conditions of the experiment. The grey and black NRF curves correspond to definitions (2.60) and (2.61) respectively.

The average number of photons at the output predicted by the simulations is nearly two orders of magnitude too high. This can be explained by a combination of 3 factors : 1) the exponential dependence of $\langle n \rangle$ on the pump field amplitude, which in the high-gain regime amplifies the uncertainty on the pump intensity (see appendix B), 2) the pump intensity toward the end of the propagation where the gain increases the fastest in turn depends nonlinearly on the input intensity, and 3) the numerical model neglects multiple higher-order nonlinear effects (multi-photon absorption, Raman scattering) and experimental factor (imperfect Gaussian beam quality) that would all experimentally contribute in reducing the pump intensity, and their absence in the simulation therefore lead to an overestimation of $\langle n \rangle$.

This overestimation of the parametric gain should not significantly affect the rest of the results that do not depend as strongly on the pump intensity, so long as propagation dynamics are

properly reproduced in the simulation. The simulation indeed predicts an output value of the autocorrelation function $g^{(2)} = 1.85$. This is in good agreement with the experimental result $g^{(2)} = 1.937$ when considering that the simulated detector has an infinite bandwidth, whereas the experiment is limited by the quantum efficiency of InGaAs sensors and might therefore lead to an overestimation of $g^{(2)}$. As for the predicted value of the noise reduction factor NRF = 719, its higher value in the simulation can be attributed to the dependence of the NRF on the shot noise level $\sqrt{\langle n \rangle}$.

To further ensure that the simulation correctly reproduce the nonlinear propagation of the pump, Figure 5.2 presents a comparison between the spectrum of the pump at the position $z = 3\,\text{mm}$ in the simulation, and the measured pump spectrum at the output of an early implementation of the BTBs source which used a 3 mm-thick BBO crystal. A good agreement can be observed between the two spectra, validating that the simulation properly models the propagation dynamics of the pump, and also demonstrating the importance of including $\chi^{(3)}$ effects in this study.

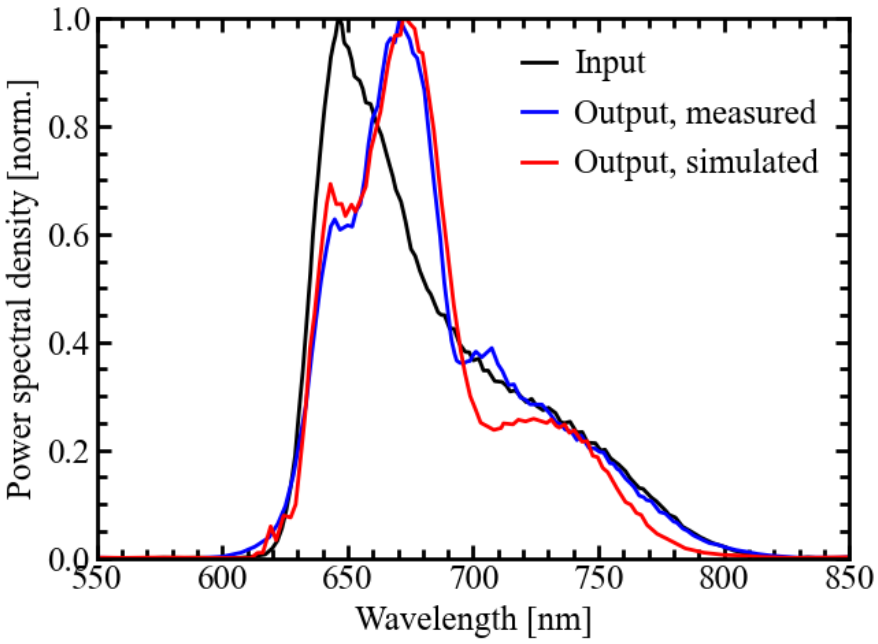

Figure 5.2 Measured vs. predicted shape of the optical spectrum of the pump after propagation through a 3 mm-thick BBO crystal.

Next, Figure 5.3 presents the k-space power density of the BTBs at the output $z = L$ plotted in both linear (left) and log (right) scales. This distribution provides an approximation for the transverse beam profile in the far-field as measured in section 4.2.1. The asymmetry

between the signal and idler beams can again be observed, and is even more pronounced in the simulation, possibly again due to its effectively infinite detection bandwidth. A first hint as to the reason why the Kerr effect leads to a rise of the NRF above unity is shown in the log-scale plot, which contrary to the experiment is not limited by the dynamic range of instrument. It can indeed be observed that the signal and idler beams are spread across the $k_x = 0$ line despite seeming well-separated in the linear-scale plot. This line is indeed used as a divider to distinguish the signal from the idler, under the important assumption that both beams have negligible intensity at that position. While a relative intensity on the order $\sim 10^{-3}$ *might* seem negligible, it is comparable to the relative shot noise level on which the NRF is based on.

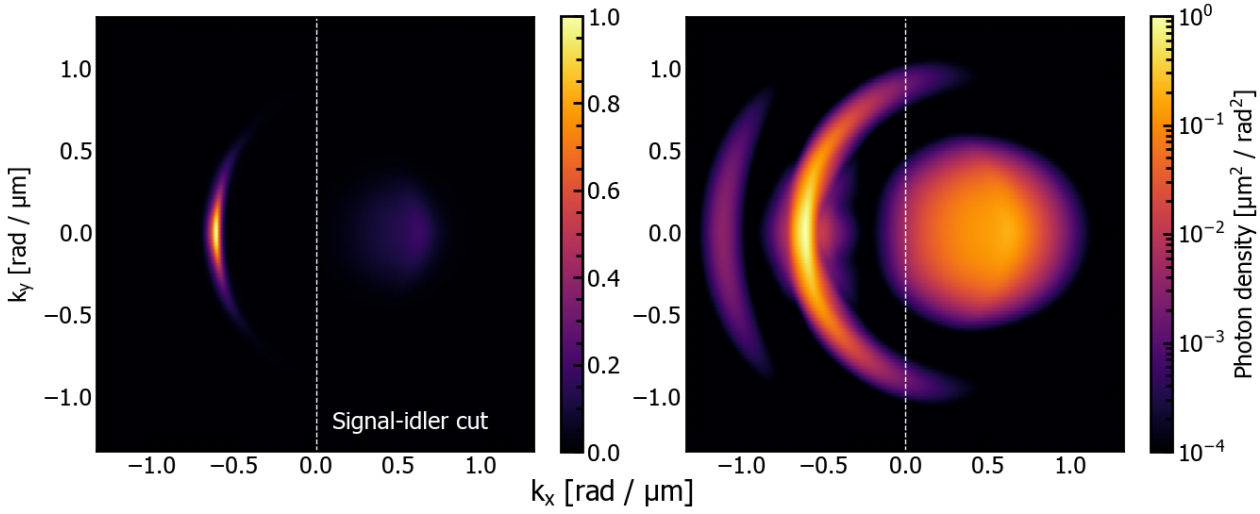

Figure 5.3 Farfield beam shape for the conditions of the experiment.

At first glance, one might think that reshaping the dividing line in a semi-circle-like might reduce the NRF back down to sub-unity values. However, this strategy provides almost no improvement to the NRF, because the assumed left-to-right correlations between the BTBs doesn't apply to light generated near the $k_x = 0$ line. Indeed, momentum conservation dictates that on this line, upward ($k_y > 0$) components are instead correlated with downward ($k_y < 0$) components, while components generated along the pump axis $k_x = k_y = 0$ are only self-correlated and cannot be split. Therefore, any attempt to improve the source toward demonstrating a quantum advantage via twin beam entanglement (e.g., measuring NRF < 1) should first aim to improve their separability in k-space.

Turning now to the time-frequency domain, Figure 5.4 presents the statistics of the output pulses and spectra for the BTBs and the pump. For all curves, a solid line is used to plot the average and a shaded area shows a width corresponding to one standard deviation. On aver-

age, the signal pulse has a full-width at half maximum (FWHM) duration slightly longer than 13 fs, in close agreement with the frequency-resolved optical gating (FROG) measurement in section 4.2.3. As predicted, the idler has a shorter duration of 10 fs thanks to its carrier-wavelength being closer to the zero-dispersion point of BBO. The signal and idler spectra also qualitatively resembles the measurements from section 4.2.2, although the simulation predicts a bandwidth for both beams that is much larger than what the InGaAs spectrometer used in the experiment can resolve. The effective bandpass filtering performed by the finite detection bandwidth of the detectors can also explain the large experimental value of the NRF, as such filtering increases the effective losses while also introducing unbalanced detection of higher-order modes.

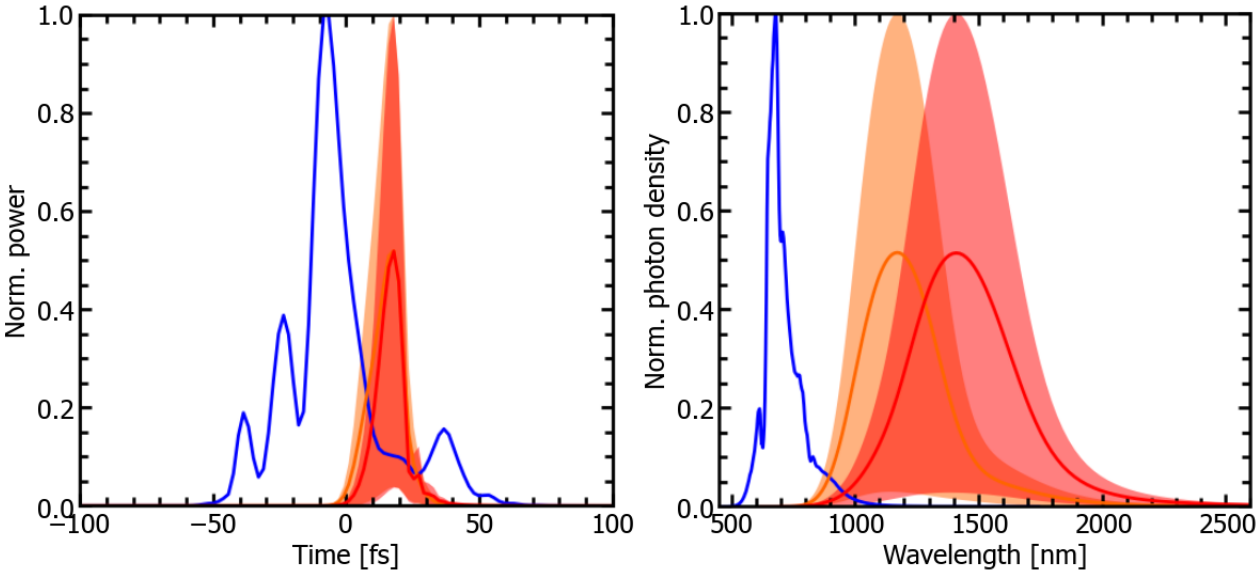

Figure 5.4 Output pulse shapes and spectra for the conditions of the experiment.

Finally, Figure 5.5 present the evolution of the average pulse shape of the pump, signal and idler as they propagate in the BBO. At the beginning of the PDC process, when the pump is still strongly dispersed, the signal and idler are generated by the most intense of its two peaks. As the gain increases and the pump compresses, the signal and idler pulses grow shorter until they reach a minimal FWHM pulse duration of 7.4 fs and 6.8 fs respectively around $z = 3.5$ mm, which explains the $g^{(2)}$ peaking around that point from a minimization of the number of temporal modes. Past that point, group velocity mismatch separates the BTBs from the pump, dramatically slowing down their amplification and allowing them to accumulate chromatic dispersion which stretches the two pulses to their final pulse duration observed in Figure 5.4.

These last results suggest that a future iteration of the BTBs source could achieve significantly

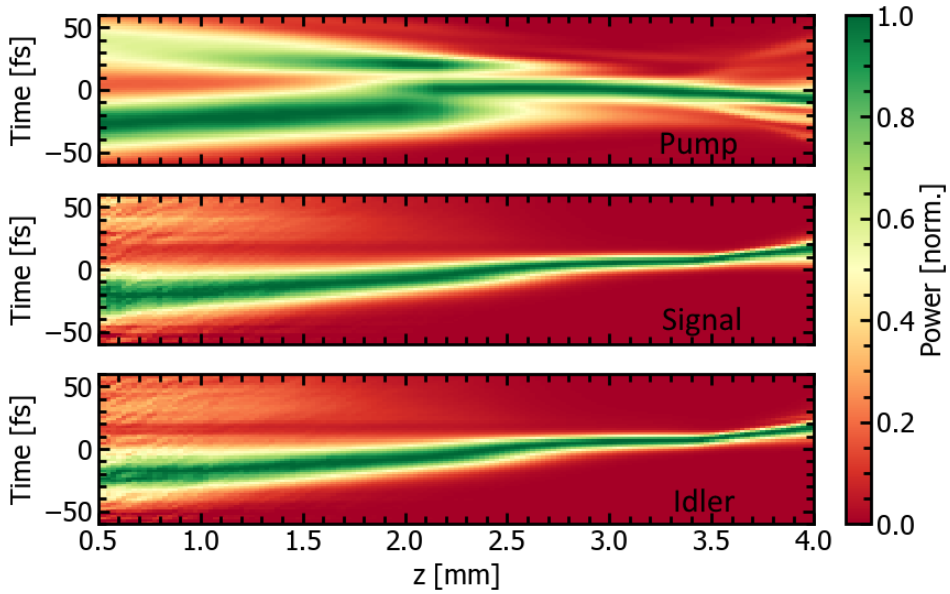

Figure 5.5 Evolution of the pulse shapes for the conditions of the experiment.

shorter pulses by substituting the nonlinear medium by a 3.5 mm-thick BBO crystal, with only a slight reduction of the parametric gain. On the other hand, the simulation also predicts that the NRF is maximal around that point, making it even harder to demonstrate a quantum advantage in this scenario. Considering the fact that $\chi^{(3)}$ effects are suspected to cause the observed rise of the NRF and that they also affect the pulse shape of all three beams, it would be more advisable to first alter the source toward the objective of achieving NRF < 1, and then optimize it for other factors.

5.2 Propagation in a $\chi^{(3)}$-less Medium

To demonstrate that the Kerr effect stemming from the $\chi^{(3)}$ response of the nonlinear medium is responsible for the loss of nonclassical correlations, this section presents results from repeating the simulations in section 5.1 with the third-order term of the nonlinear polarization artificially set to 0. All other parameters, including the RNG seed, are the same to ensure any change observed is caused by the absence of this term. The number of simulations is however reduced from 10^3 to 10^2 to reduce the calculation time.

5.2.1 Results

Figure 5.6 presents the photon statistics of the BTBs throughout the synthetic $\chi^{(3)}$-less BBO. The evolution remains similar to what is observed in Figure 5.1 for the first 2.5 mm where

the pump is not compressed. Past that point, a significant reduction of the parametric gain can be observed, which can be explained from the slower compression of the pump in the absence of the self-phase modulation (SPM). On the other hand, the $g^{(2)}$ continues rising all the way until the end of the interaction rather than peaking at $z = 3.5\,\text{mm}$, and most importantly the NRF remains far below unity throughout the entire propagation. Since the numerical model is not quantized, the exact value of the NRF found here is meaningless, but its stark decrease from the previous simulations remains significant.

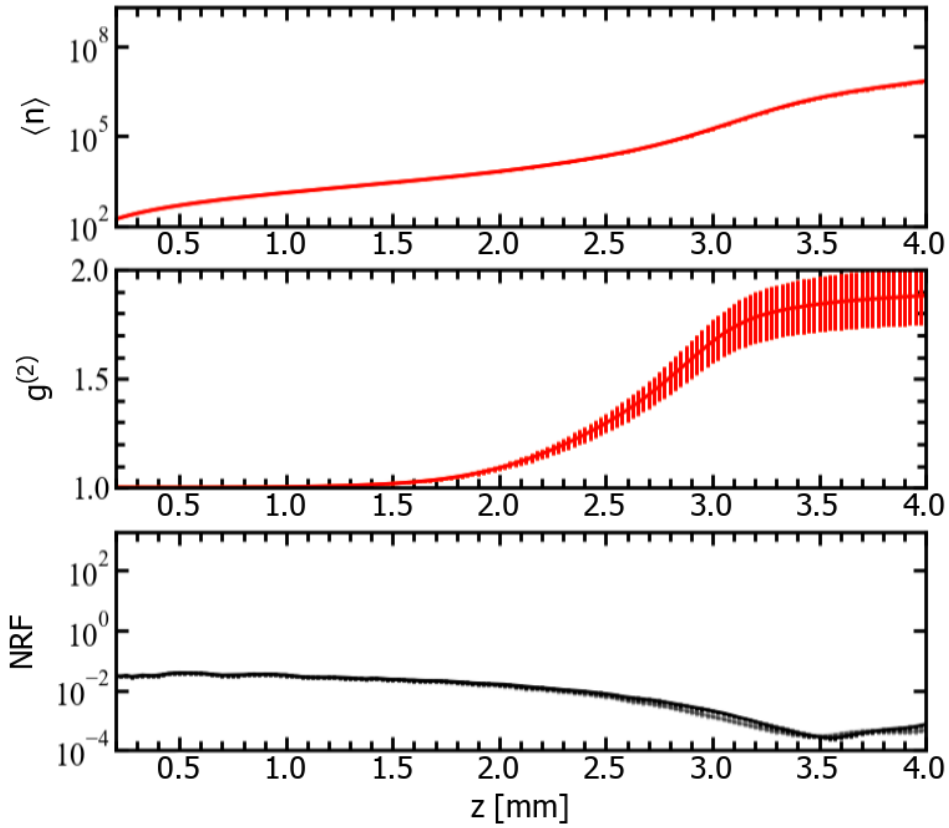

Figure 5.6 Evolution of photon statistics in $\chi^{(3)}$-less conditions.

Turning to the output k-space power density of the BTBs in Figure 5.7, the conservation of entanglement can be explained by the well-separated, beamlike shape of the signal and idler, even when plotted on a log-scale. This link between the NRF and the k-space distribution of BTBs suggest that the main limiting effect is self-focusing specifically, rather than SPM or the Kerr effect as a whole.

Quite surprisingly, this $\chi^{(3)}$-induced reshaping of the BTBs stems almost exclusively from self-focusing of the *pump*. Indeed, when the simulations are repeated with the $\chi^{(3)}$ term removed only for the down-converted modes, the results are nearly-identical to those presented in

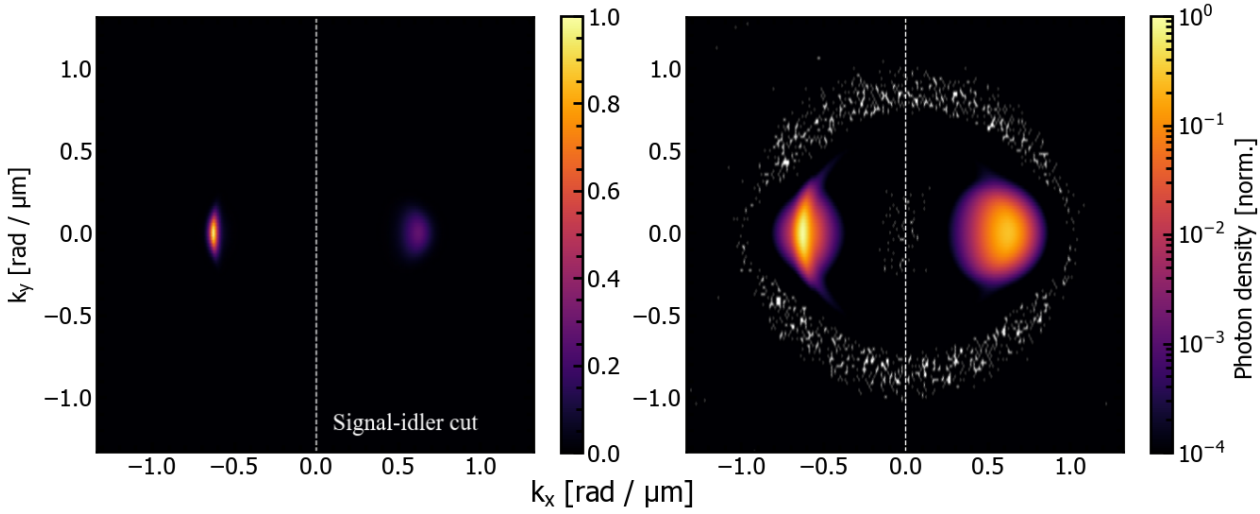

Figure 5.7 Farfield beam shape in $\chi^{(3)}$-less conditions.

section 5.1. This effect can be understood as self-focusing increasing the angular bandwidth of the pump, and therefore allowing it to drive phase-matched PDC for other pairs of k-vectors than the two beam-like directions observed in this $\chi^{(3)}$-less scenario. The conclusion is therefore that to maintain the entanglement of the BTBs, an effort should be made to prevent self-focusing of the pump specifically such that the signal and idler remain spatially well-separated in the far field.

Finally, an interesting consequence from the absence of $\chi^{(3)}$ effects is a pronounced reduction of the asymmetry between the signal and the idler, as can be best observed from the statistics of their pulse shape and spectrum plotted in Figure 5.8. Here, both beams have a carrier wavelength around 1350 nm, closely matching the frequency-degenerate design expected from phase-matching calculations in section 3.3.2. This symmetry extends to the time domain, where both pulses have a FWHM duration of 13.7 fs despite their mismatched bandwidths.

5.3 Potential Strategies to Reduce Detrimental $\chi^{(3)}$ Effects

The results of section 5.2 reflect the expectations from the initial design of the source in section 3.3.2, demonstrating how significantly $\chi^{(3)}$ effect can alter the properties of a twin beams source in the high gain regime. The present section numerically tests two simple alterations to the experimental setup that would lead to a reduced third-order nonlinear response toward the main objective of reaching sub-unity NRF values without sacrificing the other main features of the source.

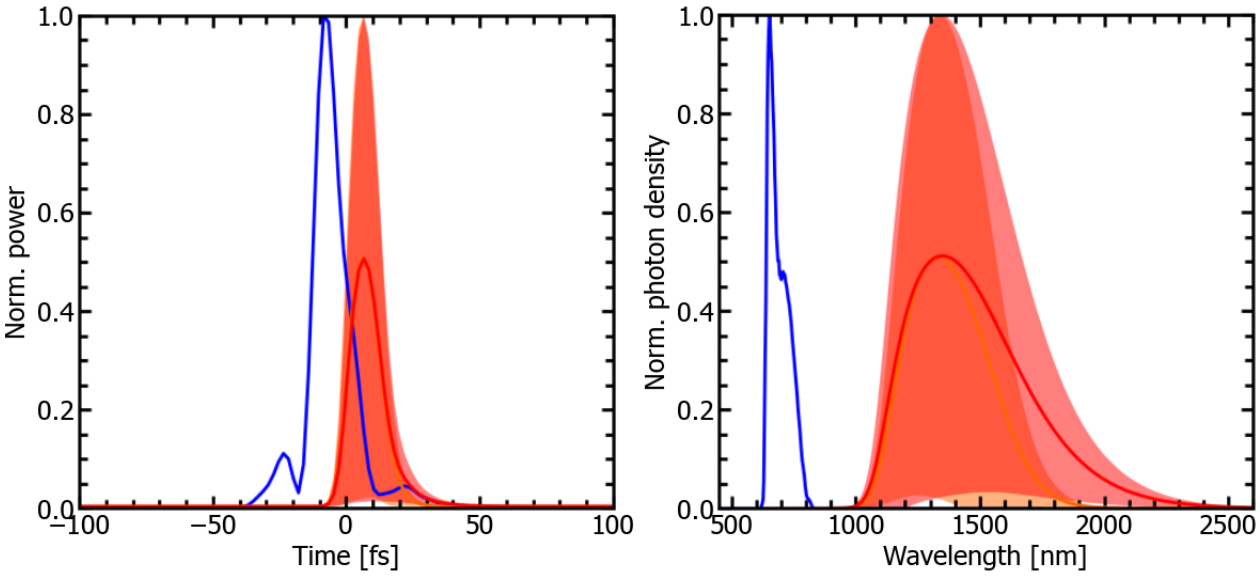

Figure 5.8 Output pulse shapes and spectra in $\chi^{(3)}$-less conditions.

5.3.1 Loosely-Focused, Longer Pump Pulse

The most straightforward change that could be made to the source is to increase the beam area and the pulse duration of the pump as to reduce the relative strength of the spatio-temporal lens created by the Kerr effect. Here, the beam radius is increased by a factor $\sqrt{10}$, and the pump is replaced by a Gaussian pulse with a 100 fs FWHM duration, about 10 times longer than the experiment. This results in a spatio-temporal pump volume that is 100 times larger than before, and the main expected consequence is for the BTBs to now be multimode. To compensate for the resulting lower intensity, the pump energy is increased by a factor of 6.5 to achieve a average number of photons at the output comparable to that in section 5.1.

First, Figure 5.9 presents the photon statistics of the BTBs with the enlarged pump. The number of photons now grows at a steady exponential rate for the entire interaction, thanks to the new pump being nearly unaffected by diffraction and dispersion, and therefore satisfying the stationary pump assumption of textbook treatments of PDC. As expected, the greater spatio-temporal volume covered by the pump results in a larger number of Schmidt modes, which can be observed by the reduced value of $g^{(2)} = 1.1$. Interestingly, the inferred number of mode $K = (g^{(2)} - 1)^{-1} \approx 10$ which is much lower than the 100-fold increase one would expect in the low-gain regime. Most of all, the NRF now maintains sub-unity values throughout the entire interaction, despite not reaching values that are as low as in the artificial $\chi^{(3)}$-less scenario.

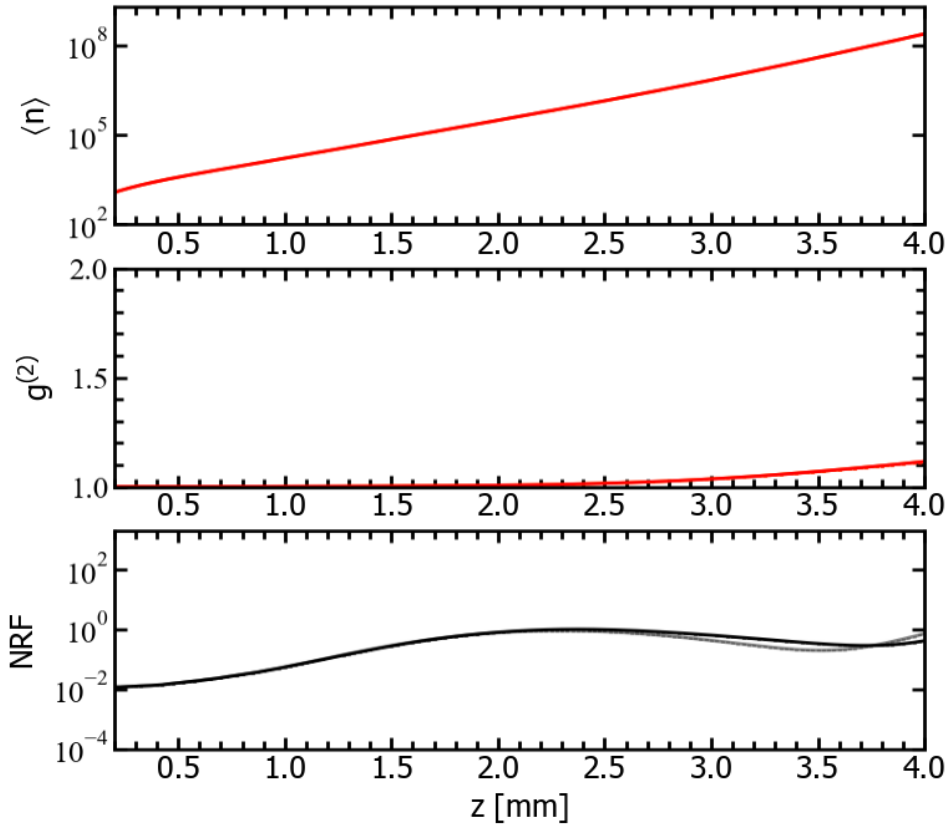

Figure 5.9 Evolution of photon statistics in multimode pumping conditions.

A potential explanation for this intermediate result on the reduction of the NRF can be found by looking at the output k-space power density of the BTBs plotted in Figure 5.10. The separability of the BTBs is significantly improved when compared to the experimental conditions, but the enlarged beam area of the pump means that the walkoff-induced spatial selection effect is reduced [24, 177] and downconverted light is generated all along the phase-matched cone. In this scenario, the use of two apertures to the left and to the right with matched areas [68] might improve the NRF and even reduce the effective number of modes.

Finally, the biggest downside to this strategy is the resulting temporal and spectral shape statistics of the BTBs, which are plotted Figure 5.11. Not only the pulses are now stretched to an average FWHM duration of over 44 fs, but their multimode composition (visible from the reduced width of the shaded area) means their is no well-defined envelope for the pulses to define a carrier-envelope phase (CEP) with. This last issue can be solve by filtering (in space and in frequency domains) the BTBs to recover single-mode statistics as in e.g. [42], but then the resulting pulse will be longer and the added losses will typically remove any quantum advantage [23].

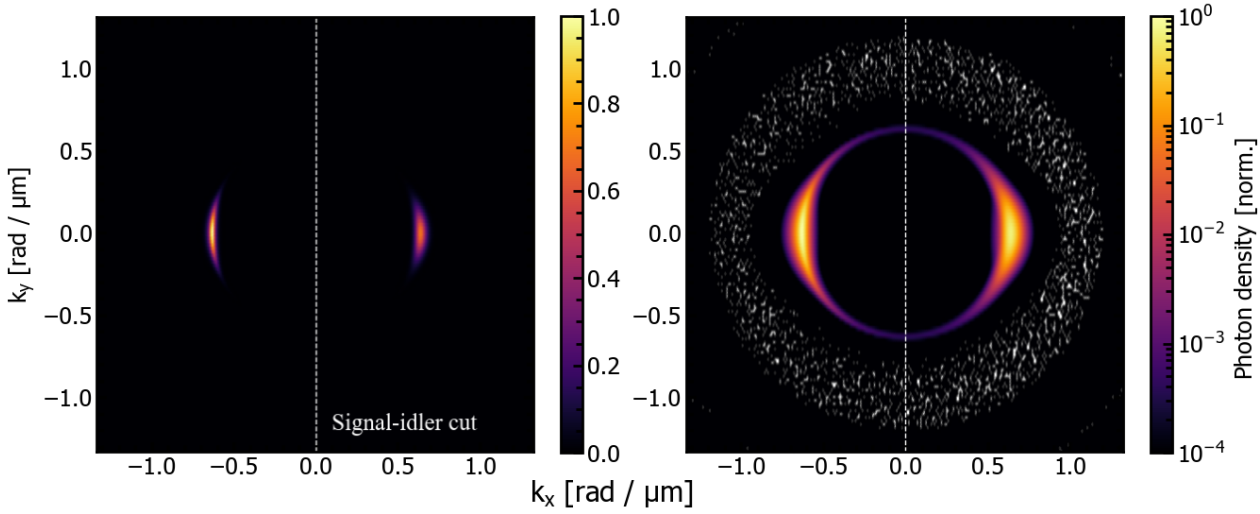

Figure 5.10 Farfield beam shape in multimode pumping conditions.

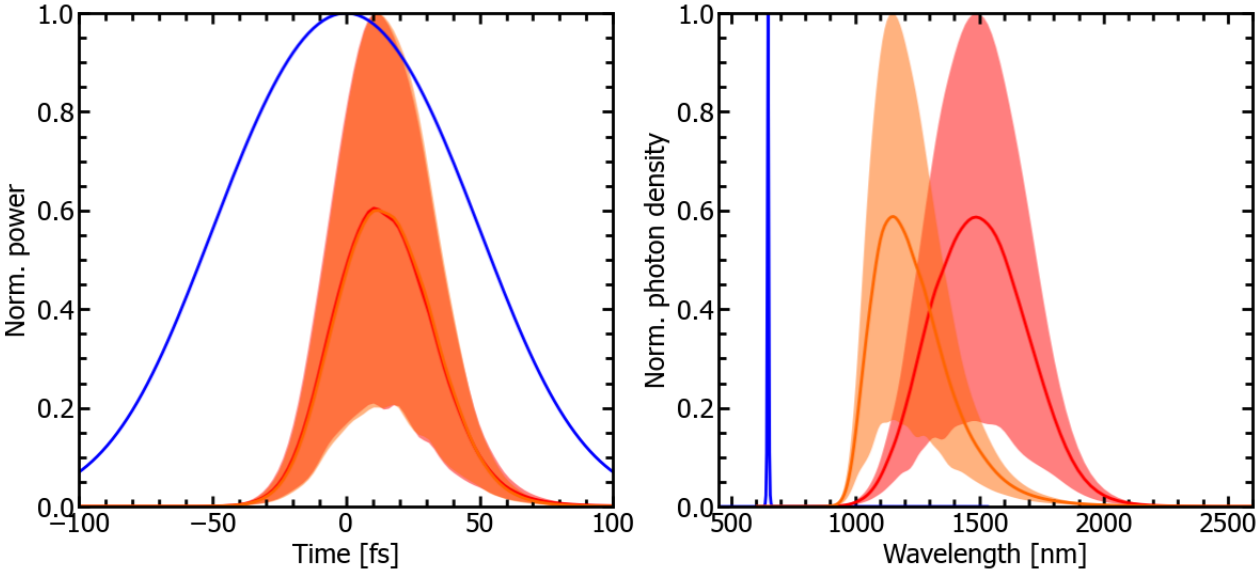

Figure 5.11 Output pulse shapes and spectra in multimode pumping conditions.

5.3.2 Divergent Pump

Another well-known strategy in the nonlinear optics community to mitigate self-focusing is to inject a divergent beam in the nonlinear medium [181]. This allows the use of pulses with much higher peak powers before the beam collapses into a filament by canceling the focusing power of the Kerr lens with the diffraction of the diverging beam. Here, this scheme was simulated by placing the geometrical focus of the pump (both in the x and y directions) at the entry face of the BBO $z = 0$, and leaving every other parameters unchanged from the

experimental case.

The resulting photon statistics are shown in Figure 5.12. The cancellation of self-focusing by the divergence of the pump results in an effective beam area that is larger than in the experimental case, yet smaller than the astigmatic pump in the $\chi^{(3)}$-less case, and therefore yielding a parametric gain that is in between these two scenarios. The value of the autocorrelation function $g^{(2)}$ also rises much faster than in any other simulated scenarios, which can be attributed to an accelerated compression of the pump pulse by SPM from the initially smaller beam size. The subsequent drop of $g^{(2)}$ past $z = 2.8\,\text{mm}$ can then be attributed to multimode amplification once the pump pulse elongates in time from dispersion. Primarily, the NRF now stays smaller than one throughout the entire interaction despite the presence of the third-order nonlinear polarization term, and its final value is even comparable to the $\chi^{(3)}$-less case.

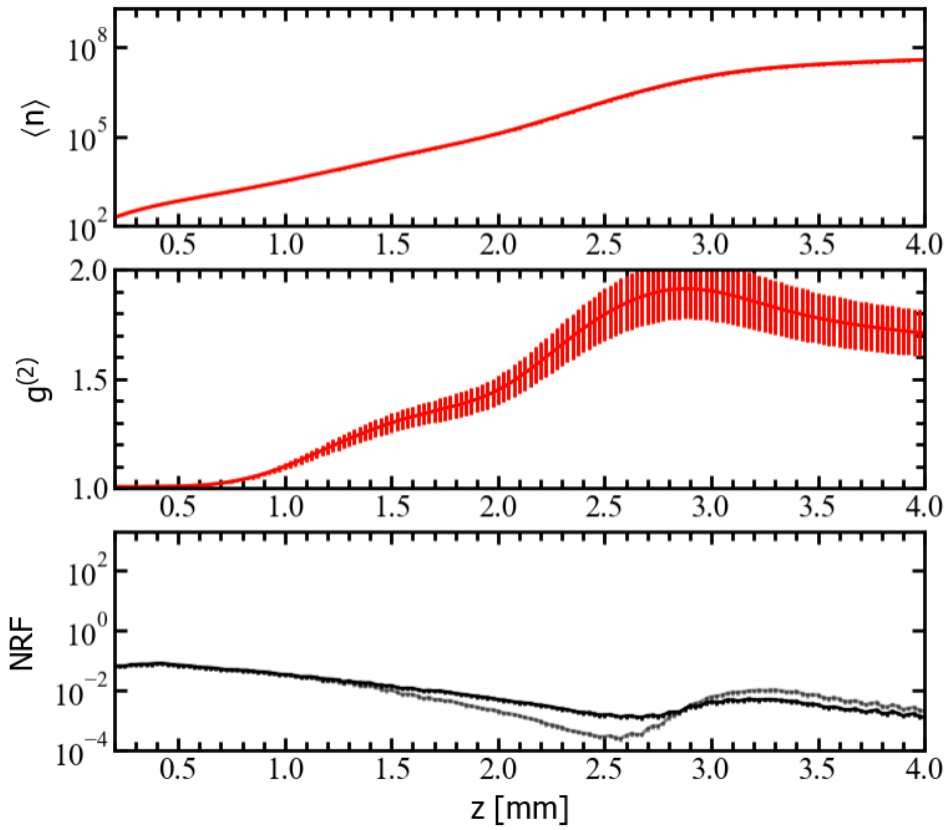

Figure 5.12 Evolution of photon statistics with a divergent pump beam.

These results suggest that self focusing of the pump is indeed the main cause of loss of twin beams squeezing. This hypothesis is reinforced by the k-space power density of the BTBs plotted in Figure 5.13, which has no discernible component along the $k_x = 0$ line even in the

log-scale plot despite a noticeable broadening of the distribution by $\chi^{(3)}$ effects. This also indicates that an experimental implementation of this scheme would greatly benefit from a high-dynamic-range analysis of the transverse beam profile of the BTBs to ensure that this separability is achieved. Such a measurement is however technically challenging due the large power fluctuations of single-mode sources which further increase the required dynamic range.

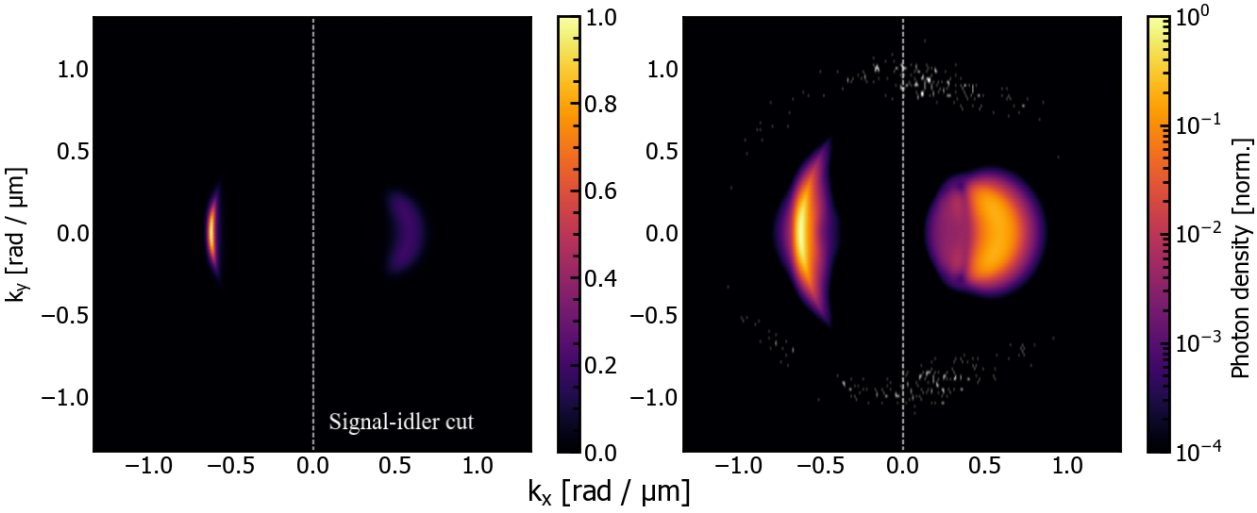

Figure 5.13 Farfield beam shape with a divergent pump beam.

Turning finally to the pulse shape and the spectrum statistics in Figure 5.14, the resulting distributions mimics those from the $\chi^{(3)}$-less simulation with nearly-frequency-degenerate signal and idler, but this time with a slightly longer pulse duration of over 20 fs due to the multimode amplification toward the end of the propagation. If the BBO is truncated to the point $z = 2.8\,\text{mm}$ where the value of $g^{(2)}$ is maximized, the resulting output pulse duration is reduced to less than 9 fs for both the signal and the idler, resulting in sub-2-cycle pulses.

5.4 Impact of Frequency-Dependent Quantum Efficiency

While sections 5.3.1 and 5.3.2 focus on solving the loss on nonclassical correlations by self-focusing in an idealized detection scenario, they do not address the technically difficult problem of needing near-perfectly balanced detection effiencies for all modes which was highlighted in section 4.2.4. This issue is further analyzed here by studying the impact of bandwidth-limited, and more generally frequency-dependent quantum efficiency $\eta(\omega)$ of the detector on the NRF. To fully isolate it from issues stemming from the generation process, the output from the $\chi^{(3)}$-less simulations are taken as an input in this numerical analysis. The spectrally-resolved photon statistics $\hat{n}_{(\text{s,i})}(\omega)$ of the signal and idler are converted into detected photons

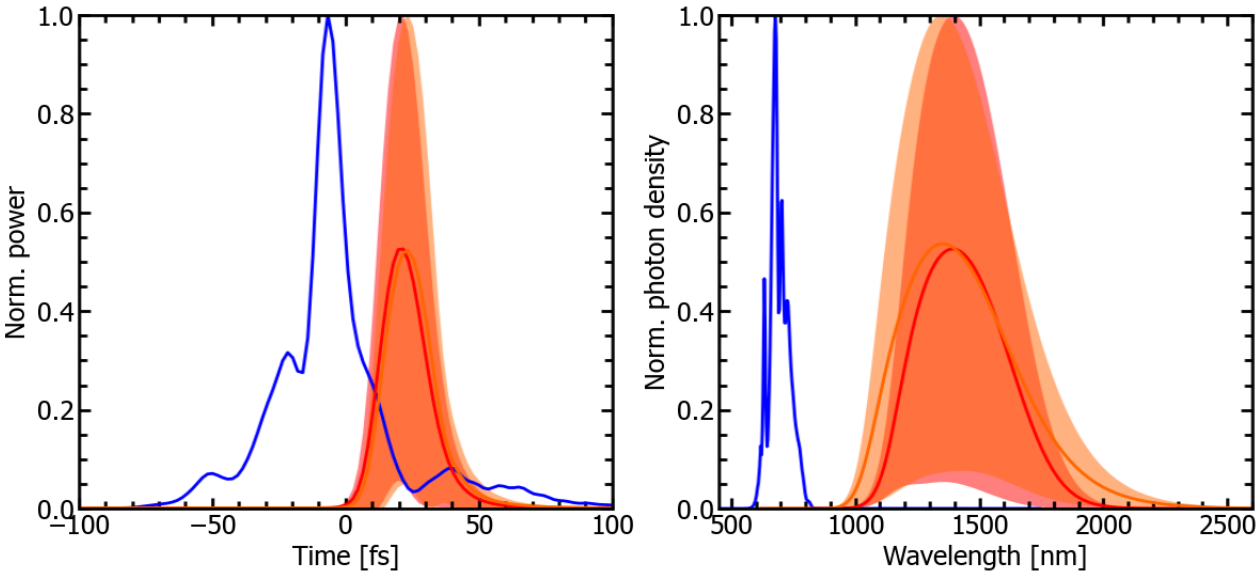

Figure 5.14 Output pulse shapes and spectra with a divergent pump beam.

$\hat{m}_{(\mathrm{s,i})}$ by calculating the mean and variance of a binomial process with a probability of success $\eta(\omega)$ for the photons contained in all frequency bins and then integrating over all frequencies. The impact of angular filtering is not treated, as it can be easily resolved experimentally with the use of wide-aperture optics and large-area detectors.

5.4.1 Detector Bandwidth

First, to identify the minimal detection bandwidth required to maintain the NRF < 1 condition, consider a synthetic detector with a rectangular quantum efficiency function

$$\eta(\lambda) = H(\lambda - \lambda_{\mathrm{on}}) - H(\lambda - \lambda_{\mathrm{off}}) \tag{5.1}$$

where $H(\lambda)$ is the Heaviside step function, and $\lambda_{(\mathrm{on,off})}$ are the cut-on and cut-off wavelength of detection. The resulting NRF is plotted as a function λ_{on} and λ_{off}, using either definitions of the NRF : (2.60) (left) or (2.61) (right). In both cases, the values in the top left corner of the plot corresponds to a scenario where the detector bandwidth far exceed the bandwidth of BTBs, reproducing the results with the perfect detectors in section 5.2. Then, as λ_{on} increases or λ_{off} decreases, the NRF slowly increases toward, and then past unity. The minimum bandwidth is obtained using eq. (2.61), where sub-unity NRF values are maintained up until $\lambda_{\mathrm{on}} = 990\,\mathrm{nm}$ and $\lambda_{\mathrm{off}} = 2400\,\mathrm{nm}$.

This minimal bandwidth extends far past the cut-off detection wavelength of standard In-

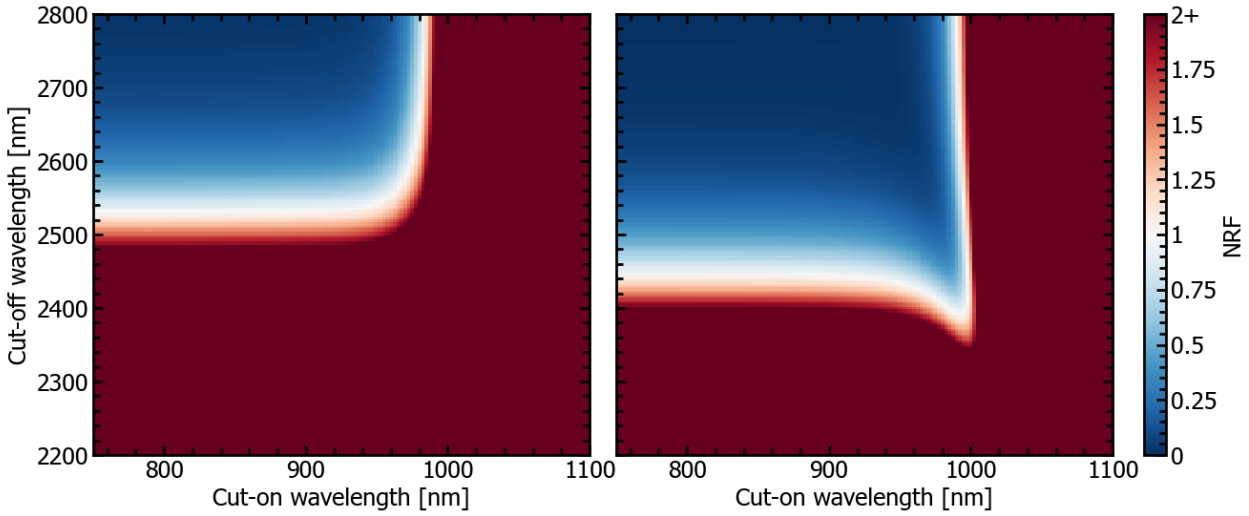

Figure 5.15 NRF (left: eq. (2.60); right: eq. (2.61)) as a function of detector bandwidth.

GaAs detectors around 1650 nm [210], and while InGaAs detectors with a cut-off wavelength extended up to 2550 nm are readily available [211], they also come with an increased cut-on wavelength that is longer than the 990 nm limit found here. A potential solution to this issue would be to spectrally split the BTBs with e.g. a dispersive prism toward multiple InGaAs detectors with different, optimized detection bandwidths [211]. An alternative would be to use a detector based on a different material with a sufficiently broad detection bandwidth. The only reported detectors with such capabilities are based on HgCdTe (e.g. [212]), which claim a quantum efficiency of over 70 % over the entire bandwidth required, with the only downside seemingly being their prohibitive cost. The feasibility of using a HgCdTe-based device to demonstrate a quantum advantage via the NRF is explored in the following section.

5.4.2 Realistic Detection Scenarios

We now consider how the the non-unity and non-flat quantum efficiency of real detectors affect the NRF. Figure 5.16 presents a comparison between the quantum efficiency and the resulting NRF for 3 detection scenarios. All three cases only consider the quantum efficiency of the detector, and do not include e.g. Fresnel back-reflection from the exit side of the BBO crystal, reflectance of mirrors, etc. as those effects 1- are generally negligible in comparison to the losses of the detectors and 2- can be mitigated with the use anti-reflection coatings.

The first scenario is a typical non-extended InGaAs detector, as used in the direct photodetection experiments of sections 4.2.1, 4.2.2, and 4.2.4, and it serves as a reference. Those detectors cover the range from 925 nm to 1650 nm with 50 % quantum efficiency. The quan-

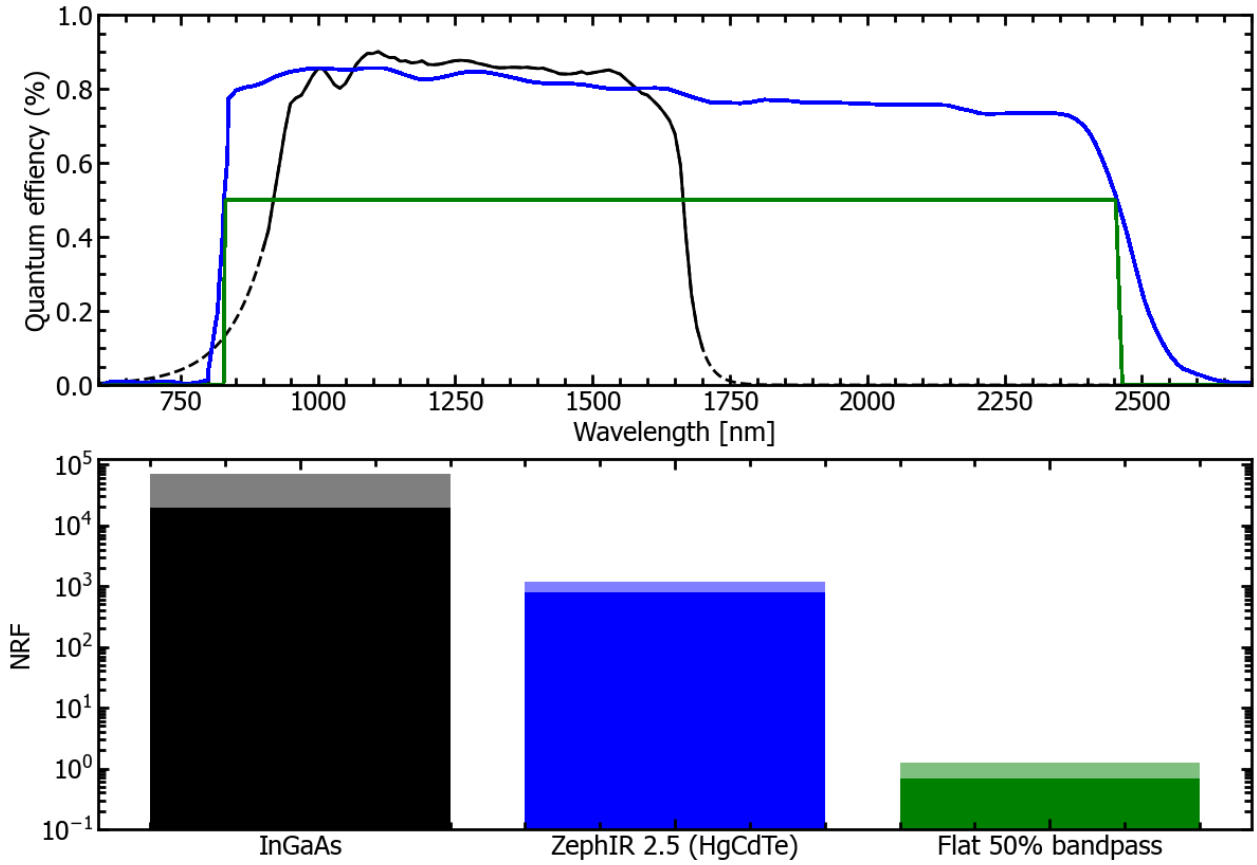

Figure 5.16 Quantum efficiency and NRF for 3 different realistic detectors.

tum efficiency curve reported by the manufacturer (solid black line) [213] is extrapolated (dashed black lines) to the full simulation grid by fitting an exponentially-decaying function to each edges of the curve. Unsurprisingly, the limited bandwidth results in NRF values (light colors: (2.60); dark colors: (2.61)) that are multiple orders of magnitude above the threshold value NRF = 1. Importantly, the NRF value predicted by this simulation is two orders of magnitude higher than the experimental value NRF = 181, indicating that the simulation overestimates either or both of the number of Schmidt modes and the optical bandwidth. Despite this discrepancy, this reference point remains useful for assessing the relative impact of a detector change.

The second scenario uses the reported quantum efficiency of the HgCdTe ZephIR 2.5 detector by Photon etc [212], which is comparable to that of the InGaAs sensor at its peak and stays above 50 % on a bandwidth ranging from 825 nm to 2450 nm. The significantly larger bandwidth indeed results in a 32× and 76× reduction of the NRF calculated respectively using equations (2.60) and (2.61). This decrease is however not enough to reach the threshold of nonclassicality, even when accounting for the lower experimental value. Since this detector

covers the entire minimal bandwidth calculated in the previous section, one must conclude that the slope of the quantum efficiency curve is now the limiting factor.

Therefore, the third and final scenario studied here is an hypothetical response-flattened version of the HgCdTe detector. The simulated response is a rectangular function

$$\eta(\lambda) = \frac{1}{2}\left(H(\lambda - \lambda_{\text{on}}) - H(\lambda - \lambda_{\text{off}})\right) \tag{5.2}$$

where λ_{on} and λ_{off} correspond to the wavelengths where the quantum efficiency of the HgCdTe detector drops to 50 %. Such a response could be attained by combining the HgCdTe detector with appropriate filters to flatten and cut the quantum efficiency (see e.g. [214] for an example of such a filter in the Si detection range). The resulting NRF indeed approaches unity for the first definition (2.60) and reaches a nonclassical value NRF = 0.7 with the second definition (2.61), confirming the need for not only broadband detection, but also a flat response.

The question is now to determine how flat the response of the detector needs to be to maintain a quantum advantage. To answer it, the NRF is recalculated by adding a slope to the otherwise flat quantum efficiency curve $\eta(\lambda)$ of the last scenario in the range $\lambda_{\text{on}} < \lambda < \lambda_{\text{off}}$, and the results are plotted in Figure 5.17. The analysis shows that the NRF is indeed quite sensitive to the slope of $\eta(\lambda)$, with the quantum advantage being preserved only if and only if

$$\left|\frac{\mathrm{d}\eta}{\mathrm{d}\lambda}\right| \leq 0.02\,\%/100\text{ nm}$$

which is on par with the reflectivity fluctuations of state-of-the-art broadband dieletric filters (e.g. [215]), albeit on a much larger bandwidth. This result leads to the conclusion that the implementation of this solution is possible though technically difficult. With that said, the first set of simulations also indicate an overestimation of the optical bandwidth and possibly also of the number of modes, and consequently the required detection bandwidth and flatness would also be overestimated. The figures presented here can therefore be reasonably interpreted as a worst-case estimation of these two parameters.

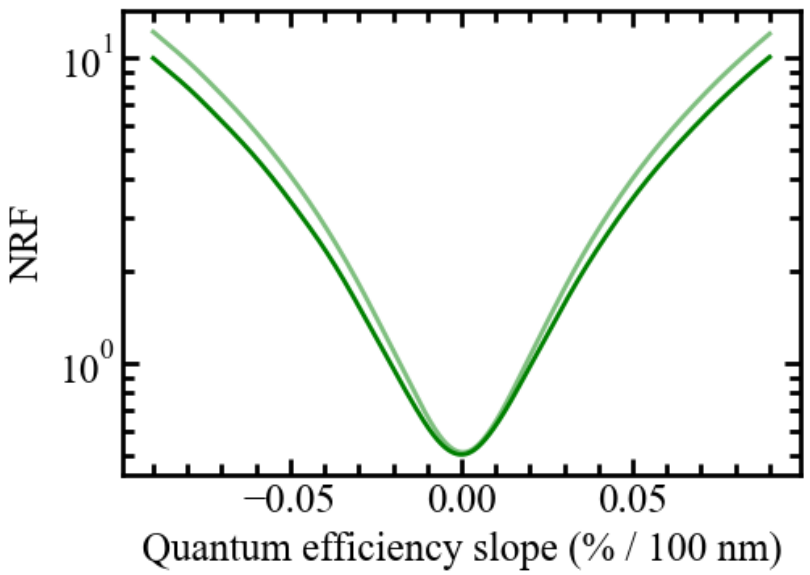

Figure 5.17 Dependence of the NRF on the slope of the quantum efficiency curve. The 0.00 point corresponds to the "flat 50% bandpass" case in Figure 5.16

CHAPTER 6 CONCLUSION

6.1 Summary of Works

In summary, the works presented in this thesis achieves nearly all of the objectives lead out in the introduction. The bright twin beams (BTBs) implementation here demonstrated operates in a previously-unexplored regime which combines 4 out the 5 ingredients identified in the introduction for an ideal source of quantum light to drive extreme nonlinear optical phenomena, making it uniquely well-positioned toward future experimental investigations of nonlinear quantum optics. Namely, the source demonstrates a macroscopic brightness $\langle n \rangle \gtrsim 10^7$, a 3.4-cycle pulse duration that could potentially be compressed down to less 2 cycles, a quasi-single spatio-temporal mode composition $K = 1.082$ that is achieved without filtering, and proof-of-principle control over the carrier-envelope phase (CEP) of the generated pulses.

The characterization results of the source also marks the demonstration of two measurements that are novel in the context of light sources driven by parametric down-conversion (PDC). First is the measurement of the pulse duration using the classical technique of frequency-resolved optical gating (FROG), which was subsequently reproduced in an experiment demonstrating high-harmonic generation in solids being driven by bright squeezed vacuum (BSV) [40]. Second is the measurement of the statistics and anti-correlation of the CEP in BTBs, which was done using a novel measurement scheme based on classical f-to-$2f$ interferometry.

Finally, a numerical simulation software here implemented models the extreme regime of nonlinear pulse propagation demonstrated in the experimental work, including the effects of diffraction, chromatic dispersion, pump depletion, and Kerr nonlinearity. This model will help the future improvement of the present BTBs implementation, notably toward achieving a demonstration of nonclassicality, as well as help in the design of novel sources operating in this new regime of bright ultrafast squeezed light.

6.2 Limitations and Suggested Solutions

The main limitation of the present work is the absence of a nonclassicality demonstration. In principle, this suggests that all the results presented here could be reproduced (and even potentially improved upon) using only classical means. The numerical analysis of Chapter 5 lead out specific criteria and potential strategies on how to adjust the experimental design

to observe nonclassicality while maintaining most, if not all of the advantageous features of the BTBs source; i.e. 1) on the generation side, the use of a diverging pump beam to cancel the detrimental effects of Kerr lensing, and 2) on the detection side, expand the bandwidth with HgCdTe-based detectors and flatten the spectral quantum efficiency curve with custom spectral filters.

Another limitation of the experimental work concerns the demonstrated CEP readout technique based on second-harmonic generation (SHG). While this scheme measures directly the CEP of the second harmonic (SH) beams and works as a proof-of-principle, the CEP of the fundamental BTBs can only be determined up to a π phase shift from this measurement. Therefore, to implement "true" CEP control via post-selection, the scheme would need to be modified as to forego the upconversion step and instead measure the Q function of the BTBs directly with a broadband local oscillator (LO) in the near infrared (NIR) that is phase-locked to the pump. With the current design, two sources could be used to generate a supercontinuum with the required frequency content : 1) the remaining energy of the noncollinear optical parametric amplifier (NOPA), which is currently used to drive the f-to-$2f$ readout of the pump CEP, or 2) the currently-unused idler beam centered at 2.1 µm generated inside the NOPA.

On the technical side, multiple improvement could be implemented relatively straightforwardly to the detection methodology. First, all spectral measurements are performed at a much lower acquisition rate than other measurements due to the electronics of the spectrometer that are used, and they also cannot accommodate simultaneous measurement of the signal and idler spectrum. Both issues could be addressed simultaneously by replacing the spectrometer with a detection scheme based on dispersive Fourier transformation [201, 202], where the spectrum is read out by stretching the pulse in time with chromatic dispersion until its time-dependent intensity can be resolved with a photodiode.

Second, the source is here operated at repetition rates of 100 kHz or lower to allow for the comparison of characterization results that are acquired with different repetition rates, as thermal effects are observed when the pulse picker is set at repetition rates of 200 kHz and higher. If *all* detection schemes could be upgraded to accommodate a 1 MHz readout, the source could be redesigned to work at the full repetition rate of the main laser system, i.e. while accounting for the thermal effects. This would enable faster acquisition of statistical samples and a lower relative contribution of low-frequency technical noise sources to the measured statistics.

Third and last, the large shot-to-shot fluctuations of the photon number of the source impose operating it with a mean photon number that is often close to the noise floor of detectors,

in order to avoid that intense events cause saturation. The use of specialized high-dynamic range detectors can alleviate this issue to some degree, but a more direct solution to this problem would be to implement detection scheme with a logarithmic response (e.g. [216]) to reduce the dynamic range required to fully resolve the fluctuations.

Finally, on the numerical side, the predictive power of the numerical model would significantly improve is the assumed Gaussian shape of the beam was replaced with a detailed experimental characterization of the pump wavefront (e.g. with a Shack–Hartmann wavefront sensor [217, 218]), which affects both the peak intensity of the pump and its transverse extent and might therefore explain some discrepancies between experiments and simulations. The predictive power is also limited by the relative slowness of its software implementation, which takes around 26h to simulate only 1000 laser shots on a desktop RTX 2060 GPU, preventing precise determination of statistical moments. Some speed gains might be achieved from the writing of custom CUDA code rather than relying on the cupy Python library which is bound to come with some amount of overhead. Another possibility would be run different levels of approximations (e.g. undepleted pump, negligible $\chi^{(3)}$, etc.) throughout the propagation to reduce the number of calculations wherever possible.

6.3 Future Research

Beyond the application of extreme nonlinear optics this work is targeting, the source here implemented can directly find other applications in quantum metrology where bright squeezed light shines. Potential uses include electro-optic sampling, where photon-number difference squeezing can be leveraged either directly to achieve sub-shot-noise detection [219], or in post-selection schemes to extract higher-order statistical moments of the fluctuating electric field [32]. Another straightforward application is in femtosecond covariance spectroscopy [220], where the inherent shot-to-shot fluctuations of the BTBs could be leveraged to passively scan the nonlinear response of materials [40] without the added complexity of a programmable pulse shaper.

Going beyond the implementation here demonstrated, the insights learned in this research can be directly applied to the development of new sources of ultrfast BTBs and BSV. Notably, a two-color BTBs source was built by the author leveraging the understanding built in this work in collaboration with the Chekhova and Tani research groups of the Max Planck Institute for the Science of Light [71], as part of a post-graduate internship for the QSciTech program[1]. This source is now being upgraded by another student toward driving ultrafast electron

[1] `http://www.qscitech.ca/fr/programme/description-detaillee/`

tunneling in nanostructures [50, 221].

Turning next to the FROG measurement here demonstrated, an interesting research avenue would be to upgrade the readout from an averaged, multi-laser-shot measurement to a single-shot-resolved measurement combined with a simultaneous determination of the relative mode composition from the optical spectrum. This way, the contribution of each temporal modes to the overall FROG trace could be separated, enabling potentially for the retrieval of a temporal analogue of the joint spectral intensity (JSI). This change would also help extend the technique toward application to few-mode PDC sources.

Then, another interesting exploration would be to see if the scheme here demonstrated to measure fluctuations of the CEP could also be used to retrieve shot-to-shot fluctuations of higher-order components of the spectral phase, i.e. the group delay, the group-delay dispersion, and so forth. In principle, the present scheme can already do so from a simple change of the numerical analysis, i.e. by extracting not only the fringe phase, but also fluctuations of the fringe frequency, its chirp, etc., but this idea has not been tested yet.

Finally, the numerical model here implemented could be leveraged toward new investigations aimed at uncovering novel forms of entanglement that might appear in ultrafast BTBs, linking e.g. the pulse amplitude with its group-delay [222]. The model is not only uniquely suited to simulate this novel regime of PDC, but the semi-classical strategy that it uses naturally reproduce the shot-by-shot data acquisition of experiments, helping toward experimental validation of such predictions.

REFERENCES

[1] T. H. Maiman, "Stimulated Optical Radiation in Ruby," *Nature*, vol. 187, no. 4736, pp. 493–494, Aug. 1960, publisher: Nature Publishing Group. [Online]. Available: https://www.nature.com/articles/187493a0

[2] K. C. Kao and G. A. Hockham, "Dielectric-fibre surface waveguides for optical frequencies," in *Proceedings of the Institution of Electrical Engineers*, vol. 113. IET, 1966, pp. 1151–1158, issue: 7.

[3] N. J. Woodland and S. Bernard, "Classifying apparatus and method," US Patent US2 612 994A, Oct., 1952. [Online]. Available: https://patents.google.com/patent/US2612994A/en?oq=U.S.+Patent+2%2c612%2c994+(1952):+%22Classifying+Apparatus+and+Method%22

[4] J. T. Russell, "Analog to digital to optical photographic recording and playback system," US Patent US3 501 586A, Mar., 1970. [Online]. Available: https://patents.google.com/patent/US3501586A/en?oq=+US+3%2c501%2c586

[5] N. Mehendale and S. Neoge, "Review on lidar technology," *Available at SSRN 3604309*, 2020.

[6] J. L. Bromberg, *The laser in America, 1950-1970*. MIT press, 1991.

[7] B. Azadgoli and R. Y. Baker, "Laser applications in surgery," *Annals of translational medicine*, vol. 4, no. 23, p. 452, 2016.

[8] M. Tse *et al.*, "Quantum-Enhanced Advanced LIGO Detectors in the Era of Gravitational-Wave Astronomy," *Physical Review Letters*, vol. 123, no. 23, p. 231107, Dec. 2019. [Online]. Available: https://link.aps.org/doi/10.1103/PhysRevLett.123.231107

[9] J. C. Maxwell, "Viii. a dynamical theory of the electromagnetic field," *Philosophical transactions of the Royal Society of London*, no. 155, pp. 459–512, 1865.

[10] M. K. E. L. Planck, "Über eine Verbesserung der Wienschen Spectralgleichung," *Verhandl. Dtsc. Phys. Ges.*, vol. 2, p. 202, 1900.

[11] M. K. E. L. Planck, "Über das Gesetz der Energieverteilung in Normalspectrum," *Ann. Phys.(Leipzig)*, vol. 4, p. 553, 1901.

[12] A. Einstein, "Über einen die Erzeugung und Verwandlung des Lichtes betreffenden heuristischen Gesichtspunkt," 1905.

[13] J. S. Bell, "On the einstein podolsky rosen paradox," *Physics Physique Fizika*, vol. 1, no. 3, p. 195, 1964.

[14] A. Aspect, J. Dalibard, and G. Roger, "Experimental test of bell's inequalities using time-varying analyzers," *Physical review letters*, vol. 49, no. 25, p. 1804, 1982.

[15] N. Gisin *et al.*, "Quantum cryptography," *Reviews of modern physics*, vol. 74, no. 1, p. 145, 2002.

[16] S. Barz, "Quantum computing with photons: introduction to the circuit model, the one-way quantum computer, and the fundamental principles of photonic experiments," *Journal of Physics B: Atomic, Molecular and Optical Physics*, vol. 48, no. 8, p. 083001, 2015.

[17] C. K. Hong and L. Mandel, "Experimental realization of a localized one-photon state," *Phys. Rev. Lett.*, vol. 56, no. 1, pp. 58–60, Jan. 1986. [Online]. Available: https://link.aps.org/doi/10.1103/PhysRevLett.56.58

[18] P. Grangier, G. Roger, and A. Aspect, "Experimental evidence for a photon anticorrelation effect on a beam splitter: a new light on single-photon interferences," *Europhysics Letters*, vol. 1, no. 4, p. 173, 1986.

[19] J. Laurat *et al.*, "Conditional Preparation of a Quantum State in the Continuous Variable Regime: Generation of a sub-Poissonian State from Twin Beams," *Physical Review Letters*, vol. 91, no. 21, p. 213601, Nov. 2003. [Online]. Available: https://link.aps.org/doi/10.1103/PhysRevLett.91.213601

[20] G. Harder *et al.*, "Single-Mode Parametric-Down-Conversion States with 50 Photons as a Source for Mesoscopic Quantum Optics," *Physical Review Letters*, vol. 116, no. 14, p. 143601, Apr. 2016. [Online]. Available: https://link.aps.org/doi/10.1103/PhysRevLett.116.143601

[21] T. S. Iskhakov *et al.*, "Heralded source of bright multi-mode mesoscopic sub-Poissonian light," *Optics Letters*, vol. 41, no. 10, p. 2149, May 2016. [Online]. Available: https://www.osapublishing.org/abstract.cfm?URI=ol-41-10-2149

[22] T. S. Iskhakov *et al.*, "Superbunched bright squeezed vacuum state," *Opt. Lett., OL*, vol. 37, no. 11, pp. 1919–1921, Jun. 2012, publisher: Optica Publishing Group. [Online]. Available: https://opg.optica.org/ol/abstract.cfm?uri=ol-37-11-1919

[23] M. Chekhova, G. Leuchs, and M. Żukowski, "Bright squeezed vacuum: Entanglement of macroscopic light beams," *Optics Communications*, vol. 337, pp. 27–43, Feb. 2015. [Online]. Available: https://linkinghub.elsevier.com/retrieve/pii/S0030401814006695

[24] A. M. Pérez *et al.*, "Giant narrowband twin-beam generation along the pump-energy propagation direction," *Nat Commun*, vol. 6, no. 1, p. 7707, Jul. 2015. [Online]. Available: https://www.nature.com/articles/ncomms8707

[25] K. Y. Spasibko *et al.*, "Multiphoton Effects Enhanced due to Ultrafast Photon-Number Fluctuations," *Phys. Rev. Lett.*, vol. 119, no. 22, p. 223603, Nov. 2017, publisher: American Physical Society. [Online]. Available: https://link.aps.org/doi/10.1103/PhysRevLett.119.223603

[26] M. Manceau *et al.*, "Indefinite-Mean Pareto Photon Distribution from Amplified Quantum Noise," *Phys. Rev. Lett.*, vol. 123, no. 12, p. 123606, Sep. 2019, publisher: American Physical Society. [Online]. Available: https://link.aps.org/doi/10.1103/PhysRevLett.123.123606

[27] A. V. Rasputnyi *et al.*, "Cascaded frequency up-conversion of bright squeezed vacuum: spectral and correlation properties," *Optics Letters*, vol. 47, no. 4, pp. 766–769, 2022.

[28] J. Aasi *et al.*, "Enhanced sensitivity of the LIGO gravitational wave detector by using squeezed states of light," *Nature Photonics*, vol. 7, no. 8, pp. 613–619, Aug. 2013. [Online]. Available: http://www.nature.com/articles/nphoton.2013.177

[29] G. Brida, M. Genovese, and I. Ruo Berchera, "Experimental realization of sub-shot-noise quantum imaging," *Nature Photon*, vol. 4, no. 4, pp. 227–230, Apr. 2010. [Online]. Available: https://www.nature.com/articles/nphoton.2010.29

[30] N. Samantaray *et al.*, "Realization of the first sub-shot-noise wide field microscope," *Light Sci Appl*, vol. 6, no. 7, pp. e17 005–e17 005, Jan. 2017. [Online]. Available: https://www.nature.com/articles/lsa20175

[31] S. T. Pradyumna *et al.*, "Twin beam quantum-enhanced correlated interferometry for testing fundamental physics," *Commun Phys*, vol. 3, no. 1, p. 104, Jun. 2020. [Online]. Available: https://www.nature.com/articles/s42005-020-0368-5

[32] S. Virally, P. Cusson, and D. V. Seletskiy, "Enhanced Electro-optic Sampling with Quantum Probes," *Phys. Rev. Lett.*, vol. 127, no. 27, p. 270504, Dec. 2021. [Online]. Available: https://link.aps.org/doi/10.1103/PhysRevLett.127.270504

[33] T. Li *et al.*, "Quantum-enhanced stimulated Brillouin scattering spectroscopy and imaging," *Optica*, vol. 9, no. 8, p. 959, Aug. 2022. [Online]. Available: https://opg.optica.org/abstract.cfm?URI=optica-9-8-959

[34] M. Even Tzur *et al.*, "Photon-statistics force in ultrafast electron dynamics," *Nat. Photon.*, vol. 17, no. 6, pp. 501–509, Jun. 2023, publisher: Nature Publishing Group. [Online]. Available: https://www.nature.com/articles/s41566-023-01209-w

[35] A. Gorlach *et al.*, "High-harmonic generation driven by quantum light," *Nat. Phys.*, vol. 19, no. 11, pp. 1689–1696, Nov. 2023, publisher: Nature Publishing Group. [Online]. Available: https://www.nature.com/articles/s41567-023-02127-y

[36] M. Even Tzur and O. Cohen, "Motion of charged particles in bright squeezed vacuum," *Light Sci Appl*, vol. 13, no. 1, p. 41, Feb. 2024, publisher: Nature Publishing Group. [Online]. Available: https://www.nature.com/articles/s41377-024-01381-w

[37] J. Heimerl *et al.*, "Multiphoton electron emission with non-classical light," *Nat. Phys.*, vol. 20, no. 6, pp. 945–950, Jun. 2024, publisher: Nature Publishing Group. [Online]. Available: https://www.nature.com/articles/s41567-024-02472-6

[38] M. E. Tzur *et al.*, "Generation of squeezed high-order harmonics," *Phys. Rev. Res.*, vol. 6, no. 3, p. 033079, Jul. 2024, publisher: American Physical Society. [Online]. Available: https://link.aps.org/doi/10.1103/PhysRevResearch.6.033079

[39] R. Yanagimoto *et al.*, "Mesoscopic ultrafast nonlinear optics—the emergence of multimode quantum non-Gaussian physics," *Optica, OPTICA*, vol. 11, no. 7, pp. 896–918, Jul. 2024, publisher: Optica Publishing Group. [Online]. Available: https://opg.optica.org/optica/abstract.cfm?uri=optica-11-7-896

[40] A. Rasputnyi *et al.*, "High-harmonic generation by a bright squeezed vacuum," *Nat. Phys.*, vol. 20, no. 12, pp. 1960–1965, Dec. 2024, publisher: Nature Publishing Group. [Online]. Available: https://www.nature.com/articles/s41567-024-02659-x

[41] M. E. Tzur *et al.*, "Measuring and controlling the birth of quantum attosecond pulses," *arXiv preprint arXiv:2502.09427*, 2025.

[42] S. Lemieux *et al.*, "Photon bunching in high-harmonic emission controlled by quantum light," *Nat. Photon.*, pp. 1–5, May 2025, publisher: Nature Publishing Group. [Online]. Available: https://www.nature.com/articles/s41566-025-01673-6

[43] A. Gorlach *et al.*, "The quantum-optical nature of high harmonic generation," *Nature communications*, vol. 11, no. 1, p. 4598, 2020.

[44] L. Cruz-Rodriguez *et al.*, "Quantum phenomena in attosecond science," *Nature Reviews Physics*, vol. 6, no. 11, pp. 691–704, 2024.

[45] H. R. Telle *et al.*, "Carrier-envelope offset phase control: A novel concept for absolute optical frequency measurement and ultrashort pulse generation," *Applied Physics B*, vol. 69, pp. 327–332, 1999.

[46] F. Krausz *et al.*, "Extreme nonlinear optics: Exposing matter to a few periods of light," *Optics and Photonics News*, vol. 9, no. 7, pp. 46–51, 1998.

[47] G. Paulus *et al.*, "Absolute-phase phenomena in photoionization with few-cycle laser pulses," *Nature*, vol. 414, no. 6860, pp. 182–184, 2001.

[48] A. Baltuška, T. Fuji, and T. Kobayashi, "Controlling the Carrier-Envelope Phase of Ultrashort Light Pulses with Optical Parametric Amplifiers," *Phys. Rev. Lett.*, vol. 88, no. 13, p. 133901, Mar. 2002, publisher: American Physical Society. [Online]. Available: https://link.aps.org/doi/10.1103/PhysRevLett.88.133901

[49] A. Baltuška *et al.*, "Attosecond control of electronic processes by intense light fields," *Nature*, vol. 421, no. 6923, pp. 611–615, 2003.

[50] T. Rybka *et al.*, "Sub-cycle optical phase control of nanotunnelling in the single-electron regime," *Nature Photonics*, vol. 10, no. 10, pp. 667–670, 2016.

[51] D. C. Burnham and D. L. Weinberg, "Observation of Simultaneity in Parametric Production of Optical Photon Pairs," *Phys. Rev. Lett.*, vol. 25, no. 2, pp. 84–87, Jul. 1970, publisher: American Physical Society. [Online]. Available: https://link.aps.org/doi/10.1103/PhysRevLett.25.84

[52] A. S. Moskalenko *et al.*, "Paraxial Theory of Direct Electro-optic Sampling of the Quantum Vacuum," *Physical Review Letters*, vol. 115, no. 26, p. 263601, Dec. 2015. [Online]. Available: https://link.aps.org/doi/10.1103/PhysRevLett.115.263601

[53] C. Riek *et al.*, "Direct sampling of electric-field vacuum fluctuations," *Science*, vol. 350, no. 6259, pp. 420–423, Oct. 2015. [Online]. Available: https://www.science.org/doi/10.1126/science.aac9788

[54] C. Couteau, "Spontaneous parametric down-conversion," *Contemporary Physics*, vol. 59, no. 3, pp. 291–304, 2018. [Online]. Available: https://doi.org/10.1080/00107514.2018.1488463

[55] I.-C. Benea-Chelmus *et al.*, "Electric field correlation measurements on the electromagnetic vacuum state," *Nature*, vol. 568, no. 7751, pp. 202–206, Apr. 2019. [Online]. Available: http://arxiv.org/abs/1809.01785

[56] B. E. Saleh and M. C. Teich, *Fundamentals of photonics*. Wiley New York, 2008, vol. 332.

[57] R. W. Boyd, *Nonlinear Optics*, Mar. 2020. [Online]. Available: https://shop.elsevier.com/books/nonlinear-optics/boyd/978-0-12-811002-7

[58] G. Vampa *et al.*, "Plasmon-enhanced high-harmonic generation from silicon," *Nature Physics*, vol. 13, no. 7, pp. 659–662, 2017.

[59] M. Hentschel *et al.*, "Attosecond metrology," *Nature*, vol. 414, no. 6863, pp. 509–513, Nov. 2001, publisher: Nature Publishing Group. [Online]. Available: https://www.nature.com/articles/35107000

[60] C. Manzoni *et al.*, "Optical-parametric-generation process driven by femtosecond pulses: Timing and carrier-envelope phase properties," *Physical Review A*, vol. 79, no. 3, p. 033818, Mar. 2009. [Online]. Available: https://link.aps.org/doi/10.1103/PhysRevA.79.033818

[61] K. Garay-Palmett *et al.*, "Photon pair-state preparation with tailored spectral properties by spontaneous four-wave mixing in photonic-crystal fiber," *Optics express*, vol. 15, no. 22, pp. 14 870–14 886, 2007.

[62] A. Eckstein *et al.*, "Highly Efficient Single-Pass Source of Pulsed Single-Mode Twin Beams of Light," *Phys. Rev. Lett.*, vol. 106, no. 1, p. 013603, Jan. 2011, publisher: American Physical Society. [Online]. Available: https://link.aps.org/doi/10.1103/PhysRevLett.106.013603

[63] M. A. Finger *et al.*, "Characterization and shaping of the time-frequency Schmidt mode spectrum of bright twin beams generated in gas-filled hollow-core photonic crystal fibers," *Phys. Rev. A*, vol. 95, no. 5, p. 053814, May 2017, publisher: American Physical Society. [Online]. Available: https://link.aps.org/doi/10.1103/PhysRevA.95.053814

[64] N. Quesada and A. M. Brańczyk, "Gaussian functions are optimal for waveguided nonlinear-quantum-optical processes," *Physical Review A*, vol. 98, no. 4, p. 043813, 2018.

[65] A. Allevi, S. Olivares, and M. Bondani, "Measuring high-order photon-number correlations in experiments with multimode pulsed quantum states," *Phys. Rev. A*, vol. 85, no. 6, p. 063835, Jun. 2012. [Online]. Available: https://link.aps.org/doi/10.1103/PhysRevA.85.063835

[66] F. Paleari *et al.*, "Thermal photon statistics in spontaneous parametric downconversion," *Optics Express*, vol. 12, no. 13, p. 2816, Jun. 2004. [Online]. Available: https://www.osapublishing.org/abstract.cfm?URI=oe-12-13-2816

[67] A. Agliati *et al.*, "Quantum and classical correlations of intense beams of light investigated via joint photodetection," *Journal of Optics B: Quantum and Semiclassical Optics*, vol. 7, no. 12, pp. S652–S663, Dec. 2005. [Online]. Available: https://iopscience.iop.org/article/10.1088/1464-4266/7/12/031

[68] I. N. Agafonov, M. V. Chekhova, and G. Leuchs, "Two-color bright squeezed vacuum," *Physical Review A—Atomic, Molecular, and Optical Physics*, vol. 82, no. 1, p. 011801, 2010.

[69] M. V. Chekhova *et al.*, "Broadband bright twin beams and their upconversion," *Optics letters*, vol. 43, no. 3, pp. 375–378, 2018.

[70] J. Flórez, J. S. Lundeen, and M. V. Chekhova, "Pump depletion in parametric down-conversion with low pump energies," *Optics Letters*, vol. 45, no. 15, pp. 4264–4267, 2020.

[71] P. Cusson *et al.*, "Ultrafast Bright Squeezed Vacuum in Nearly Single Spatio-Temporal Mode," in *CLEO 2024 (2024), paper FTh1M.5.* Optica Publishing Group, May 2024, p. FTh1M.5. [Online]. Available: https://opg.optica.org/abstract.cfm?uri=CLEO_FS-2024-FTh1M.5

[72] P. Cusson, S. Virally, and D. Seletskiy, "Generation of single-mode few-cycle twin beams for time-domain quantum optics," in *2023 Photonics North (PN).* IEEE, 2023, pp. 1–2.

[73] A. M. Pérez *et al.*, "Bright squeezed-vacuum source with 1.1 spatial mode," *Opt. Lett.*, vol. 39, no. 8, p. 2403, Apr. 2014. [Online]. Available: https://opg.optica.org/abstract.cfm?URI=ol-39-8-2403

[74] M. A. Finger *et al.*, "Raman-free, noble-gas-filled photonic-crystal fiber source for ultrafast, very bright twin-beam squeezed vacuum," *Physical review letters*, vol. 115, no. 14, p. 143602, 2015.

[75] T. S. Iskhakov *et al.*, "Low-noise macroscopic twin beams," *Physical Review A*, vol. 93, no. 4, p. 043849, Apr. 2016. [Online]. Available: https://link.aps.org/doi/10.1103/PhysRevA.93.043849

[76] P. F. Moulton, "Spectroscopic and laser characteristics of Ti:Al_2O_3," *J. Opt. Soc. Am. B, JOSAB*, vol. 3, no. 1, pp. 125–133, Jan. 1986, publisher: Optica Publishing Group. [Online]. Available: https://opg.optica.org/josab/abstract.cfm?uri=josab-3-1-125

[77] R. R. Alfano and S. L. Shapiro, "Emission in the Region 4000 to 7000 å Via Four-Photon Coupling in Glass," *Phys. Rev. Lett.*, vol. 24, no. 11, pp. 584–587, Mar. 1970, publisher: American Physical Society. [Online]. Available: https://link.aps.org/doi/10.1103/PhysRevLett.24.584

[78] R. R. Alfano and S. L. Shapiro, "Observation of Self-Phase Modulation and Small-Scale Filaments in Crystals and Glasses," *Phys. Rev. Lett.*, vol. 24, no. 11, pp. 592–594, Mar. 1970, publisher: American Physical Society. [Online]. Available: https://link.aps.org/doi/10.1103/PhysRevLett.24.592

[79] M. Kolesik, J. Moloney, and M. Mlejnek, "Unidirectional optical pulse propagation equation," *Physical review letters*, vol. 89, no. 28, p. 283902, 2002.

[80] S. Akturk *et al.*, "Spatio-temporal couplings in ultrashort laser pulses," *J. Opt.*, vol. 12, no. 9, p. 093001, Sep. 2010. [Online]. Available: https://iopscience.iop.org/article/10.1088/2040-8978/12/9/093001

[81] E. Treacy, "Optical pulse compression with diffraction gratings," *IEEE Journal of Quantum Electronics*, vol. 5, no. 9, pp. 454–458, Sep. 1969. [Online]. Available: https://ieeexplore.ieee.org/abstract/document/1076303

[82] R. L. Fork, O. E. Martinez, and J. P. Gordon, "Negative dispersion using pairs of prisms," *Opt. Lett., OL*, vol. 9, no. 5, pp. 150–152, May 1984, publisher: Optica Publishing Group. [Online]. Available: https://opg.optica.org/ol/abstract.cfm?uri=ol-9-5-150

[83] A. M. Weiner, J. P. Heritage, and E. M. Kirschner, "High-resolution femtosecond pulse shaping," *J. Opt. Soc. Am. B, JOSAB*, vol. 5, no. 8, pp. 1563–

1572, Aug. 1988, publisher: Optica Publishing Group. [Online]. Available: https://opg.optica.org/josab/abstract.cfm?uri=josab-5-8-1563

[84] R. Szipöcs *et al.*, "Chirped multilayer coatings for broadband dispersion control in femtosecond lasers," *Opt. Lett., OL*, vol. 19, no. 3, pp. 201–203, Feb. 1994, publisher: Optica Publishing Group. [Online]. Available: https://opg.optica.org/ol/abstract.cfm?uri=ol-19-3-201

[85] J. A. Armstrong *et al.*, "Interactions between Light Waves in a Nonlinear Dielectric," *Phys. Rev.*, vol. 127, no. 6, pp. 1918–1939, Sep. 1962, publisher: American Physical Society. [Online]. Available: https://link.aps.org/doi/10.1103/PhysRev.127.1918

[86] D. E. Zelmon, D. L. Small, and D. Jundt, "Infrared corrected Sellmeier coefficients for congruently grown lithium niobate and 5 mol% magnesium oxide –doped lithium niobate," *J. Opt. Soc. Am. B*, vol. 14, no. 12, p. 3319, Dec. 1997. [Online]. Available: https://opg.optica.org/abstract.cfm?URI=josab-14-12-3319

[87] G. Tamošauskas *et al.*, "Transmittance and phase matching of BBO crystal in the 3-5 um range and its application for the characterization of mid-infrared laser pulses," *Opt. Mater. Express*, vol. 8, no. 6, p. 1410, Jun. 2018. [Online]. Available: https://opg.optica.org/abstract.cfm?URI=ome-8-6-1410

[88] V. Loriot *et al.*, "Measurement of high order kerr refractive index of major air components," *Optics express*, vol. 17, no. 16, pp. 13 429–13 434, 2009.

[89] G. A. Askar'yan, "Effects of the gradient of a strong electromagnetic beam on electrons and atoms," *Sov. Phys. JETP*, vol. 15, no. 6, pp. 1088–1090, 1962.

[90] R. Y. Chiao, E. Garmire, and C. H. Townes, "Self-Trapping of Optical Beams," *Phys. Rev. Lett.*, vol. 13, no. 15, pp. 479–482, Oct. 1964, publisher: American Physical Society. [Online]. Available: https://link.aps.org/doi/10.1103/PhysRevLett.13.479

[91] L. F. Mollenauer, R. H. Stolen, and J. P. Gordon, "Experimental Observation of Picosecond Pulse Narrowing and Solitons in Optical Fibers," *Phys. Rev. Lett.*, vol. 45, no. 13, pp. 1095–1098, Sep. 1980. [Online]. Available: https://link.aps.org/doi/10.1103/PhysRevLett.45.1095

[92] J. Valdmanis, G. Mourou, and C. Gabel, "Subpicosecond electrical sampling," *IEEE Journal of Quantum Electronics*, vol. 19, no. 4, pp. 664–667, Apr. 1983. [Online]. Available: http://ieeexplore.ieee.org/document/1071915/

[93] Q. Wu and X. Zhang, "Free-space electro-optic sampling of terahertz beams," *Applied Physics Letters*, vol. 67, no. 24, pp. 3523–3525, Dec. 1995. [Online]. Available: http://aip.scitation.org/doi/10.1063/1.114909

[94] Q. Wu and X.-C. Zhang, "Free-space electro-optics sampling of mid-infrared pulses," *Applied Physics Letters*, vol. 71, no. 10, pp. 1285–1286, Sep. 1997. [Online]. Available: http://aip.scitation.org/doi/10.1063/1.119873

[95] C. Riek *et al.*, "Subcycle quantum electrodynamics," *Nature*, vol. 541, no. 7637, pp. 376–379, Jan. 2017. [Online]. Available: http://www.nature.com/articles/nature21024

[96] A. Grupp *et al.*, "Broadly tunable ultrafast pump-probe system operating at multi-kHz repetition rate," *Journal of Optics*, vol. 20, no. 1, p. 014005, Jan. 2018. [Online]. Available: https://iopscience.iop.org/article/10.1088/2040-8986/aa9b07

[97] J. F. Lippmann *et al.*, "Laser cooling of semiconductors traced in the time domain," in *Conference on Lasers and Electro-Optics (2019), paper FW4M.3.* Optical Society of America, May 2019, p. FW4M.3. [Online]. Available: https://www.osapublishing.org/abstract.cfm?uri=CLEO_QELS-2019-FW4M.3

[98] A. S. Kowligy *et al.*, "Infrared electric field sampled frequency comb spectroscopy," *SCIENCE ADVANCES*, p. 8, 2019.

[99] I. Pupeza *et al.*, "Field-resolved infrared spectroscopy of biological systems," *Nature*, vol. 577, no. 7788, pp. 52–59, Jan. 2020. [Online]. Available: http://www.nature.com/articles/s41586-019-1850-7

[100] S. Lischke *et al.*, "Ultra-fast germanium photodiode with 3-db bandwidth of 265 ghz," *Nature Photonics*, vol. 15, no. 12, pp. 925–931, 2021.

[101] R. Trebino *et al.*, "Highly reliable measurement of ultrashort laser pulses," *Journal of Applied Physics*, vol. 128, no. 17, 2020.

[102] E. J. Akutowicz, "On the determination of the phase of a fourier integral, i," *Transactions of the American Mathematical Society*, vol. 83, no. 1, pp. 179–192, 1956.

[103] E. J. Akutowicz, "On the determination of the phase of a fourier integral, ii," *Proceedings of the American Mathematical Society*, vol. 8, no. 2, pp. 234–238, 1957.

[104] D. J. Kane and R. Trebino, "Measuring the intensity and phase of a femtosecond pulse using spectrally resolved self-diffraction," in *OSA Annual Meeting.* Optica Publishing Group, 1991, p. PD36.

[105] D. Kane and R. Trebino, "Characterization of arbitrary femtosecond pulses using frequency-resolved optical gating," *IEEE Journal of Quantum Electronics*, vol. 29, no. 2, pp. 571–579, Feb. 1993. [Online]. Available: https://ieeexplore.ieee.org/abstract/document/199311

[106] R. Trebino and D. J. Kane, "Using phase retrieval to measure the intensity and phase of ultrashort pulses: frequency-resolved optical gating," *J. Opt. Soc. Am. A, JOSAA*, vol. 10, no. 5, pp. 1101–1111, May 1993, publisher: Optica Publishing Group. [Online]. Available: https://opg.optica.org/josaa/abstract.cfm?uri=josaa-10-5-1101

[107] K. W. DeLong *et al.*, "Frequency-resolved optical gating with the use of second-harmonic generation," *J. Opt. Soc. Am. B, JOSAB*, vol. 11, no. 11, pp. 2206–2215, Nov. 1994, publisher: Optica Publishing Group. [Online]. Available: https://opg.optica.org/josab/abstract.cfm?uri=josab-11-11-2206

[108] K. W. DeLong *et al.*, "Pulse retrieval in frequency-resolved optical gating based on the method of generalized projections," *Opt. Lett., OL*, vol. 19, no. 24, pp. 2152–2154, Dec. 1994, publisher: Optica Publishing Group. [Online]. Available: https://opg.optica.org/ol/abstract.cfm?uri=ol-19-24-2152

[109] D. Kane, "Real-time measurement of ultrashort laser pulses using principal component generalized projections," *IEEE Journal of Selected Topics in Quantum Electronics*, vol. 4, no. 2, pp. 278–284, Mar. 1998. [Online]. Available: https://ieeexplore.ieee.org/abstract/document/686733

[110] P. Sidorenko *et al.*, "Ptychographic reconstruction algorithm for frequency-resolved optical gating: super-resolution and supreme robustness," *Optica, OPTICA*, vol. 3, no. 12, pp. 1320–1330, Dec. 2016, publisher: Optica Publishing Group. [Online]. Available: https://opg.optica.org/optica/abstract.cfm?uri=optica-3-12-1320

[111] T. Zahavy *et al.*, "Deep learning reconstruction of ultrashort pulses," *Optica, OPTICA*, vol. 5, no. 5, pp. 666–673, May 2018, publisher: Optica Publishing Group. [Online]. Available: https://opg.optica.org/optica/abstract.cfm?uri=optica-5-5-666

[112] R. Jafari, T. Jones, and R. Trebino, "100% reliable algorithm for second-harmonic-generation frequency-resolved optical gating," *Opt. Express*, vol. 27, no. 3, p. 2112, Feb. 2019. [Online]. Available: https://opg.optica.org/abstract.cfm?URI=oe-27-3-2112

[113] N. C. Geib *et al.*, "Common pulse retrieval algorithm: a fast and universal method to retrieve ultrashort pulses," *Optica*, vol. 6, no. 4, p. 495, Apr. 2019. [Online]. Available: https://opg.optica.org/abstract.cfm?URI=optica-6-4-495

[114] T. Bendory, P. Sidorenko, and Y. C. Eldar, "On the Uniqueness of FROG Methods," *IEEE Signal Processing Letters*, vol. 24, no. 5, pp. 722–726, May 2017. [Online]. Available: https://ieeexplore.ieee.org/document/7891012

[115] J. Ratner *et al.*, "Coherent artifact in modern pulse measurements," *Opt. Lett.*, vol. 37, no. 14, p. 2874, Jul. 2012. [Online]. Available: https://opg.optica.org/abstract.cfm?URI=ol-37-14-2874

[116] M. Miranda *et al.*, "Simultaneous compression and characterization of ultrashort laser pulses using chirped mirrors and glass wedges," *Optics express*, vol. 20, no. 1, pp. 688–697, 2011.

[117] A. Leblanc *et al.*, "Phase-matching-free pulse retrieval based on transient absorption in solids," *Opt. Express, OE*, vol. 27, no. 20, pp. 28 998–29 015, Sep. 2019, publisher: Optica Publishing Group. [Online]. Available: https://opg.optica.org/oe/abstract.cfm?uri=oe-27-20-28998

[118] C. Iaconis and I. A. Walmsley, "Spectral phase interferometry for direct electric-field reconstruction of ultrashort optical pulses," *Optics letters*, vol. 23, no. 10, pp. 792–794, 1998, publisher: Optical Society of America.

[119] J. R. Birge, R. Ell, and F. X. Kärtner, "Two-dimensional spectral shearing interferometry for few-cycle pulse characterization," *Opt. Lett.*, vol. 31, no. 13, p. 2063, Jul. 2006. [Online]. Available: https://opg.optica.org/abstract.cfm?URI=ol-31-13-2063

[120] J. R. Birge, H. M. Crespo, and F. X. Kärtner, "Theory and design of two-dimensional spectral shearing interferometry for few-cycle pulse measurement," *J. Opt. Soc. Am. B, JOSAB*, vol. 27, no. 6, pp. 1165–1173, Jun. 2010, publisher: Optica Publishing Group. [Online]. Available: https://opg.optica.org/josab/abstract.cfm?uri=josab-27-6-1165

[121] F. Kärtner *et al.*, "Design and fabrication of double-chirped mirrors," *Optics letters*, vol. 22, no. 11, pp. 831–833, 1997.

[122] R. J. Glauber, "The Quantum Theory of Optical Coherence," *Phys. Rev.*, vol. 130, no. 6, pp. 2529–2539, Jun. 1963, publisher: American Physical Society. [Online]. Available: https://link.aps.org/doi/10.1103/PhysRev.130.2529

[123] Q. Zhang *et al.*, "Large scale quantum key distribution: challenges and solutions [Invited]," *Optics Express*, vol. 26, no. 18, p. 24260, Sep. 2018. [Online]. Available: https://www.osapublishing.org/abstract.cfm?URI=oe-26-18-24260

[124] M. O. Scully and M. S. Zubairy, *Quantum Optics*, 1997.

[125] M. G. Raymer and I. A. Walmsley, "Temporal modes in quantum optics: then and now," *Phys. Scr.*, vol. 95, no. 6, p. 064002, Jun. 2020. [Online]. Available: https://iopscience.iop.org/article/10.1088/1402-4896/ab6153

[126] S. Virally and B. Reulet, "Unidimensional time-domain quantum optics," *Phys. Rev. A*, vol. 100, no. 2, p. 023833, Aug. 2019. [Online]. Available: https://link.aps.org/doi/10.1103/PhysRevA.100.023833

[127] P. A. M. Dirac, "The quantum theory of the emission and absorption of radiation," *Proceedings of the Royal Society of London. Series A, Containing Papers of a Mathematical and Physical Character*, vol. 114, no. 767, pp. 243–265, 1927, publisher: The Royal Society London.

[128] L. Susskind and J. Glogower, "Quantum mechanical phase and time operator," *Physics Physique Fizika*, vol. 1, no. 1, pp. 49–61, Jul. 1964, publisher: American Physical Society. [Online]. Available: https://link.aps.org/doi/10.1103/PhysicsPhysiqueFizika.1.49

[129] H. Paul, "Phase of a Microscopic Electromagnetic Field and Its Measurement," *Fortschritte der Physik*, vol. 22, no. 11, pp. 657–689, 1974, _eprint: https://onlinelibrary.wiley.com/doi/pdf/10.1002/prop.19740221104. [Online]. Available: https://onlinelibrary.wiley.com/doi/abs/10.1002/prop.19740221104

[130] D. T. Pegg and S. M. Barnett, "Unitary Phase Operator in Quantum Mechanics," *EPL*, vol. 6, no. 6, p. 483, Jul. 1988. [Online]. Available: https://dx.doi.org/10.1209/0295-5075/6/6/002

[131] D. T. Pegg and S. M. Barnett, "Phase properties of the quantized single-mode electromagnetic field," *Phys. Rev. A*, vol. 39, no. 4, pp. 1665–1675, Feb. 1989, publisher: American Physical Society. [Online]. Available: https://link.aps.org/doi/10.1103/PhysRevA.39.1665

[132] H. B. Casimir, "On the attraction between two perfectly conducting plates," in *Proc. Kon. Ned. Akad. Wet.*, vol. 51, 1948, p. 793.

[133] W. E. Lamb and R. C. Retherford, "Fine Structure of the Hydrogen Atom by a Microwave Method," *Physical Review*, vol. 72, no. 3, pp. 241–243, Aug. 1947. [Online]. Available: https://link.aps.org/doi/10.1103/PhysRev.72.241

[134] A. Fragner *et al.*, "Resolving Vacuum Fluctuations in an Electrical Circuit by Measuring the Lamb Shift," *Science*, vol. 322, no. 5906, pp. 1357–1360, Nov. 2008. [Online]. Available: https://www.sciencemag.org/lookup/doi/10.1126/science.1164482

[135] C. M. Caves, "Quantum-mechanical noise in an interferometer," *Phys. Rev. D*, vol. 23, no. 8, pp. 1693–1708, Apr. 1981, publisher: American Physical Society. [Online]. Available: https://link.aps.org/doi/10.1103/PhysRevD.23.1693

[136] W. Heisenberg, "Über den anschaulichen inhalt der quantentheoretischen kinematik und mechanik," *Zeitschrift für Physik*, vol. 43, no. 3, pp. 172–198, 1927.

[137] R. H. Brown and R. Q. Twiss, "Correlation between Photons in two Coherent Beams of Light," *Nature*, vol. 177, no. 4497, pp. 27–29, Jan. 1956, publisher: Nature Publishing Group. [Online]. Available: https://www.nature.com/articles/177027a0

[138] H. Vahlbruch *et al.*, "Detection of 15 db squeezed states of light and their application for the absolute calibration of photoelectric quantum efficiency," *Physical review letters*, vol. 117, no. 11, p. 110801, 2016.

[139] J. Amari, J. Takai, and T. Hirano, "Highly efficient measurement of optical quadrature squeezing using a spatial light modulator controlled by machine learning," *Opt. Continuum, OPTCON*, vol. 2, no. 4, pp. 933–941, Apr. 2023, publisher: Optica Publishing Group. [Online]. Available: https://opg.optica.org/optcon/abstract.cfm?uri=optcon-2-4-933

[140] R.-D. Li and P. Kumar, "Quantum-noise reduction in traveling-wave second-harmonic generation," *Physical Review A*, vol. 49, no. 3, p. 2157, 1994.

[141] N. Quesada *et al.*, "Theory of high-gain twin-beam generation in waveguides: From Maxwell's equations to efficient simulation," *Phys. Rev. A*, vol. 102, no. 3, p. 033519, Sep. 2020, publisher: American Physical Society. [Online]. Available: https://link.aps.org/doi/10.1103/PhysRevA.102.033519

[142] K. Chinni and N. Quesada, "Beyond the parametric approximation: Pump depletion, entanglement, and squeezing in macroscopic down-conversion," *Phys. Rev. A*, vol. 110, no. 1, p. 013712, Jul. 2024, publisher: American Physical Society. [Online]. Available: https://link.aps.org/doi/10.1103/PhysRevA.110.013712

[143] K. Spasibko, "Spectral and statistical properties of high-gain parametric down-conversion," *arXiv:2007.12999 [physics, physics:quant-ph]*, Jul. 2020. [Online]. Available: http://arxiv.org/abs/2007.12999

[144] C. K. Hong, Z. Y. Ou, and L. Mandel, "Measurement of subpicosecond time intervals between two photons by interference," *Physical Review Letters*, vol. 59, no. 18, pp. 2044–2046, Nov. 1987. [Online]. Available: https://link.aps.org/doi/10.1103/PhysRevLett.59.2044

[145] O. A. Ivanova *et al.*, "Multiphoton correlations in parametric down-conversion and their measurement in the pulsed regime," *Quantum Electron.*, vol. 36, no. 10, pp. 951–956, Oct. 2006. [Online]. Available: https://iopscience.iop.org/article/10.1070/QE2006v036n10ABEH013300

[146] K. Husimi, "Some formal properties of the density matrix," *Proceedings of the Physico-Mathematical Society of Japan. 3rd Series*, vol. 22, no. 4, pp. 264–314, 1940.

[147] E. Wigner, "On the quantum correction for thermodynamic equilibrium," *Physical review*, vol. 40, no. 5, p. 749, 1932.

[148] E. Sudarshan, "Equivalence of semiclassical and quantum mechanical descriptions of statistical light beams," *Physical Review Letters*, vol. 10, no. 7, p. 277, 1963.

[149] R. J. Glauber, "Coherent and incoherent states of the radiation field," *Physical Review*, vol. 131, no. 6, p. 2766, 1963.

[150] N. Walker, "Quantum Theory of Multiport Optical Homodyning," *Journal of Modern Optics*, vol. 34, no. 1, pp. 15–60, Jan. 1987. [Online]. Available: http://www.tandfonline.com/doi/abs/10.1080/09500348714550131

[151] U. Leonhardt and H. Paul, "Simultaneous Measurements of Canonically Conjugate Variables in Quantum Optics," *Journal of Modern Optics*, vol. 40, no. 9, pp. 1745–1751, Sep. 1993. [Online]. Available: http://www.tandfonline.com/doi/abs/10.1080/09500349314551761

[152] U. Leonhardt and H. Paul, "Realistic optical homodyne measurements and quasiprobability distributions," *Phys. Rev. A*, vol. 48, no. 6, pp. 4598–4604, Dec. 1993. [Online]. Available: https://link.aps.org/doi/10.1103/PhysRevA.48.4598

[153] U. Leonhardt, B. Böhmer, and H. Paul, "Uncertainty relations for realistic joint measurements of position and momentum in quantum optics," *Optics Communications*, vol. 119, no. 3-4, pp. 296–300, Sep. 1995. [Online]. Available: https://linkinghub.elsevier.com/retrieve/pii/003040189500321X

[154] J. Shapiro and S. Wagner, "Phase and amplitude uncertainties in heterodyne detection," *IEEE J. Quantum Electron.*, vol. 20, no. 7, pp. 803–813, Jul. 1984. [Online]. Available: http://ieeexplore.ieee.org/document/1072470/

[155] M. Collett, R. Loudon, and C. Gardiner, "Quantum Theory of Optical Homodyne and Heterodyne Detection," *Journal of Modern Optics*, vol. 34, no. 6-7, pp. 881–902, Jun. 1987. [Online]. Available: http://www.tandfonline.com/doi/abs/10.1080/09500348714550811

[156] M. G. Raymer, J. Cooper, and M. Beck, "Many-port homodyne detection of an optical phase," *Phys. Rev. A*, vol. 48, no. 6, pp. 4617–4628, Dec. 1993. [Online]. Available: https://link.aps.org/doi/10.1103/PhysRevA.48.4617

[157] U. Leonhardt and H. Paul, "Phase measurement and Q function," *Phys. Rev. A*, vol. 47, no. 4, pp. R2460–R2463, Apr. 1993. [Online]. Available: https://link.aps.org/doi/10.1103/PhysRevA.47.R2460

[158] C. R. Müller *et al.*, "Evading vacuum noise: Wigner projections or husimi samples?" *Physical Review Letters*, vol. 117, no. 7, p. 070801, 2016.

[159] Y. S. Teo *et al.*, "Superiority of heterodyning over homodyning: An assessment with quadrature moments," *Physical Review A*, vol. 95, no. 4, p. 042322, 2017.

[160] D. T. Smithey *et al.*, "Measurement of the Wigner distribution and the density matrix of a light mode using optical homodyne tomography: Application to squeezed states and the vacuum," *Physical Review Letters*, vol. 70, no. 9, pp. 1244–1247, Mar. 1993. [Online]. Available: https://link.aps.org/doi/10.1103/PhysRevLett.70.1244

[161] T. Wasak *et al.*, "Cauchy-schwarz inequality and particle entanglement," *Physical Review A*, vol. 90, no. 3, p. 033616, 2014.

[162] S. Ryl *et al.*, "Unified nonclassicality criteria," *Physical Review A*, vol. 92, no. 1, p. 011801, 2015.

[163] M. Bohmann, E. Agudelo, and J. Sperling, "Probing nonclassicality with matrices of phase-space distributions," *Quantum*, vol. 4, p. 343, 2020.

[164] H. P. Yuen and J. H. Shapiro, "Quantum statistics of homodyne and heterodyne detection," in *Coherence and Quantum Optics IV: Proceedings of the Fourth Rochester Conference on Coherence and Quantum Optics held at the University of Rochester, June 8–10, 1977*. Springer, 1978, pp. 719–727.

[165] Z. Y. Ou, "Fundamental quantum limit in precision phase measurement," *Phys. Rev. A*, vol. 55, no. 4, pp. 2598–2609, Apr. 1997, publisher: American Physical Society. [Online]. Available: https://link.aps.org/doi/10.1103/PhysRevA.55.2598

[166] B. Yurke, S. L. McCall, and J. R. Klauder, "SU(2) and SU(1,1) interferometers," *Phys. Rev. A*, vol. 33, no. 6, pp. 4033–4054, Jun. 1986, publisher: American Physical Society. [Online]. Available: https://link.aps.org/doi/10.1103/PhysRevA.33.4033

[167] Z. Hradil, "Phase measurement in quantum optics," *Quantum Opt.*, vol. 4, no. 2, pp. 93–108, Apr. 1992. [Online]. Available: https://iopscience.iop.org/article/10.1088/0954-8998/4/2/004

[168] J. J. . Bollinger *et al.*, "Optimal frequency measurements with maximally correlated states," *Phys. Rev. A*, vol. 54, no. 6, pp. R4649–R4652, Dec. 1996, publisher: American Physical Society. [Online]. Available: https://link.aps.org/doi/10.1103/PhysRevA.54.R4649

[169] R. Lynch, "The quantum phase problem: a critical review," *Physics Reports*, vol. 256, no. 6, pp. 367–436, May 1995. [Online]. Available: https://www.sciencedirect.com/science/article/pii/037015739400095K

[170] G. Gour, "The quantum phase problem: steps toward a resolution," *Foundations of Physics*, vol. 32, pp. 907–926, 2002, publisher: Springer.

[171] S. M. Barnett and J. A. Vaccaro, *The Quantum Phase Operator: A Review.* Taylor & Francis, Apr. 2007, google-Books-ID: f2BiAgAAQBAJ.

[172] P. CARRUTHERS and M. M. NIETO, "Phase and Angle Variables in Quantum Mechanics," *Rev. Mod. Phys.*, vol. 40, no. 2, pp. 411–440, Apr. 1968, publisher: American Physical Society. [Online]. Available: https://link.aps.org/doi/10.1103/RevModPhys.40.411

[173] T. Linowski, K. Schlichtholz, and L. Rudnicki, "Formal relation between Pegg-Barnett and Paul quantum phase frameworks," *Phys. Rev. A*, vol. 107, no. 3, p. 033707, Mar. 2023, publisher: American Physical Society. [Online]. Available: https://link.aps.org/doi/10.1103/PhysRevA.107.033707

[174] W. Schleich, A. Bandilla, and H. Paul, "Phase from q function via linear amplification," *Physical Review A*, vol. 45, no. 9, p. 6652, 1992.

[175] M. Freyberger, K. Vogel, and W. P. Schleich, "From photon counts to quantum phase," *Physics Letters A*, vol. 176, no. 1-2, pp. 41–46, 1993.

[176] N. Quesada and J. Sipe, "The effects of self-and cross-phase modulation in the generation of bright twin beams using spdc," in *2017 Conference on Lasers and Electro-Optics (CLEO)*. IEEE, 2017, pp. 1–2.

[177] M. Riabinin, P. R. Sharapova, and T. Meier, "Bright correlated twin-beam generation and radiation shaping in high-gain parametric down-conversion with anisotropy," *Opt. Express*, vol. 29, no. 14, p. 21876, Jul. 2021. [Online]. Available: https://opg.optica.org/abstract.cfm?URI=oe-29-14-21876

[178] M. B. Nasr *et al.*, "Generation of high-flux ultra-broadband light by bandwidth amplification in spontaneous parametric down conversion," *Optics Communications*, vol. 246, no. 4-6, pp. 521–528, Feb. 2005. [Online]. Available: https://linkinghub.elsevier.com/retrieve/pii/S0030401804011162

[179] K. A. O'Donnell and A. B. U'Ren, "Observation of ultrabroadband, beamlike parametric downconversion," *Optics Letters*, vol. 32, no. 7, p. 817, Apr. 2007. [Online]. Available: https://www.osapublishing.org/abstract.cfm?URI=ol-32-7-817

[180] S. Lemieux *et al.*, "Engineering the Frequency Spectrum of Bright Squeezed Vacuum via Group Velocity Dispersion in an SU(1,1) Interferometer," *Phys. Rev. Lett.*, vol. 117, no. 18, p. 183601, Oct. 2016, publisher: American Physical Society. [Online]. Available: https://link.aps.org/doi/10.1103/PhysRevLett.117.183601

[181] A. Dubietis *et al.*, "Ultrafast Supercontinuum Generation in Bulk Condensed Media," *Lith. J. Phys.*, vol. 57, no. 3, pp. 113–157, 2017, num Pages: 45 Place: Vilnius Publisher: Lithuanian Physical Soc Web of Science ID: WOS:000416465800001.

[182] A. Couairon *et al.*, "Practitioner's guide to laser pulse propagation models and simulation," *Eur. Phys. J. Spec. Top.*, vol. 199, no. 1, pp. 5–76, Nov. 2011. [Online]. Available: https://doi.org/10.1140/epjst/e2011-01503-3

[183] G. Kulkarni *et al.*, "Classical model of spontaneous parametric down-conversion," *Phys. Rev. Res.*, vol. 4, no. 3, p. 033098, Aug. 2022, publisher: American Physical Society. [Online]. Available: https://link.aps.org/doi/10.1103/PhysRevResearch.4.033098

[184] F. DeMartini *et al.*, "Self-steepening of light pulses," *Physical Review*, vol. 164, no. 2, p. 312, 1967.

[185] R. Cheng *et al.*, "A 100-pixel photon-number-resolving detector unveiling photon statistics," *Nature Photonics*, vol. 17, no. 1, pp. 112–119, 2023.

[186] "Boxcar Averagers | Zurich Instruments," Jul. 2021. [Online]. Available: https://www.zhinst.com/en/boxcar-averagers

[187] C. R. Rao, *Linear Statistical Inference and its Applications*. John Wiley & Sons, Sep. 2009.

[188] H. Kv, "Notes on the use of propagation of error formulas," *Journal of Research of the National Bureau of Standards: Engineering and instrumentation. Section C.*, vol. 70, no. 4, p. 263, 1966.

[189] "PHAROS Femtosecond Lasers." [Online]. Available: https://lightcon.com/products/pharos-femtosecond-lasers/

[190] M. Jankowski *et al.*, "Efficient Octave-Spanning Parametric Down-Conversion at the Picojoule Level," *arXiv:2104.07928 [physics]*, Apr. 2021. [Online]. Available: http://arxiv.org/abs/2104.07928

[191] O. Jedrkiewicz *et al.*, "High visibility pump reconstruction via ultra broadband sum frequency mixing of intense phase-conjugated twin beams," *Opt. Express*, vol. 19, no. 14, p. 12903, Jul. 2011. [Online]. Available: https://opg.optica.org/oe/abstract.cfm?uri=oe-19-14-12903

[192] A. Allevi, G. Chesi, and M. Bondani, "Generation of quasi-single-mode twin-beam states in the high-intensity domain," *International Journal of Quantum Information*, vol. 15, no. 08, p. 1740021, Dec. 2017. [Online]. Available: https://www.worldscientific.com/doi/abs/10.1142/S0219749917400214

[193] R. DeSalvo *et al.*, "Infrared to ultraviolet measurements of two-photon absorption and n/sub 2/ in wide bandgap solids," *IEEE J. Quantum Electron.*, vol. 32, no. 8, pp. 1324–1333, Aug. 1996. [Online]. Available: http://ieeexplore.ieee.org/document/511545/

[194] X. Li *et al.*, "Multiple-harmonic generation in rare gases at high laser intensity," *Physical Review A*, vol. 39, no. 11, p. 5751, 1989.

[195] S. Ghimire *et al.*, "Observation of high-order harmonic generation in a bulk crystal," *Nature physics*, vol. 7, no. 2, pp. 138–141, 2011.

[196] P. R. Sharapova *et al.*, "Properties of bright squeezed vacuum at increasing brightness," *Physical Review Research*, vol. 2, no. 1, p. 013371, Mar. 2020. [Online]. Available: https://link.aps.org/doi/10.1103/PhysRevResearch.2.013371

[197] G. Cerullo and S. De Silvestri, "Ultrafast optical parametric amplifiers," *Review of Scientific Instruments*, vol. 74, no. 1, pp. 1–18, Jan. 2003. [Online]. Available: http://aip.scitation.org/doi/10.1063/1.1523642

[198] C. Manzoni and G. Cerullo, "Design criteria for ultrafast optical parametric amplifiers," *Journal of Optics*, vol. 18, no. 10, p. 103501, Oct. 2016. [Online]. Available: https://iopscience.iop.org/article/10.1088/2040-8978/18/10/103501

[199] "ORPHEUS-F Broad-Bandwidth Hybrid OPA." [Online]. Available: https://lightcon.com/products/orpheus-f-hybrid-opa/

[200] "BBO Crystals for Second Harmonic Generation." [Online]. Available: https://www.thorlabs.com/bbo-crystals-for-second-harmonic-generation?tabName=Damage%20Thresholds

[201] K. Goda and B. Jalali, "Dispersive Fourier transformation for fast continuous single-shot measurements," *Nature Photonics*, vol. 7, no. 2, pp. 102–112, Feb. 2013. [Online]. Available: http://www.nature.com/articles/nphoton.2012.359

[202] A. Mahjoubfar *et al.*, "Time stretch and its applications," *Nature Photon*, vol. 11, no. 6, pp. 341–351, Jun. 2017. [Online]. Available: https://www.nature.com/articles/nphoton.2017.76

[203] A. Eckstein, B. Brecht, and C. Silberhorn, "A quantum pulse gate based on spectrally engineered sum frequency generation," *Opt. Express, OE*, vol. 19, no. 15, pp. 13 770–13 778, Jul. 2011, publisher: Optica Publishing Group. [Online]. Available: https://opg.optica.org/oe/abstract.cfm?uri=oe-19-15-13770

[204] Y. Kurochkin, A. S. Prasad, and A. I. Lvovsky, "Distillation of The Two-Mode Squeezed State," *Physical Review Letters*, vol. 112, no. 7, p. 070402, Feb. 2014. [Online]. Available: https://link.aps.org/doi/10.1103/PhysRevLett.112.070402

[205] S. Virally, S. Lacroix, and N. Godbout, "Limits of heralded single-photon sources based on parametric photon-pair generation," *Physical Review A*, vol. 81, no. 1, p. 013808, Jan. 2010. [Online]. Available: https://link.aps.org/doi/10.1103/PhysRevA.81.013808

[206] S. M. Barnett and D. T. Pegg, "Quantum theory of optical phase correlations," *Phys. Rev. A*, vol. 42, no. 11, pp. 6713–6720, Dec. 1990. [Online]. Available: https://link.aps.org/doi/10.1103/PhysRevA.42.6713

[207] R. Tanaś, A. Miranowicz, and T. Gantsog, "Vi quantum phase properties of nonlinear optical phenomena," in *Progress in Optics*. Elsevier, 1996, vol. 35, pp. 355–446.

[208] M. Selvadoray and M. S. Kumar, "Phase properties of correlated two-mode squeezed coherent states," *Optics communications*, vol. 136, no. 1-2, pp. 125–134, 1997.

[209] A. Fougères, C. Monken, and L. Mandel, "Measurements of the probability distribution of the phase difference between two quantum fields," *Optics letters*, vol. 19, no. 21, pp. 1771–1773, 1994.

[210] M. Vollmer, K.-P. Möllmann, and J. A. Shaw, "The optics and physics of near infrared imaging," in *SPIE Proceedings*, vol. 9793. Bordeaux, France: SPIE, Oct. 2015, p. 97930Z, iSSN: 0277-786X. [Online]. Available: http://proceedings.spiedigitallibrary.org/proceeding.aspx?doi=10.1117/12.2223094

[211] "Extended InGaAs Image Sensors Questions & Answers | Hamamatsu Photonics." [Online]. Available: https://hub.hamamatsu.com/us/en/ask-an-engineer/imaging/extended-ingaas-image-sensors-questions-and-answers.html

[212] "ZephIR 2.5, SWIR, 850-2500 nm, infrared camera." [Online]. Available: https://www.photonetc.com/products/zephir-2-5

[213] "Thorlabs - PDA10CS2 InGaAs Switchable Gain Amplified Detector, 900 - 1700 nm, 13 MHz BW, 0.8 mm^2, Universal 8-32 / M4 Mounting Holes." [Online]. Available: https://www.thorlabs.com

[214] "Response-Flattening Filters for Silicon Photodiodes." [Online]. Available: https://www.thorlabs.com

[215] "Long Wave Pass Filter 102102." [Online]. Available: https://www.layertec.de/en/shop/datasheet-102102/

[216] "FEMTO® - HLVA-100 logarithmic voltage amplifier." [Online]. Available: https://www.femto.de/en/voltage-amplification/dc-up-to-100-mhz-logarithmic-voltage-amplifier-hlva-100-2/

[217] J. Hartmann, *Objektivuntersuchungen*. Springer, 1904.

[218] R. V. Shack, "Production and use of a lenticular hartmann screen," in *Spring Meeting of Optical Society of America, 1971*, vol. 656, 1971.

[219] D. Adamou *et al.*, "Quantum-enhanced time-domain spectroscopy," *Science Advances*, vol. 11, no. 4, p. eadt2187, 2025.

[220] J. O. Tollerud *et al.*, "Femtosecond covariance spectroscopy," *Proceedings of the National Academy of Sciences*, vol. 116, no. 12, pp. 5383–5386, Mar. 2019. [Online]. Available: http://www.pnas.org/lookup/doi/10.1073/pnas.1821048116

[221] G. Demontigny *et al.*, "Electron tunneling driven by bright two-mode squeezed quantum pulses," in *Ultrafast Phenomena and Nanophotonics XXIX*, vol. 13364. SPIE, 2025, pp. 16–19.

[222] G. Thekkadath *et al.*, "Gain-Induced Group Delay in Spontaneous Parametric Down-Conversion," *Phys. Rev. Lett.*, vol. 133, no. 20, p. 203601, Nov. 2024, publisher: American Physical Society. [Online]. Available: https://link.aps.org/doi/10.1103/PhysRevLett.133.203601

APPENDIX A PHOTON STATISTICS FOR MAXIMAL EFFICIENCY OF MULTIPHOTON PROCESSES

We consider a light source with a discrete photon number probability distribution

$$P(n) = p_n \tag{A.1}$$

where p_n is the probability to detect exactly n photons over a given time window Δt such that the average photon flux $\langle n_t \rangle = \langle n \rangle / \Delta t$. We assume that the time window Δt is much smaller that the coherence time of the field such that its inherent statistics are properly resolved and not averaged out over in integration. We here search optimal values q_n^2 for the p_n coefficients such that the efficiency of a m-photons perturbative nonlinear process

$$\eta_m \propto \langle n_t \rangle^{m-1} g^{(m)} = \frac{\left\langle \Pi_{i=0}^{m-1}(n-i) \right\rangle}{\langle n \rangle \, \Delta t^{m-1}} \tag{A.2}$$

is maximized. Squared coefficients q_n^2 are used to impose non-negative probabilities. η_m reaches an extremum when its gradient with respect to all coefficients q_n is 0:

$$\frac{\partial \eta_m}{\partial q_j} = 0 \qquad \forall j \in \mathbb{Z} + \ . \tag{A.3}$$

Any physical and non-trivial solution to this set of equation should also satisfy two constraints : 1) all probabilities must sum to 1

$$\sum_n q_n^2 = 1 \ , \tag{A.4}$$

and 2) the source should emit a finite average photon flux

$$\sum_n n q_n^2 = \langle n \rangle \ . \tag{A.5}$$

Those two constraints are added to equation (A.3) using the method of Lagrange multipliers. Under the constraint of finite photon flux (i.e. $\langle n \rangle$ is a fixed constant), maximizing η_m is identical to maximizing its numerator $\left\langle \Pi_{i=0}^{m-1}(n-i) \right\rangle$, simplifying the problem. The new set of equations to solve is therefore

$$\frac{\partial}{\partial q_j}\left\langle \Pi_{i=0}^{m-1}(n-i)\right\rangle - \lambda_0 \frac{\partial}{\partial q_j}\left(\sum_n q_n^2 - 1\right) - \lambda_1 \frac{\partial}{\partial q_j}\left(\sum_n n q_n^2 - \langle n\rangle\right) = 0 \qquad \forall j \in \mathbb{Z}+ \quad \text{(A.6)}$$

$$2\sum_n \Pi_{i=0}^{m-1}(j-i)q_j - \lambda_0 2q_j - \lambda_1 2jq_j = 0 \qquad \forall j \in \mathbb{Z}+ \quad \text{(A.7)}$$

$$q_j\left(\Pi_{i=0}^{m-1}(j-i) - \lambda_0 - \lambda_1 j\right) = 0 \qquad \forall j \in \mathbb{Z}+ \ . \quad \text{(A.8)}$$

We first consider the 0-th equation. While q_0 can be arbitrarily small, it cannot be null for a finite photon flux since $q_0 = 0$ would imply that any arbitrarily small time window Δt would always be guarantied to contain at least one photon. We can therefore solve for the first Lagrange multiplier λ_0

$$\lambda_0 = 0 \ . \quad \text{(A.9)}$$

Then, we consider the N-th equation, where is N is defined such that $N/\Delta t$ is the highest possible photon flux, i.e. $q_M^2 > 0$ and $q_n^2 = 0 \ \forall n > N$. N is finite, but can be arbitrarily large, so there is no loss of generality for a finite photon flux. With this, we find the second Lagrange multiplier λ_1

$$\Pi_{i=0}^{m-1}(N-i) - \lambda_1 N = 0 \quad \text{(A.10)}$$

$$\lambda_1 = \frac{\Pi_{i=0}^{m-1}(N-i)}{N} = \Pi_{i=1}^{m-1}(N-i) \ . \quad \text{(A.11)}$$

The set of equations (A.8) becomes

$$q_j j\left(\Pi_{i=1}^{m-1}(j-i) - \Pi_{i=1}^{m-1}(N-i)\right) = 0 \qquad \forall j \in [0, N] \ . \quad \text{(A.12)}$$

Equation (A.12) is verified if and only if $q_j = 0$, $j = 0$, $j = N$ or $m > N$. The last inequality describe a trivial case where the source always emits less than m photons at a time, which yields $\eta_m = 0$. Therefore, for all other cases we must conclude that $q_j = 0 \ \forall \ j \neq \{0, N\}$, i.e. the source always emits either 0 or N photons. With this, we can find expressions for the probabilities $p_0 = q_0^2$ and $p_N = q_N^2$ using the two constraints

$$\sum_n np_n = \langle n \rangle \tag{A.13}$$

$$Np_N = \langle n \rangle \tag{A.14}$$

$$p_N = \langle n \rangle / N \tag{A.15}$$

$$\sum_n p_n = 1 \tag{A.16}$$

$$p_0 + p_N = 1 \tag{A.17}$$

$$p_0 = 1 - p_N = 1 - \langle n \rangle / N \tag{A.18}$$

and we find that η_m takes a very simple form:

$$\eta_m \propto \frac{\left\langle \Pi_{i=0}^{m-1} n - i \right\rangle}{\langle n \rangle \, \Delta t^{m-1}} \tag{A.19}$$

$$\eta_m \propto \frac{\sum_n \Pi_{i=0}^{m-1} (n-i) p_n}{\langle n \rangle \, \Delta t^{m-1}} \tag{A.20}$$

$$\eta_m \propto \frac{\Pi_{i=1}^{m-1} (N-i)}{\Delta t^{m-1}} \ . \tag{A.21}$$

Up to process-dependent constants and in the perturbative regime, equation (A.21) gives the highest efficiency η_m achievable for a m-photons process with a light source having an average and maximal photon flux $\langle n \rangle / \Delta t$ and $N/\Delta t$ respectively.

The corresponding optimal photon probability distribution describes a source which emits no light for long periods of time of average duration $N\Delta t / \langle n \rangle$, and then emits a burst of N photons contained in a small time window Δt. Those conditions are reproduced experimentally to a very good approximation by an ultrafast pulsed laser with an effective pulse duration $\tau = \Delta t$, repetition rate $f_{\mathrm{rr}} = \langle n \rangle / N \Delta t$ and average photon content per pulse $\langle n_p \rangle = N$. When considering high-power laser systems with $\langle n_p \rangle \gg m$, we find that

$$\eta_m \propto \frac{\Pi_{i=1}^{m-1} (\langle n_p \rangle - i)}{\tau} \approx \left(\frac{\langle n_p \rangle}{\tau} \right)^{(m-1)} \tag{A.22}$$

and recover the classical result relating η_m to the peak pulse power.

APPENDIX B EXPONENTIAL ERROR PROPAGATION FOR NUMERICAL PREDICTION OF $\langle n \rangle$

In the single-mode, undepleted regime, the number of photons per beam in a BTBs source is

$$\langle n \rangle = \sinh^2(G) \approx \frac{e^{2G}}{4} \tag{B.1}$$

where $G \propto \sqrt{I_\mathrm{p}}$ is the parametric gain for a pump with intensity I_p, and where the last approximation holds for $G \gg 1$. If the pump intensity increases by a quantity ΔI_p, the gain increases by

$$\Delta G = G \left(\sqrt{1 + \frac{\Delta I_\mathrm{p}}{I_\mathrm{p}}} - 1 \right) \tag{B.2}$$

and in turn the average number of photons increases by

$$\Delta \langle n \rangle \approx \langle n \rangle \left(e^{2\Delta G} - 1 \right) \approx \langle n \rangle \left((4 \langle n \rangle)^{\left(\sqrt{1+\frac{\Delta I_\mathrm{p}}{I_\mathrm{p}}} - 1 \right)} - 1 \right) \tag{B.3}$$

which shows how uncertainty on the pump intensity is exponentially amplified when trying to predict $\langle n \rangle$. For instance, a relative uncertainty on the pump intensity $\Delta I_\mathrm{p}/I_\mathrm{p} = 1\,\%$ yields an error $\Delta \langle n \rangle / \langle n \rangle = 9\,\%$, while $\Delta I_\mathrm{p}/I_\mathrm{p} = 5\,\%$ yields an error $\Delta \langle n \rangle / \langle n \rangle = 50\,\%$. To reproduce an overestimation $\Delta \langle n \rangle / \langle n \rangle \approx 100$ as observed in the simulations, the error on the pump intensity would need to be $\Delta I_\mathrm{p}/I_\mathrm{p} = 64\,\%$.

To first order, equation (B.3) also describes how technical power fluctuations of the pump get transmitted to the photons statistics of the BTBs/BSV, and might lead to an experimental overestimation of $g^{(2)}$.

APPENDIX C LIST OF CONTRIBUTIONS

Papers

1. S. Liu, S. Virally, G. Demontigny, **P. Cusson**, and D. Seletskiy, "Engineering spectro-temporal light states with physics-embedded deep learning," Ultrafast Science, 2025.
2. J.-B. Billeau, **P. Cusson**, D. V. Seletskiy, and S. Reuter, "Optical inline interferometer for enhanced low-field detection via electric-field induced second harmonic generation," Plasma Sources Science and Technology, vol. 34, no. 1, p. 01LT03, 2025.
3. J.-B. Billeau, **P. Cusson**, A. Dogariu, A. Morozov, D. V. Seletskiy, and S. Reuter, "Coherent homodyne detection for amplified cross-beam electric-field induced second harmonic," Applied Optics, vol. 63, no. 19, pp. 5203–5207, 2024.
4. J. Hogue, **P. Cusson**, M. Meunier, D. V. Seletskiy, and S. Reuter, "Sensitive detection of electric field-induced second harmonic signals," Optics Letters, vol. 48, no. 17, pp. 4601–4604, 2023.
5. S. Virally, **P. Cusson**, and D. V. Seletskiy, "Enhanced electro-optic sampling with quantum probes," Physical Review Letters, vol. 127, no. 27, p. 270504, 2021.

Talks (presenter)

1. **P. Cusson**, S. Virally, and D. V. Seletskiy, "Carrier-Envelope Phase Correlations in Few-Cycle Bright Twin Beams," in International Conference on Ultrafast Phenomena. Optica Publishing Group, 2024, proceedings to be published.
2. **P. Cusson**, A. Rasputnyi, F. Tani, D. Seletskiy, and M. Chekhova, "Ultrafast bright squeezed vacuum in nearly single spatio-temporal mode," in CLEO : Fundamental Science. Optica Publishing Group, 2024, pp. FTh1M–5.
3. **P. Cusson**, S. Virally, and D. Seletskiy, "Twin beams probe pulses for subcycle sampling of THz-MIR fields," in 2023 48th International Conference on Infrared, Millimeter, and Terahertz Waves (IRMMW-THz). IEEE, 2023, pp. 1–2.
4. **P. Cusson**, S. Virally, and D. Seletskiy, "Generation of single-mode few-cycle twin beams for time-domain quantum optics," in 2023 Photonics North (PN). IEEE, 2023, pp. 1–2.

5. **P. Cusson**, S. Virally, and D. V. Seletskiy, "Génération d'impulsions lumineuses intriquées de quelques cycles optiques," in 89e Congrès de l'Acfas, 2022.

6. **P. Cusson**, S. Virally, and D. V. Seletskiy, "Subcycle sampling of quantum fields with nonclassical temporal gates," in CLEO : Science and Innovations. Optica Publishing Group, 2021, pp. SW4F–1.

7. **P. Cusson**, S. Virally, and D. V. Seletskiy, "Quantum-enhanced electro-optic sampling," in 2021 Photonics North (PN). IEEE, 2021, pp. 1–1.

8. **P. Cusson**, S. Virally, and D. V. Seletskiy, "Entangled probes for subcycle sampling of quantum fields, in RQMP Grand Conference, 2020.

Posters (presenter)

1. **P. Cusson**, S. Virally, and D. V. Seletskiy, "Single Spatio-Temporal Mode Bright Twin Beams Driven by Sub-10-fs Pump Pulses," in International Conference on Ultrafast Phenomena. Optica Publishing Group, 2024, proceedings to be published.

2. S. Virally, **P. Cusson**, and D. V. Seletskiy, "A time-domain perspective of quantum electro-optic sampling," in International Conference on Ultrafast Phenomena. Optica Publishing Group, 2022, pp. W4A–13.

3. **P. Cusson**, S. Virally, and D. V. Seletskiy, "Nonclassical probes for enhanced electro-optic sampling of quantum fields," in Quantum days, 2022.

4. **P. Cusson**, S. Virally, and D. V. Seletskiy, "Conditioned thermal states as nonclassical gates in subcycle sampling of quantum fields," in International Conference on Ultrafast Phenomena. Optica Publishing Group, 2020, pp. Tu4A–10.

Talks and posters (co-author)

1. G. Demontigny, **P. Cusson**, L. Rivard, G. Beaudin, P. Charette, M. Hofheinz, and D. V. Seletskiy, "Electron tunneling driven by bright two-mode squeezed quantum pulses," in Ultrafast Phenomena and Nanophotonics XXIX, vol. 13364. SPIE, 2025, pp. 16–19.

2. D. Seletskiy, **P. Cusson**, A. Rasputnyi, S. Virally, F. Tani, and M. Chekhova, "Bright few-cycle quantum light," in Ultrafast Phenomena and Nanophotonics XXIX. SPIE, 2025, p. PC133640O.

3. J.-B. Billeau, **P. Cusson**, D. Seletskiy, and S. Reuter, "Enhancing sensitivity of electric-field detection," in APS Annual Gaseous Electronics Meeting Abstracts, 2024, pp. IR1–003.

4. J.-B. Billeau, J. Hogue, **P. Cusson**, M. Meunier, A. Dogariu, D. Seletskiy, and S. Reuter, "Micro electric fields detection improvements : Steps toward tailoring cold atmospheric pressure plasma," in APS Annual Gaseous Electronics Meeting Abstracts, 2023, pp. IW5–016.